

Development of a Large-Scale Vision-Based Tactile Sensing System for Robotic Links

Duong Van Lac

Japan Advanced Institute of Science and Technology

Doctoral Dissertation

Development of a Large-Scale Vision-Based Tactile Sensing System for Robotic Links

Duong Van Lac

Supervisor: **Associate Prof. Ho Anh Van**

Graduate School of Advanced Science and Technology
Japan Advanced Institute of Science and Technology
Materials Science

September, 2021

Abstract

The sense of touch allows individuals to physically perceive and interact with their environment. Touch is even crucial for robots, as robots equipped with tactile sensation can more safely interact with the surroundings. Although in recent decades, tactile sensing technology has shown great advances in design, the main challenges relate to mimicking the inherent complexity of natural skin structure that has a particularly high density of receptors, e.g. mechanoreceptors (pressure and vibration sensing), thermoreceptors (temperature sensing), and nociceptors (pain and damage sensing). The conventional approaches focused mostly on developing a skin-like structure with a small matrix of sensing elements without considering system-level design, such as the bulk of wires and electronic components, the complication of data processing and transmitting, and risk of damage.

The research describes the development of a vision-based artificial sensory system for robotic links, called TacLINK, which can be assembled to form a whole-body tactile sensing robot arm. The developed system is an elongated structure consisting of a skeletal transparent tube covered by a continuous artificial skin, which is soft, very safe and comfortable to touch and interact. When contacting with the surrounding environment (real-world objects and humans), TacLINK perceives tactile information through the three-dimensional (3-D) deformation of the skin that results from the tracking of an array of marker points sitting on its inner wall by two cameras installed at both sides of the transparent tube.

Remarkably, a finite element model with shell structure for the skin body was successfully established to describe the relationship between applied forces and the displacements of these markers, allowing computation of tactile force. Thus, TacLINK provides simultaneous contact geometry and distribution of contacted force throughout the skin surface, regardless of the number of contact points and contact area with humans and various real-world objects. Besides, artificial skin of TacLINK not only provides tactile force feedback but can change its form and nominal stiffness by providing air to inflate at low pressure (0–2.5 kPa).

The scientific and technical contributions of the research are:

1) A novel design of a large-scale tactile sensing system at low-cost for robot links: The research proposes an accomplished tactile sensing system for robot links with a large sensing area $\sim 500 \text{ cm}^2$ at low cost (about 150\$US). The developed system is high performance in sensing both contact geometry and contact force upon interactions between the robot and surroundings.

2) An efficient vision-based tactile sensing system: The proposed vision system comprising two facing cameras with proposed algorithms (i.e., stereo registration, 3-D reconstruction, self-calibration technique) reconstructs efficiently displacements of all the markers locating on the inner wall of the elongated skin surface. This vision-based sensing shows the advantages for developing large-scale tactile sensing systems, such as minimizing the challenges in wiring, and the bulk of electronics. This vision system could be utilized widely for other similar systems, such as prosthetic arms, legs.

3) The finite element method (FEM) for tactile force sensing: Previous research on vision-based force-sensing faced difficulty in the derivation of force in relationship with displacement/deformation. This research utilized the FEM to derive the structural stiffness of the skin with shell structures that is a key to calculate the contact force. Besides, based on FEM, we could also characterize the skin to evaluate the design and choose the suitable materials for the specified application.

4) A highly scalable structure and generalized sensing principle for the development of the vision-based tactile sensing devices: The proposed artificial skin with markers is very simple and easily fabricated by the casting method. The shape and size are customizable for the specified applications. The FEM is generalized that the structural stiffness of the skin could be derived by using the analytical FEM. Vision technology now is powerful and small in size, thus a set of cameras can be set to track the displacements of the skin. Thus, the research expects to contribute significantly to the field of tactile sensing with a generalized technique for designing vision-based tactile force sensing devices.

To sum up, TacLINK is compact in design, scalable in size, durable in operation, but low in cost, as well as being a high-performance tactile sensing system. The proposed system can be widely exploited in the design of robotic arms, prosthetic arms, and humanoid robots, etc.

This thesis introduces the entire development process of TacLINK, from design, modeling, calibration, implementation of algorithms, as well as experiments for evaluation of the system.

Keywords: Tactile sensing skin, vision-based force sensing, non-rigid registration, finite element method (FEM), soft robotics.

Acknowledgements

I would like to deeply thank my supervisor, Assoc. Professor Van Anh Ho for his support and giving me an opportunity to research in his laboratory at Japan Advanced Institute of Science and Technology (JAIST). Thanks to, Student Affairs Department, Educational Affairs Department, and all faculty members of JAIST for their kind help to my work.

I would like to sincerely thank Dr. Nguyen Trong Doanh, Dr. Mac Thi Thoa, and all my colleagues at the Hanoi University of Science and Technology (HUST), Department of Mechatronics, for their help and support.

I gratefully acknowledge the financial supports from Honda Foundation for ten weeks internship at JAIST from October 29, 2017, to January 07, 2018, and the Japanese Government Scholarship (Monbukagakusho: MEXT) for my Ph.D. course at JAIST from October 01, 2018 to September 30, 2021.

Finally, I express my deepest gratitude to my parents for their endless loving for me.

Japan, September 2021

Duong Van Lac

HO Laboratory

School of Materials Science

Japan Advanced Institute of Science and Technology

To my mother and father

Contents

Abstract	i
Acknowledgements	iv
List of Figures	xiv
List of Tables	xv
1 Introduction	1
1.1 Human Tactile Sensing	1
1.2 Tactile Sensing Technology	2
1.2.1 Tactile Sensing Principles	3
1.2.2 Potential Applications	6
1.2.3 Challenges	8
1.3 Research Purpose	9
1.4 Thesis Outline	10
2 Related Work	12
2.1 Large-Scale Robotic Tactile Skin	12
2.2 Vision-based Tactile Sensor	14
2.3 Vision-based Force Sensing	16
2.4 Summary	17

3 TacLINK	19
3.1 Approach	19
3.2 System Requirement and Design	20
3.2.1 Mechanical Design	20
3.2.2 Vision System Design	23
3.3 Sensing Principle	26
3.4 Artificial Skin Fabrication	27
3.5 Summary	31
4 Vision-Based Modeling	32
4.1 Stereo Camera Model	32
4.2 Uncertainty Analysis	36
4.3 Image Processing	39
4.4 Notations and Marker Numbering	41
4.5 Non-rigid Stereo Registration	42
4.6 3-D Reconstruction	48
4.7 Camera Calibration	51
4.8 Experimental Accuracy	57
4.8.1 Setup	57
4.8.2 Experimental Result	58
4.9 Summary	59
5 Finite Element Modeling	60
5.1 Introduction	60
5.2 Fundamentals	62
5.3 FE Mesh and Element Geometry	66
5.3.1 Meshing	68
5.3.2 Element Geometry	68
5.4 Element Displacement Field	70
5.5 Element Strain Field	73
5.6 Element Equation	75

5.7	Global Finite Element Equation	77
5.8	Simulation Result	79
5.9	Young's modulus Calibration	81
5.10	Summary	85
6	Tactile Force Reconstruction	86
6.1	Tactile Force Calculation	86
6.2	Sensitivity Analysis	87
6.3	Experimental Evaluation	89
6.3.1	Experimental Setup	89
6.3.2	Single Point Contact	91
6.3.3	Multiple Large Area Contacts	99
6.4	Summary	104
7	Conclusion	105
7.1	Summary and Contribution	106
7.2	Discussion	107
7.2.1	Vision-Based Tactile Force Sensing	107
7.2.2	FE Model and Material Nonlinearity	108
7.3	Future Work and Outlook	109
List of Publications		111
Reference		111

List of Figures

1.1	Structure of sensory touch receptors in human skin, and transmission of tactile signal from fingertips to somatosensory cortex of brain [1], [2].	2
1.2	Some recent electronic skins. (a) A stretchable silicon nanoribbon skin for smart prosthetics [6]. (b) A matrix of strain sensor based on a piezopotential-gated graphene transistor [7]. (c) A stretchable circuit of dense transistors array for health monitoring and human-machine interface [8].	3
1.3	Schematic illustrations of basic transduction mechanisms for tactile sensors [9]. (a) Capacitance. (b) Piezoresistivity. (c) Piezoelectricity.	4
1.4	Potential applications of artificial tactile skin across multiple domains. (a) Intelligent robots. (b) Prosthetics (c) Medical devices.	7
1.5	Flowchart of TacLINK development.	11
2.1	Example of robot application in humans life. (a) Toshiba's humanoid robot. (b) RIBA nursing-care assistant robot. (c) PARO therapeutic robot for use in nursing homes and hospitals.	13

2.2 Examples of the nearest deployment of whole-body large-scale robotic tactile skin. (a) RI-MAN robot with flexible printed circuits (FPC) skin for human-robot interaction [36]. (b) iCub robot covered with a mesh of triangles printed circuit boards (PCB) [10]. (c) The allegro hand covered by hexagonally shaped PCB skin cells, which can sense multimodal sensing: temperatures, light touch, accelerations, and proximity [38].	14
2.3 Example designs of the vision-based tactile sensor. (a) the GelForce sensor [41]. (b) The Gesight sensor [42]. (c) The TacTip sensor [44].	15
3.1 A prototype of a robotic arm with tactile sensing links.	20
3.2 Structure of the proposed TacLINK (cross-section view).	21
3.3 The main components for building the TacLINK.	21
3.4 A tube subject to bending and torsional moments.	22
3.5 The observed size of a marker on the camera.	25
3.6 The dead zone of the camera.	26
3.7 Vision-based tactile force sensing principle of TacLINK.	27
3.8 (a) CAD design of the mold. (b) The printed parts of the mold.	28
3.9 (a) Mixing the Ecoflex 00-50 materials of part A: part B with Sile pigment (black color for the skin body and white color for markers). (b) Degassing the silicone mixture in a vacuum chamber.	29
3.10 Casting mold for skin fabrication. (a) The 3-D printable casting mold. (b) Filling female holes of the inner mold with white silicone to cast the markers array. (c) The actual soft skin body after fabrication with distributed markers. (a) Top view. (b) Inside view.	30

4.1 Configuration of the stereo vision system (stereo camera). The world coordinate system (WCS) is XYZ , whose Z -axis locates on the baseline that is the centreline of the skin. Its origin coincides with the center of the first end, and its X -axis is parallel to the X_{c_1} -axis and anti-parallel X_{c_2} -axis of the camera frames. Note that the image of camera 2 was inverted about its y_2 -axis to unify the direction of the coordinates of the two images. Thus, the image coordinates on the x_1/x_2 - and y_1/y_2 -axes are in the same directions as the X and Y -axes of WCS, respectively.	33
4.2 Stereo uncertainty evaluation results illustrating the highest variations of error in the working space. (a) Uncertainty of Z coordinate with deviations $\Delta r_1 = -1/\sqrt{2}, \Delta r_2 = 1/\sqrt{2}$. (b) Uncertainty of radial coordinate ΔR with deviations $\Delta r_1 = 1/\sqrt{2}, \Delta r_2 = 1/\sqrt{2}$	38
4.3 Image processing for marker detecting in captured images. (Left) Image processing of camera 1. (Right) Image processing of camera 2.	40
4.4 Marker numbering on the stereo images (i.e., sets I_1 and I_2).	42
4.5 The intuitive curve tracking algorithm. Using the proposed objective function with two known anchor points, ϑ_0 and ϑ_{n_2} , the tracking process can trace unknown nodes sequentially $\vartheta_1, \vartheta_2, \dots, \vartheta_{n_2-1}$	44
4.6 A scenario for illustration of the proposed stereo implementation, where the TacLINK is in contact with a long cylinder surface. (a) Stereo images with the proposed path tracking algorithm. (b) 3-D Reconstruction from stereo images of the 3-D shape of the skin.	46

4.7	Linear interpolation in a path. The coordinates of the missing node ℓ_j is linearly interpolated between the nearest two known nodes ℓ_{j-} and ℓ_{j+} on the same path ℓ	48
4.8	Illustration of the robust performance of proposed vision-based sensing for 3-D shape reconstruction of the skin surface. (a1), (b1), and (c1) The skin is subjected to multi-contact points (three points). (a2), (b2), and (c2) The skin is under pressurization of 1.5 kPa.	50
4.9	Calibration results for each iteration: RMSE of coordinates for estimating stereo parameters and lens distortion.	54
4.10	Illustration of the initial 3-D position of markers (roundly marked) using the calibrated parameters.	55
4.11	A ray of light being refracted in the transparent acrylic tube. .	57
4.12	Experiment evaluating the measurement accuracy of the vision system in the radial direction. (a) Experimental setup. (b) Measured displacements of ten nodes on a path comparing with deflections created by robot motion.	58
5.1	FE simulation for the skin using ANSYS student software. The skin is subjected to an inner pressure of 1.5 kPa.	61
5.2	Common element families [62].	62
5.3	Element categories [63].	63
5.4	Finite element discretization.	65
5.5	Discretization of solid and flat shell elements [64].	65
5.6	FEM discretization of a cylindrical skin surface in flat rectangular shell elements. (a) Finite element mesh of $N_e = 264$ elements and $N = 288$ nodes. (b) Mesh topology.	67
5.7	Element geometry and coordinate systems.	69
5.8	FE model simulation results for soft artificial skin. (a) Skin deformation by a normal force 0.2 N at node #127(7,5). (b) Response of skin to additional inner air pressure $P = 0.5$ kPa. .	80

5.9	Inflation experiment for calibrating Young's modulus of the silicone material (Ecoflex 00-50). (a) Measuring the curvature of the skin under inner air pressure. (b) Comparison of experimental data (solids) and FE model (lines) with calibrated Young's modulus E of skin curvature in response to applied inner pressures of 0.5, 1, and 1.5 kPa.	84
6.1	FE model simulation of the reaction force at node #127(7,5) for evaluating the force reconstruction error in each direction. (a) The response of the skin constrained at node #127 by Eq. (6.3). (b) Illustration of three tangential, radial, and axial components of the reaction force at node #127.	88
6.2	The experimental platform for measurement.	90
6.3	Probe forces applied yielding radial deflections ΔR at node #127 compared with the nodal tactile forces at node #127 obtained from TacLINK and simulation under different inner air pressures.	92
6.4	Contact force reconstruction of the probe applied yielding radial deflections ΔR at node #127 with inner air pressure $P = 0$ kPa.	95
6.5	Contact force reconstruction of the probe applied yielding radial deflections ΔR at node #127 with inner air pressure $P = 0.5$ kPa.	96
6.6	Contact force reconstruction of the probe applied yielding radial deflections ΔR at node #127 with inner air pressure $P = 1.0$ kPa.	97
6.7	Contact force reconstruction of the probe applied yielding radial deflections ΔR at node #127 with inner air pressures $P = 1.5$ kPa.	98
6.8	Touching TacLINK with a flat surface.	100
6.9	Touching TacLINK with a curved cylinder surface.	101

6.10 Touching TacLINK with a finger.	101
6.11 Touching TacLINK with multiple fingers.	102
6.12 Pinching TacLINK by fingers.	102
6.13 Squeezing TacLINK by fingers.	103

List of Tables

3.1	Camera specifications.	23
3.2	Material specifications (Ecoflex TM 00-50, Smooth-On Inc., USA).	27
4.1	Self-Calibration Results of Stereo Camera Parameters ($\mu \pm \sigma$)	53
5.1	Coordinates and weights for Gauss integration [66].	77

Nomenclature

The following is a list of principal symbols that will be later used within the body of the document.

FEM Finite element method

2-D Two-Dimensional

3-D Three-Dimensional

Skin Parameters

ID Inner diameter

OD Outer diameter

L Length

D_{marker} Diameter of the marker

h Vertical pitch of the marker array

γ Circular pitch of the marker array

Vision System Model

XYZ World/Global coordinate system (WCS)

r, φ	Polar coordinates
R, φ, Z	Cylindrical coordinates
$X_{c_1} Y_{c_1} Z_{c_1}, X_{c_2} Y_{c_2} Z_{c_2}$	Camera coordinate systems (CCS)
$x_1 y_1, x_2 y_2$	Image coordinate systems
$u_1 v_1, u_2 v_2$	Pixel coordinates systems
c_1, c_2	Principal points
f_1, f_2	Focal lengths
b_1, b_2	Extrinsic parameters
$k_{11}, k_{21}, k_{12}, k_{22}$	Lens distortion coefficients
$S \times S$	Cropped image area
ℓ	Path index
j	Cell index
N	Number of FE nodes
\mathcal{N}	Set of FE nodes
\mathcal{M}	Set of free nodes/markers labeled
$\mathcal{B}_1, \mathcal{B}_2$	Set of fixed nodes labeled
I_1, I_2	Unorganized sets of detected markers
Φ_1, Φ_2	Organized sets of detected markers
\mathbf{x}	3-D initial position vector of all nodes
\mathbf{X}	3-D position vector of all nodes

Finite Element Model and Tactile Force Computation

X, Y, Z	Global coordinates
\hat{x}, \hat{y}	Local coordinates
$u_{\hat{x}}, u_{\hat{y}}, u_{\hat{z}}$	Local translations about Cartesian axes
$\theta_{\hat{x}}, \theta_{\hat{y}}$	Local rotational degrees of freedom
$u_{\hat{X}}, u_{\hat{Y}}, u_{\hat{Z}}$	Global translations about Cartesian axes
$\theta_{\hat{X}}, \theta_{\hat{Y}}, \theta_{\hat{Z}}$	Global rotations about Cartesian axes
F_X, F_Y, F_Z	Global force components
M_X, M_Y, M_Z	Global moment components
$\hat{\mathbf{u}}$	Displacement field vector
P	Inner air pressure
$\hat{\mathbf{s}}$	Surface load of inner air pressure
$\hat{\boldsymbol{\epsilon}}$	Generalized strain vector
$\hat{\boldsymbol{\sigma}}$	Generalized stress vector
\mathbf{B}	Strain-displacement matrix
\mathbf{C}	Constitutive matrix of material
E	Young's Modulus
ν	Poison's ratio
$\hat{\mathbf{f}}$	Local force vector of an element
\mathbf{f}	Global force vector of an element

$\hat{\mathbf{f}}^{\text{ext}}, \mathbf{f}^{\text{ext}}$	External concentrated force vectors
$\hat{\mathbf{f}}_{\text{pressured}}, \mathbf{f}_{\text{pressured}}$	Distributed force vectors
$\hat{\mathbf{d}}$	Local displacement vector of an element
\mathbf{d}	Global displacement vector of an element
$\hat{\mathbf{k}}$	Element stiffness matrix in the local coordinates
\mathbf{k}	Element stiffness matrix in the global coordinates
\mathbf{F}	Global vector of nodal forces
\mathbf{F}^{ext}	External concentrated force vectors
$\mathbf{F}_{\text{pressured}}$	Distributed force vectors
\mathbf{D}	Global vector of nodal displacements
\mathbf{K}	Global stiffness matrix
$\mathbf{D}_{\text{measured}}$	Measured nodal displacements
\mathbf{F}^{tac}	Vector of tactile forces

Chapter 1

Introduction

1.1 Human Tactile Sensing

As humans, we rely on the five senses of sight, touch, taste, smell, and hearing as a means to perceive and interact with the surroundings. Utilizing one or a combination of these senses, humans discover, experience, and survive in environments. Touch sensations, such as pressure, vibration, temperature, pain, and humidity, are perceived through human skin which is the key and largest sensory organ protecting the inner body organs from external harm. Such touch information arises from the multiple receptors located within complex layers of the skin, such as the epidermis and dermis that are shown in Fig. 1.1. The epidermis layer is a protective surface responsible for maintaining body temperature, while the dermis layer locating under the epidermis flashes nerve signals from mechanical, thermal, chemical, and various stimuli to the central nervous system (brain). After processing the signals, the brain gives reactive behaviors in the form of physical response. Through touch sensing, especially on hands and fingers, humans can perceive contact pressure to infer object properties such as size, shape, hardness, through which humans not only interact safely with the environment but also handle skillfully with the real-world object, etc.

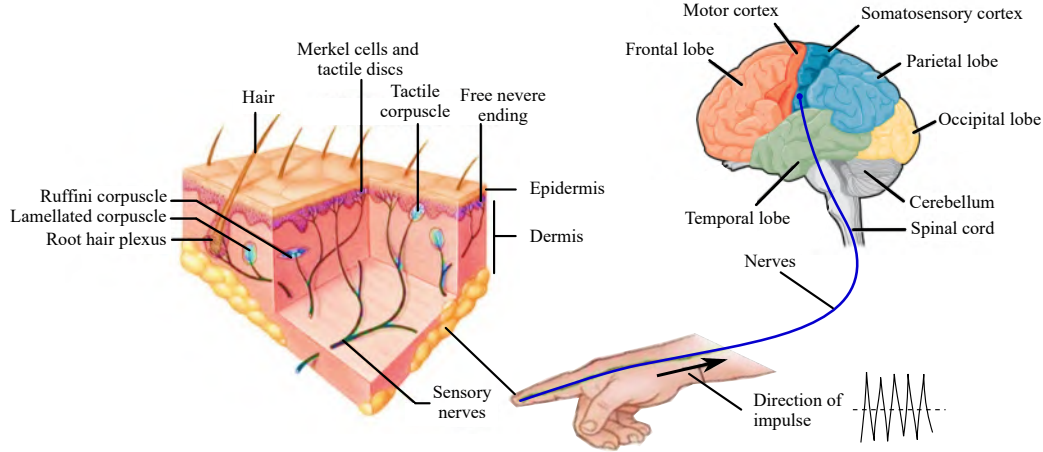


Figure 1.1: Structure of sensory touch receptors in human skin, and transmission of tactile signal from fingertips to somatosensory cortex of brain [1], [2].

1.2 Tactile Sensing Technology

The human skin has a wide range of touch receptors that perceive many forms of touch, such as mechanoreceptors for pressure and vibration sensing, thermoreceptors for temperature sensing, and nociceptors for pain and damage sensing. It is desirable to develop robotic devices with similar sensing capability, especially for applications of humanoid robotics, prosthetics. Since the early 1980s, artificial touch sensing has been fast-evolving research involving a strong interdisciplinary effort from researchers in different fields, such as physics, electronics, material sciences, and robotics, etc. The tactile sensor is normally designed as a matrix of sensing elements, for example as shown in Fig. 1.2, and a large list of relevant design specifications was introduced [1–5]. Nonetheless, these approaches focused mainly on developing a skin-like structure at a small scale with the target to detect strain, pressure, temperature, or humidity without considering system-level design and deployment issues when developing at a large scale, such as the bulk of wires and analog-to-digital converters, the effect of noise, and the risk of damage.

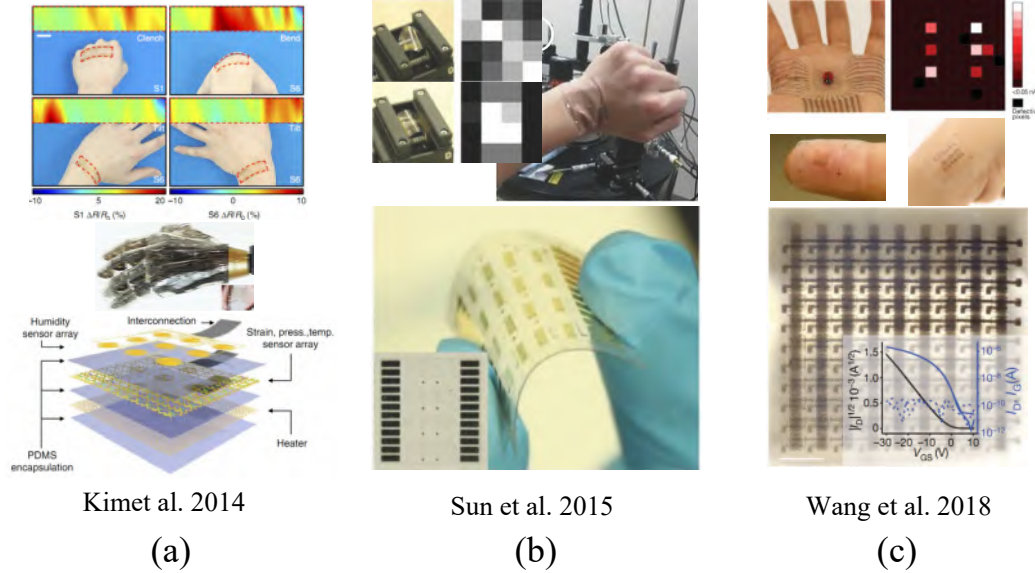


Figure 1.2: Some recent electronic skins. (a) A stretchable silicon nanoribbon skin for smart prosthetics [6]. (b) A matrix of strain sensor based on a piezopotential-gated graphene transistor [7]. (c) A stretchable circuit of dense transistors array for health monitoring and human-machine interface [8].

1.2.1 Tactile Sensing Principles

The common techniques currently being used for the tactile sensors are based on capacitive, piezoresistive, piezoelectric, magnetic, and optical transduction methods. Each of these transduction principles employed to convert physical stimuli from the environment into an electrical signal for a data acquisition system has different characteristics. Below is the brief review of basic tactile sensing methods and their advantages and disadvantages.

Capacitive Tactile Sensors

The capacitive tactile sensor is based on the change of measured capacitance from an applied force over two parallel plates capacitor, as illustrated in Fig. 1.3(a) and given in Eq. (1.1), where $\epsilon_0 = 8.854 \times 10^{-12} \text{ F} \cdot \text{m}^{-1}$ is the constant permittivity of vacuum, ϵ is the relative permittivity of the dielectric layer, A

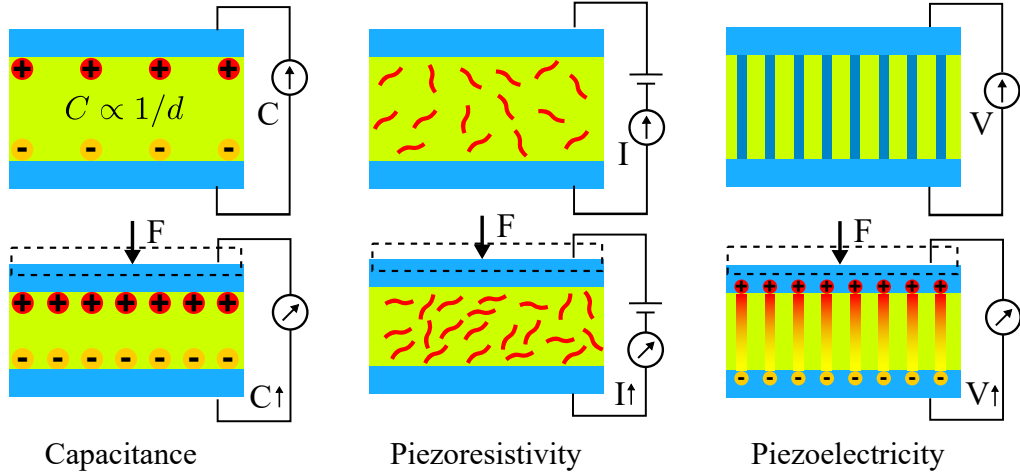


Figure 1.3: Schematic illustrations of basic transduction mechanisms for tactile sensors [9]. (a) Capacitance. (b) Piezoresistivity. (c) Piezoelectricity.

and d are the area and distance between the two parallel plates, respectively. Thus, changes in C can be utilized to measure normal strain or force.

$$C = \varepsilon_0 \varepsilon \frac{A}{d} \quad (1.1)$$

Capacitive sensors could be fabricated in a small size, enabling design and integration into dense arrays in a limited area, e.g., from the body, arms, palms, to fingertips [10]. Thus, this sensor technology has become popular in robotics for the development of sensing element “taxels” that mimic aspects of mechanoreceptors in human skin. This technology also presents various advantages in terms of high sensitivity, long-term drift stability, low power consumption [11]. Limitations include significant hysteresis, thermal drift [10], and be susceptible to external fields [12].

Piezoresistive Tactile Sensors

Piezoresistive tactile sensors measures changes in the resistance of contact materials when applying an external force. These sensors are generally fab-

ricated in conductive material, as illustrated in Fig. 1.3(b) [13, 14]. The change ΔR in the electrical resistance of piezoresistive effect can be formulated in Eq. (1.2), where R is the electrical resistance of a conductor along longitudinal direction, ν is Poisson's ratio, ε is the longitudinal strain, M_l is the longitudinal elastoresistance coefficient, ρ is the resistivity, L and A are the length and cross-sectional area of the conductor, respectively. Thus, the change in resistance can be used to infer the contact strain.

$$\frac{\Delta R}{R} = (1 + 2\nu)\varepsilon + \frac{\Delta\rho}{\rho}, \text{ with } R = \rho \frac{L}{A} \quad (1.2)$$

The benefits offered by this technology include low cost, simple data acquisition circuit, wide dynamic range, durability, and the ability for fabrication in a small size. Utilizing nanomaterials with high mechanical flexibility and chemical resistance for microstructure fabrication of sensing elements enables them to be used in wearable sensing devices, e-skin for robotics [15–17], etc. Disadvantages are susceptibility to drift and hysteresis [18, 19].

Piezoelectric Tactile Sensors

Piezoelectrical tactile sensors generate an electric charge proportional to an applied force/pressure by the piezoelectric effect [20]. The magnitude of the electrical potential of the charge density D_i ($C \cdot m^{-2}$) generated in the i -th direction is described by Eq. (1.3), where d_{ijk} ($C \cdot N^{-1}$) is the tensor of piezoresistive coefficients, X_{jk} (N/m^{-2}) is the external applied stress.

$$D_i = d_{ijk} X_{jk} \quad (1.3)$$

Piezoelectric sensors are suitable for measurement of vibrations and widely utilized in dynamic measurements owing to their sensitivity, high-frequency response, and availability in various material forms, such as plastics, ceramics, crystals, and flexible polyvinylidene fluoride (PVDF) [21]. The main drawbacks of this sensing technology is susceptibility to temperature [18].

Optical Tactile Sensors

The principle of optical tactile sensors is based on transducing physical signals, such as force, pressure, or deformation, into changes in observed light intensity, which are commonly detected by using vision sensors (e.g., CCD or CMOS camera sensors). Optical tactile sensing can be used for surface roughness sensing [22], shear and normal force [23], and force/torque sensor [24]. It can also be developed for robotic skin [25]. In general, such optical technology provides high resolution and stability, fast response, immunity to electronic noise, and can sense deformation of a surface without embedded sensors and considering the wiring problem. The main drawback of optical sensors is the required large space for light sources and distance between vision detectors and the sensing skin, thus this kind of sensor is basically thick.

1.2.2 Potential Applications

The tactile sensor provides a low-cost, highly flexible, and scalable technology for multi-modal physical contact measurements. Potential application scenarios widely range across multiple domains (see Fig. 1.4), i.e., from major robotics to health care and medical devices as below

Intelligent Robots

In comparison to vision, sensory tactile skin is not affected by occlusion and offers physical multi-modal contact sensation. The robot equipped with tactile skin could safely interact in close contact with real-world objects and humans. For instance, collaborative and humanoid robots are essential for the next generation of intelligent robots, which can be covered with large areas of tactile skin [e.g., Fig. 1.4(a)] to provide a robust sensing interface for human-robot interaction. Besides, the handheld robot teaching pendants could be replaced with a realistic touch interface. The sensitive skin can

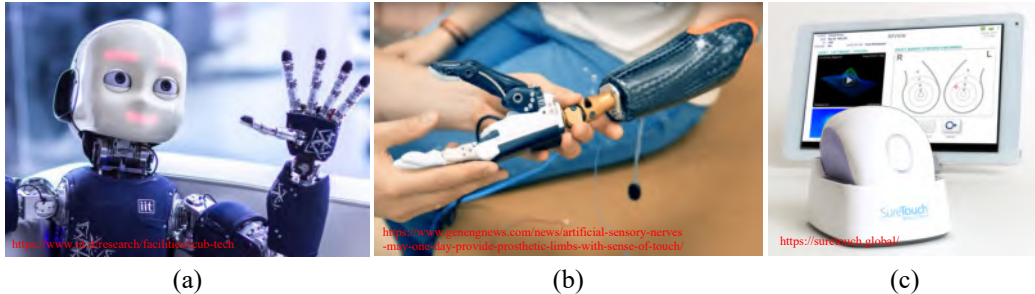


Figure 1.4: Potential applications of artificial tactile skin across multiple domains. (a) Intelligent robots. (b) Prosthetics (c) Medical devices.

feedback meaningful touch information on their hands/fingers, such as the shape of the object, and contact force, enabling robots to manipulate objects accurately and dexterously.

Prosthetics

The artificial skin could lead to the next generation of prosthetics that patients can feel touch, pain, and properties of natural objects if the arm could flash tactile signals to the brain [e.g., Fig 1.4(b)]. The sense of touch is still unavailable on current prosthetic devices, such as fingers, hands, arms, and legs, which are still rigid and far from the sensing functions of human skin. The idea is to enable amputees to receive sensory feedback from their prosthetic limb not only for grasping objects but also to help them to perceive more information about the objects' shapes and the experience of pain, etc.

The artificial skin can give the prosthesis control feedback of contact force distribution on the artificial body surface. Feedback signals to the brain can be transmitted via implanted electrodes by an electrical nerve stimulator, and the neuromorphic signal transduction simulates the changes in the tactile signal with respect to changes in stimulation pulse width and frequency, for instance, matching the perceived levels of touch or pain.

Medical Devices

The tactile skin for medical applications is very promising. For example, endoscopic, surgical robots could use touch sensing to avoid collisions between robots and patients, the direct tactile interaction with human organs could be visualized and displayed on control panels to minimize tissue damage, automatically avoid high forces, or alert about potential harm to the staff.

Artificial skin could be used for physical examination that provides health status and diagnosing disease, for example, the SureTouch device developed by Sure, Inc. shown in Fig. 1.4(c) could create an accurate image of the breast during a breast exam to detect an abnormal mass is cancer or is benign. The tactile sensor can also be embedded into sensing suits, beds, offering robust ways of real-time monitoring, and tracking of healths.

1.2.3 Challenges

The challenges of tactile sensing technology can be introduced as

Flexibility, Durability, and Scalability

The tactile sensors should be mechanically flexible/soft, stretchable, and durable to be wearable/comfortable on a curve 3-D surface, comfortable to touch, and avoid damages due to external impacts, respectively. Since these requirements, the development of a tactile sensor is a very challenging goal that involves many technical issues, including materials, principles, design. Besides, tactile skin structure has to be simple to manufacture and scalable between multiple systems to easily deploy. Artificial skin should be sensitive, multi-modal sensitivity, robust and reliable, since it frequently works in dynamic interaction with various physical contact scenarios.

Large Area Tactile Skin

Robotic tactile skin deployed on the entire body of a robot would require coverage over large areas with a high number of many distributed sensing elements, that have so far prevented an effective utilization of artificial skin technology. All their signals have to be connected, and converted, processed, and transmitted, resulting in solving technical challenges, such as wiring, networking, and data acquisition. Tactile signal transmitting and processing to a control system is also required to implement in real-time to enable fast and safe responses. Besides, a large artificial skin should neither weigh much and consume power much (since a large number of sensing elements increases these significantly).

Tactile Perception and Control

The challenges in tactile sensing technology are not only in the development of devices but also in utilizing tactile feedback for specific applications. The tactile information is inherently bulky and diverse, thus processing, interpreting, and developing the control algorithms with input such information is also a major challenge. For manipulation, the extracted information about contact location, contact geometry, and forces is crucial to grasp objects effectively and safely with desired forces and motions to them. For exploration, high-level tactile information about the object is helpful, including the local geometry, hardness, texture, slip, and friction.

1.3 Research Purpose

To solve the above challenges, the research desires to create a whole-body soft robot with deformable tactile skin that is able to perceive in detail both contact geometry and contact force. To do this, the TacLINK a large-scale tactile sensing system with soft skin based on vision technology is developed

for robotic links. This system is capable of the robust recognition of multiple contacts under conditions of large deformation. Interestingly, the analytical finite element model of the continuous artificial skin was successfully formulated for computation of contact force. The originality of the research can be described as :

- 1) Development of a low-cost, efficient design for robotic links equipped with large-scale tactile force sensing.
- 2) The artificial skin is durable, soft, and comfortable to touch, and can be inflated to change its form by varying air pressure supplied.
- 3) An efficient vision system with robust algorithms for tracking 3-D deformation of an elongated and curved skin based on the views supplied by a stereo camera.
- 4) The finite element method (FEM) approach is used to compute contact force that is generalized in spatial force reconstruction. The proposed vision-based tactile force sensing can be utilized for similar structures.

1.4 Thesis Outline

The thesis introduces the entire development of TacLINK (see Fig. 1.5), from sensing principle, mechanical design, design, fabrication, modeling, implementation of algorithms, and experimental evaluations are presented. The remaining parts of this thesis are divided into six chapters as

Chapter 2 gives a concise overview of the related works on robotic tactile skin, development of artificial skin with their limitations;

Chapter 3 proposes an approach to create an artificial skin system, explains design, fabrication, and principle-based on vision technologies;

Chapter 4 introduces the camera model and calibration method. The algorithms to track markers, and reconstruct the 3-D surface of the skin are also proposed;

Chapter 5 formulates the finite element (FE) model of artificial skin for

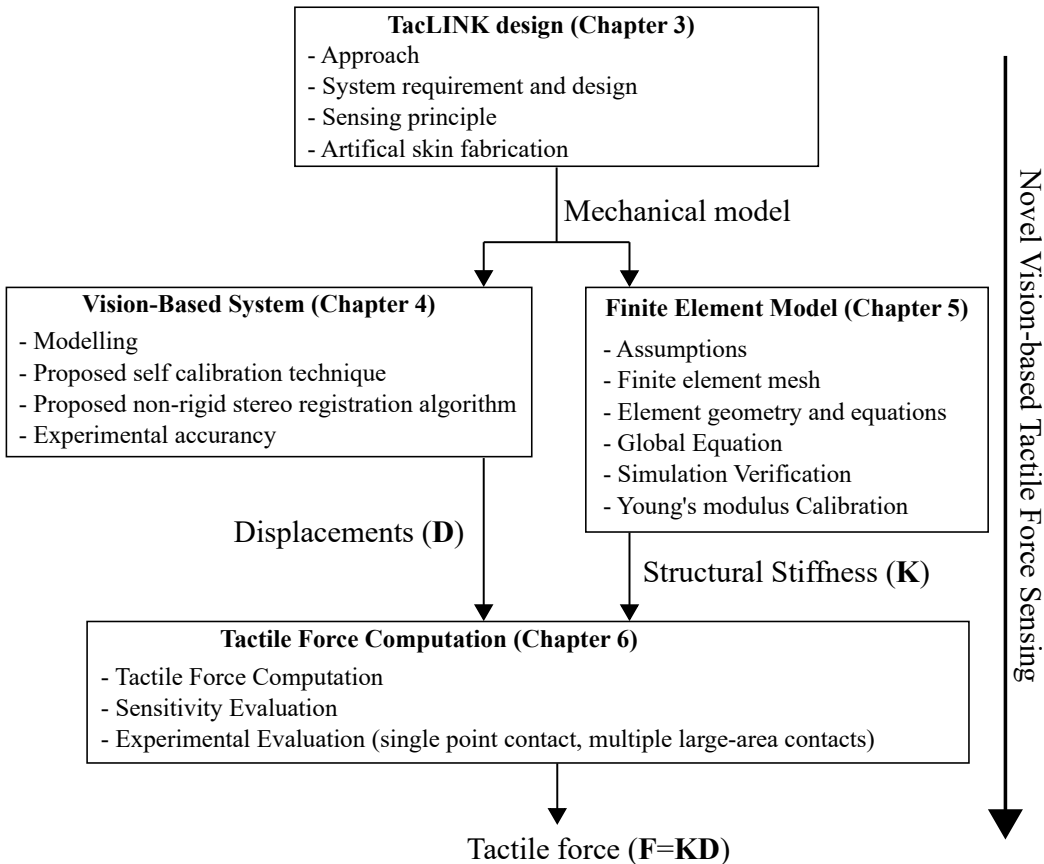


Figure 1.5: Flowchart of TacLINK development.

the evaluation of the skin stiffness and computation of the structural stiffness;

Chapter 6 shows computation, assumptions, experimental results, discussion of tactile force reconstruction;

Chapter 7 concludes the thesis and introduces the outlook of the research in developing large-scale tactile sensing systems.

Chapter 2

Related Work

2.1 Large-Scale Robotic Tactile Skin

Nowadays, the robot is not only confined inside industrial factories within safety fences to operate high speed with accurately repetitive operations. Rather, they are being increasingly developed for utilizing in many activities of human life (e.g., Fig. 2.1). These robots are designed to frequently interact with surrounding objects and humans, especially during physical contacts, which has led to attempts to equip robots with whole-body artificial skin, which can perceive multiple modalities tactile sensations. For instance, robot hands equipped with tactile perceptions, such as object's properties of location, shape, size, and texture, can improve the dexterous manipulation, while a robot body covered with tactile skin can enable high awareness about contact force for safe interaction.

Focusing on artificial robot skin, tactile sensor specifications must not only be sensitive and flexible [28–30], but be highly stretchable and scalable [31–33], enabling them to be wearable on curved and large surfaces of robot's parts, from fingertips to larger areas, such as legs, hands, arms, and body. Tactile sensing devices are normally designed as an array of sensing elements (taxels), whose sensing principles are based on physical transduc-

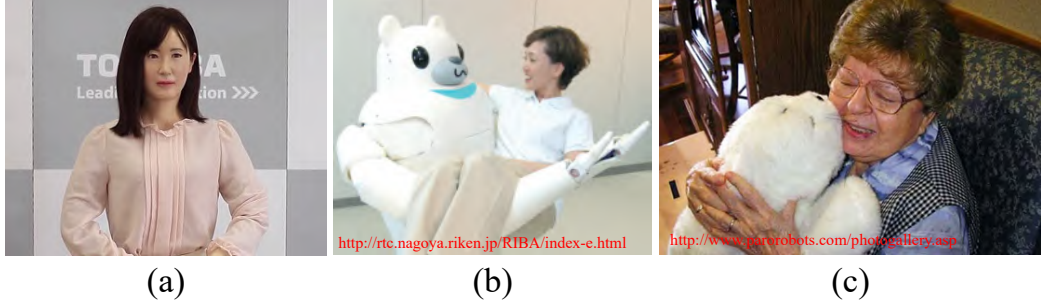


Figure 2.1: Example of robot application in humans life. (a) Toshiba’s humanoid robot. (b) RIBA nursing-care assistant robot. (c) PARO therapeutic robot for use in nursing homes and hospitals.

tion principles, from applied force/pressure to changes in, for instance, resistance, capacitance, piezoelectricity, magnetics, and light density, etc. [34]. Nonetheless, most of these proposed designs focused only on the development of the structure and principle, without considering the technical issues at the system-level design, such as the bulk of wires, power consumption, analog-to-digital converters, and data networking and transmitting, etc. required for a large number of taxels. Also, manufacturing complexity and high cost partly constrain the number of currently available commercial tactile sensors.

To date, few studies have succeeded in covering the surface of the robot with large areas of tactile sensors. As mentioned above, deployment on a large scale deals with technical issues, such as wiring and conformability to non-flat surfaces. At present, the typical designs are the integrated electronic skin formed by many spatially distributed modular sensing points with a microcontroller [35], which is to allow huge amounts of tactile data to be locally processed and sent through a serial bus (e.g., CAN bus, RS485 bus, I²C bus) to tackle wiring challenge. To conform to the curved surface of a robot’s body, the tactile modules are normally the flexible printed circuits [36] [see Fig. 2.2(a)], a mesh of triangularly [10,37] [see Fig. 2.2(b)] or hexagonally shaped printed circuit boards [38] [see Fig. 2.2(c)]. Unfortunately, based on the modular design by integration of various sensors, electronics, and

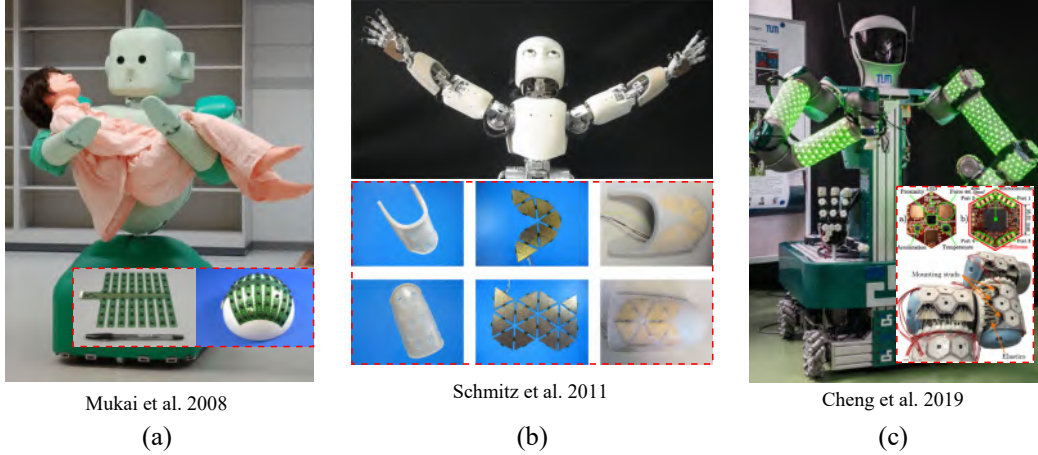


Figure 2.2: Examples of the nearest deployment of whole-body large-scale robotic tactile skin. (a) RI-MAN robot with flexible printed circuits (FPC) skin for human-robot interaction [36]. (b) iCub robot covered with a mesh of triangles printed circuit boards (PCB) [10]. (c) The allegro hand covered by hexagonally shaped PCB skin cells, which can sense multimodal sensing: temperatures, light touch, accelerations, and proximity [38].

microcontrollers, this design approach is low spatial resolution, relatively expensive. Moreover, the electronic components and sensors embedded are rigid but fragile, thus this design is lack mechanical flexibility and not durable if frequently external impacts with the surrounding objects.

2.2 Vision-based Tactile Sensor

Vision-based sensing technology addresses many advantages to artificial tactile skin [39], that the high spatial resolution could be realized, the pixel size is very small and in the order of μm (e.g., $3\mu m$, $5\mu m$, and $12\mu m$), and the pixel resolution of a vision sensor is now from several to 10 megapixels or even much higher. The structure of a vision-based sensor basically consists of three major parts: an elastic membrane skin with physical contact-to-light conversion or color markers, a light source, and a camera. The camera is uti-

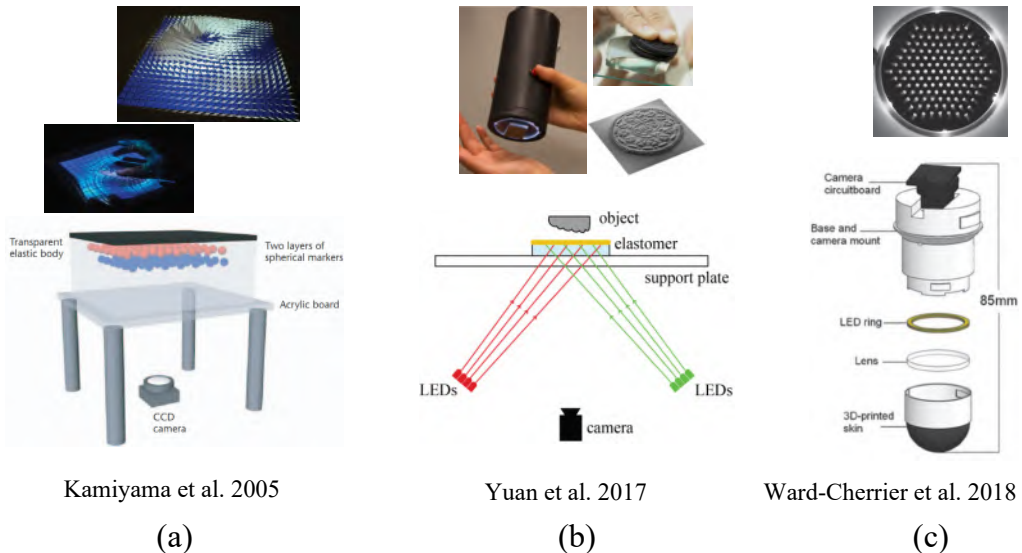


Figure 2.3: Example designs of the vision-based tactile sensor. (a) the GelForce sensor [41]. (b) The Gesight sensor [42]. (c) The TacTip sensor [44].

lized to track the change of the skin and then using a computational model running on the computer to convert the captured image to tactile information, such that vision technology can be utilized to simultaneously sense the deformation of a large area of soft robotic skin without the need to embed any sensing elements in the robotic skin, markedly reducing wires and bulky data acquisition system. However, the major difficulty is to build the computational model, in most cases, an analytical model is very hard to establish due to the nonlinearity of the elastomer materials and complicated contact scenarios, such as multiple contact points.

Various approaches for vision-based tactile sensor were proposed [40], for example, the GelForce sensor [41] consists of a transparent elastic membrane with two layers of colored markers [see Fig. 2.3(a)], whose displacements are tracked by a camera, and the force-displacement relationship was experimentally calibrated. When touching on the surface, this sensor provides the surface's traction field (vector distribution), and then the direction and mag-

nitude of a single point contact could be estimated. In [42], the GelSight can measure detailed surface texture and the 3-D shape of a contacted object [see Fig. 2.3(b)], the sensor consists of a special elastomer surface coated with a reflective coating layer to enhance reflectivity when lighting from the LEDs source. They also used experimental methods to build a lookup table, which maps pixel intensities of the captured images to the geometry gradient of the normal surface.

Recently, the TacTip family [44] for the robot fingertip was addressed with different 3-D shapes [see Fig. 2.3(c)]. A rapid prototyping Objet 3D printer is used to create the TacTip’s skin with an array of markers on the inner wall surface. Although the contact force was not derived, from the observed image, they utilized the machine learning method to output approximated edge of the contact surface, which is useful to perform tactile tasks such as contour following, with potential implications for tactile exploration, tactile manipulation, and object perception. However, most of the aforementioned sensors were designed for fingertip, the scalability of a large area has not yet been determined.

2.3 Vision-based Force Sensing

The vision-based sensing technology still has difficulty in determining a clear relationship between the distribution of applied force and measured deformation of an elastic body. Vision-based force sensing has therefore been investigated, for instance, a fluid-type tactile sensor could estimate the multi-axis contact force from the positions of a dotted pattern [45]. They build the equilibrium equations of the tensional forces on each segment of the elastic membrane to compute the contact force. However, establishing these equations is rather complex, and due to solved by an iteration method, the computation rate is only about 1.0 Hz, which is not fast enough for the basic requirements of a real-time sensing system. Another energy minimization

method [46] was used to match the template to the contour data image of a deformed object, such as a cantilever, microgripper, estimating the distribution of the applied force. The Cauchy problem in elasticity was also proposed to estimate the contact force of a gripper [47]. However, the computational efficiency of these techniques for real-time performance is still a challenge.

The other approaches using machine learning to predict the contact force have been reported [42, 48]. Nonetheless, the machine learning method relies mainly on training data that requires acquiring very huge data samples for every produced sensor. Thus, most of the aforementioned vision-force sensing is basically based on experimental methods and could only proximate the total contact force not provide the distribution of applied force on a large artificial skin area.

Recently, the external forces on soft robots have been investigated [49], the surface of the soft objects are stuck with some markers, whose displacements are tracked by a commercial optical tracking system. The mechanical model of the object is built on SOFA (Simulation Open Framework Architecture), an open-source framework for physics-based simulations. The position of these markers on the real object is compared with the corresponding points in the simulation environment to determine the intensities of the external forces acting at these points by solving an inverse problem. However, the required vision system here is expensive and not compact, and the force-sensing technique is rather complex with some limitations.

2.4 Summary

At present, despite the significant development in tactile sensing technology, their effective deployment, and utilization in real applications still require further improvements, especially for deploying large-scale systems on curved surfaces and solving system-level issues, such as wiring, data networking, power consumption, as well as the production cost.

This research adopts the advantages of the vision technology to create a whole-body soft tactile sensing system for the robotic link, which is a part frequently contacting with the environment. The developed system is scalable in size, durable in operation, but very low in cost.

Chapter 3

TacLINK: Large-Scale Vision-Based Tactile Sensing for Robot Links

3.1 Approach

Nowadays, robots share their workspace with humans, posing significant challenges for avoiding dangerous collisions, and interacting and collaborating both at the physical and cognitive levels in a safe manner. Effective strategies include using flexible mechanisms [50] or elastic actuators [51,52] to limit potential injury situations for humans. Nonetheless, such strategies increase the complexity of the mechanical structure and control problem, resulting in reducing the performance of the system.

Artificial robot skins currently can provide a variety of meaningful sensory information that can be applied to many intelligent control algorithms. By utilizing the robotic skin the safety of robots can be obtained without the need of modifying the robot's mechanical structure. Thus, research is motivated by a desire to develop a tactile sensing system with soft and deformable skin for robot links, called TacLINK (see Fig. 3.1) that perceives detailed

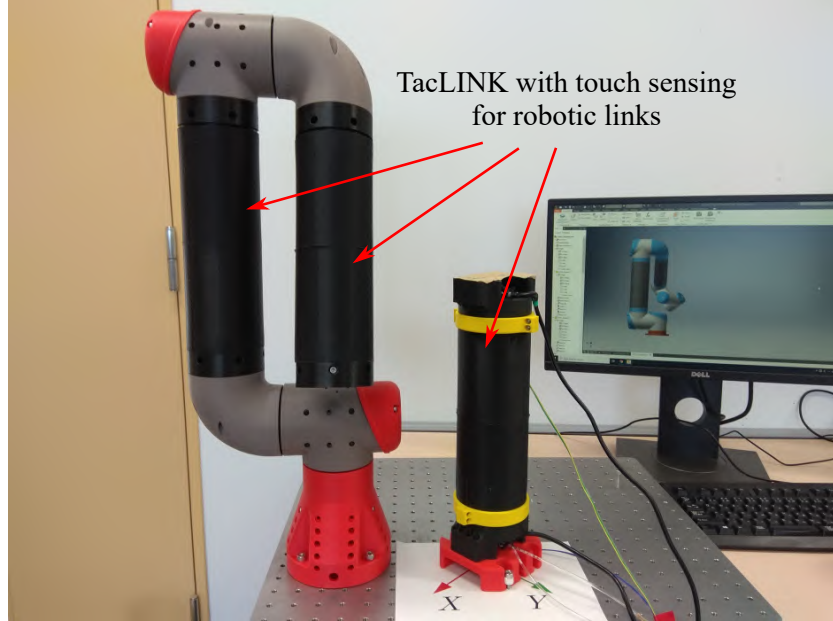


Figure 3.1: A prototype of a robotic arm with tactile sensing links.

contact geometry and contact force during dynamic interaction between the robot and their environments. TacLINK is expected to be widely exploited for smart designs of robotic arms, humanoid robots, and prosthetics, etc.

3.2 System Requirement and Design

3.2.1 Mechanical Design

Figure 3.2 depicts a cross-section view of the mechanical design of the TacLINK showing the overall interior structure. TacLINK is a hollow cylindrical shape of radius 40 mm and height 280 mm. The system consists of a transparent acrylic tube, an artificial skin, two cameras, LEDs, and supporting structures. Specifically, a hollow tube with transparent acrylic materials acting like a skeletal frame is to maintain its rigid structure (see Fig. 3.2). The inner and outer diameters of the tube are $D = 30$ mm, $d = 24$ mm, respectively.

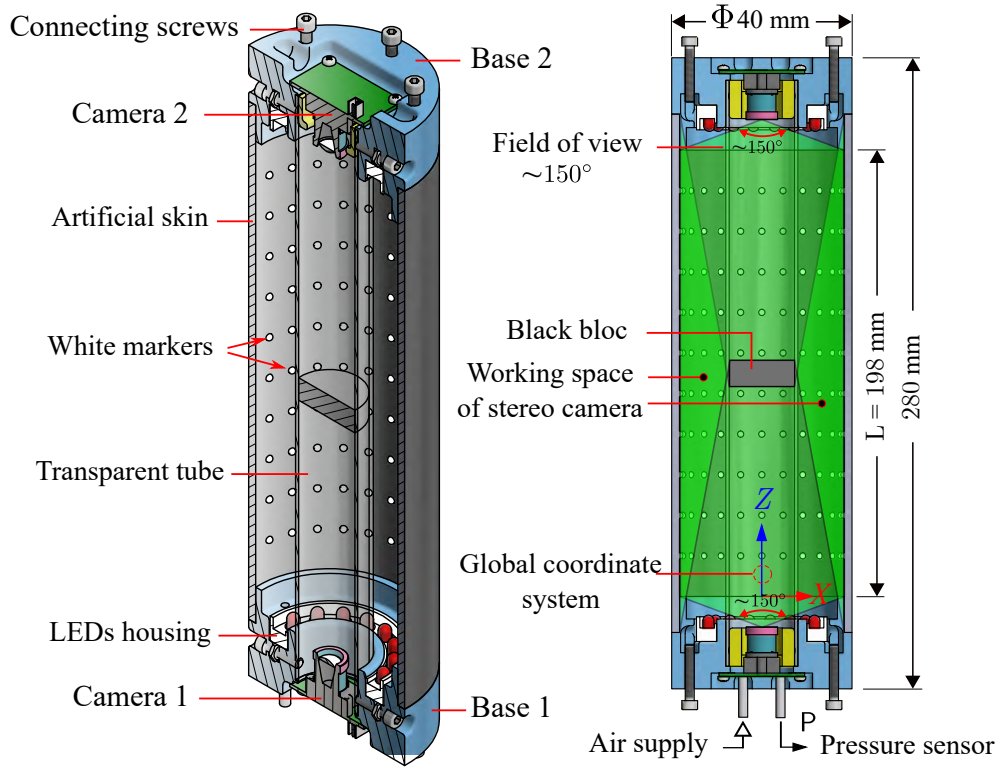


Figure 3.2: Structure of the proposed TacLINK (cross-section view).

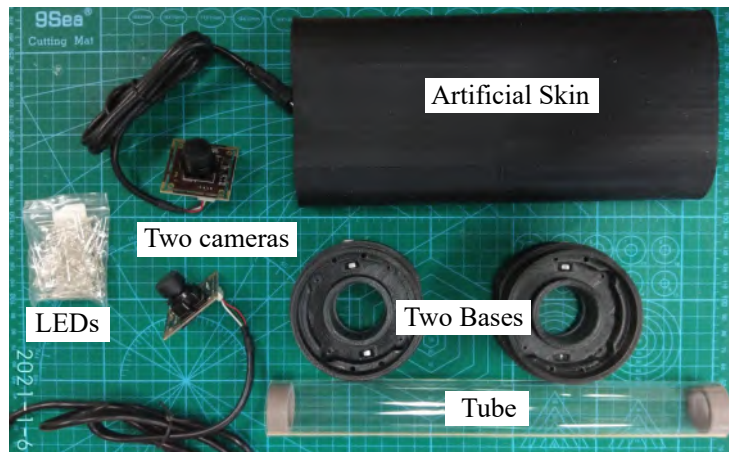


Figure 3.3: The main components for building the TacLINK.

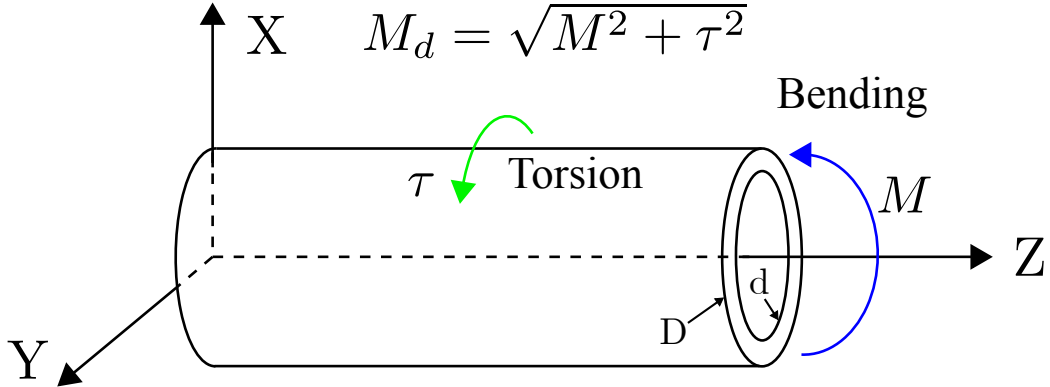


Figure 3.4: A tube subject to bending and torsional moments.

Although the working load limit of TacLINK is reduced compared with metal materials, we can choose suitable dimensions D and d for specified applications (see Fig. 3.4). If M_d is the working load design moment that combines bending and torsional behavior, and $[\sigma]$ represents the permissible stress, the strength condition of the tube can be expressed as [53]

$$W = \frac{\pi}{32} \frac{D^4 - d^4}{D} \geq \frac{M_d}{[\sigma]}, \quad \text{with } [\sigma] = \frac{\sigma_u}{k}, \quad (3.1)$$

where W , σ_u , and k are section modulus of the tube, ultimate strength of materials (acrylic material $\sigma_u = 87 \text{ MPa}$), and safety factor. On the other hand, from Eq. 3.1, we can determine the working load of TacLINK as follows

$$M_d \leq \frac{\pi}{32} \frac{D^4 - d^4}{D} \frac{\sigma_u}{k} = \frac{\pi}{32} \frac{0.03^4 - 0.024^4}{0.03} \frac{87 \times 10^5}{1.5} = 90.7 \text{ Nm}, \quad (3.2)$$

Thus, with $k = 1.5$, the moment working load of TacLINK is $M_d \leq 90.7 \text{ Nm}$.

To ensure the highly deformable, and durable characteristics, TacLINK is covered by a soft artificial skin (with large sensing area $\pi \frac{OD^2}{4} L = \sim 49,763 \text{ mm}^2$) made by black silicon rubber to completely isolate ambient light to the inner space (see Fig. 3.2 and 3.3). To track the deformation of artificial skin, a pat-

Model	ELP USBFHD01M-L21
Sensor	OV2710
Sensor Size	1/2.7 inch
Pixel Size	3µm × 3µm
Image area	5856 µm × 3276 µm
Max. Resolution	1920(H)×1080(V)
Compression format	MJPEG / YUV2
Resolution and frame	VGA@ 640×480, YUV2@ 30fps
Lens Parameter	~ 150 Degree
USB protocol	USB2.0 HS/FS

Table 3.1: Camera specifications.

tern of 240 white markers locates on the inner wall of the skin. The markers are hemisphere with a diameter of $D_{\text{marker}} = 2.8 \text{ mm}$. The skin is attached firmly to the two base parts to totally seal the space between the skin and the tube. An inlet supplies air to the inner space, and an outlet is connected to an external pressure sensor. By changing the inner air pressure (ranging from 0 to 1.5 kPa) can actively inflate the skin, resulting in a different form and sense of stiffness.

3.2.2 Vision System Design

The vision system is to track the 3-D deformation of skin based on measuring the 3-D displacement of all markers, which are the nodes of the finite element model of artificial skin. Normally, the RGB-D cameras or depth sensors can be utilized to provide the information of 3-D position with accuracy from mm to cm. However, these kinds of sensors, which are only effective with a facing surface (due to limitation of view angle $\sim 70^\circ$) in a rather far distance (e.g., RealSense camera D455 is range from 0.4 m to 20 m), thus, installing in inner space of a hollow cylinder surface of TacLINK is unsuitable. Therefore, TacLINK uses two facing cameras with a wide view angle ($\sim 150^\circ$), each camera is located on each end to capture entire markers.

For the implementation of the vision system, note that using checkerboard patterns on the skin surface to apply the general stereo theory can derive the deformation of the skin. However, in this sensing system, note that only positions/displacements of nodes of the finite element model are useful for tactile force computation, resulting in the necessity in designing and simplification in fabricating the pattern of markers that coincide with the nodes of the finite element mesh. Here, the markers are equally distributed to ensure the stable operation of the tracking algorithm, as well as conveniently modeling the skin.

Here, the camera needs to be small but wide-angle range. The selected USB fisheye CMOS camera with model ELP USBFHD01M-L21 is low-cost (about US50\$) but satisfies all the designed requirements with specifications shown in Table 3.1. The used resolution of the camera is 640×480 effective pixels, and the frame rate is about 30 fps (frames per second) for the YUV2 format that realizes real-time measuring. For illumination, an array of white LEDs (size 3 mm with viewing angle about 30°) is mounted circularly on a 3-D printed housing located on every two ends that are base parts used to connect between TacLINK and the external joints of the robot arm (see Fig. 3.1 and 3.2).

Note that to capture the marker movement clearly, the LED sources should use the polarizing filter to produce uniform light and minimize the reflected light from the transparent acrylic plate and the skin surface. In addition, the system has two facing cameras, thus a black bloc is set in the middle of the acrylic tube shown in Fig. 3.2 to block the undesired direct light from the light source to the opposite camera. Here, the location of the camera is calculated to ensure the field of view $\sim 150^\circ$ of each camera covering all the inner space of the skin (see Fig. 3.2). Note that to ensure the detectable ability of the digital camera, the design length of the skin should

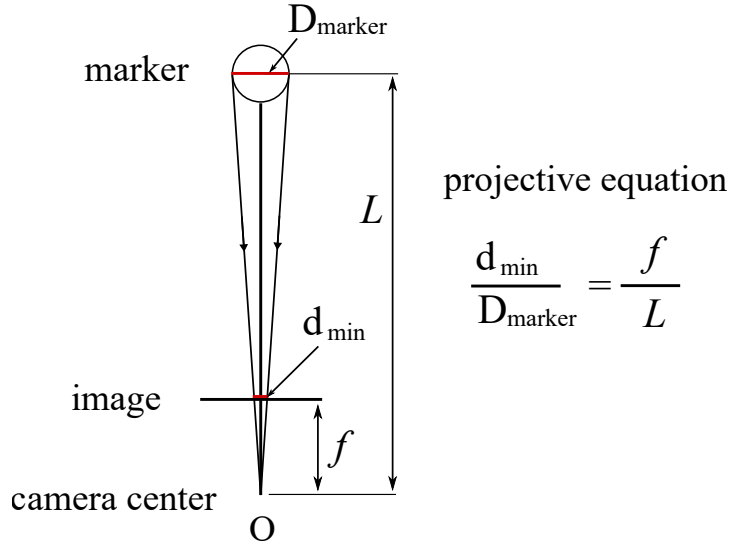


Figure 3.5: The observed size of a marker on the camera.

satisfy the following condition (see Fig. 3.5):

$$L < f \frac{D_{\text{marker}}}{d_{\min}} = 226.5 \frac{2.8}{3} = 211 \text{ mm} \quad (3.3)$$

where f is the focal length of a camera in pixels (see Table. 4.1), and d_{\min} is the minimum detectable pixel size of a marker on the computer image. Here, the length of the skin $L = 198$ mm was chosen.

Besides, increasing the diameter ID of TacLINK results in increasing the blind-zone on the total length of TacLINK (see Fig. 3.6) that should be considered to choose suitable sizes (length and diameter) for a specific application. The length of the blind zone on each side can be determined as

$$L_{\text{blind}} = \frac{ID}{2} \cot \frac{\alpha}{2} \quad (3.4)$$

where α is the view angle of the camera. In this research, the diameter of TacLINK was chosen based on the size of the UR5 robot with the purpose to be replaceable for this robot. Here, $L_{\text{blind}} = \frac{73}{2} \cot \frac{150^\circ}{2} = 9.7$ mm.

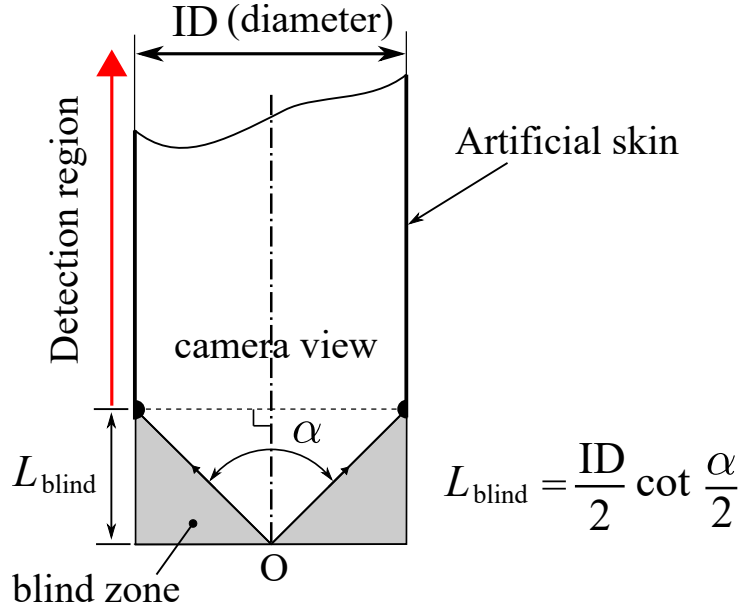
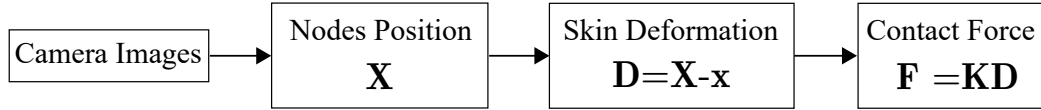


Figure 3.6: The dead zone of the camera.

3.3 Sensing Principle

The tactile sensing principle of TacLINK is simple as shown in Fig. 3.7. There two co-axial cameras installed at both sides (stereo camera) are to increase the observation ability for the elongated skin surface. Such stereo camera tracks the skin deformation by capturing stereo pictures that contain projections of markers, from which the camera model and algorithms are proposed to calculate accurately the three-dimensional (3-D) positions of all markers on a global coordinate system. Next, the deformation of the skin is determined by calculating the displacements of these markers.

Remarkably, to describe the relationship between measured markers displacement and the contact force, this research utilizes the finite element method (FEM) to model the elastic artificial skin, which is divided into a mesh of rectangular elements (each element has four nodes). The free nodes are the markers tracked by the camera, and the fixed nodes are clamped at two ends of the skin. Since the finite element (FE) model provides the



X the vector of nodes position (on FE mesh) with initial positions vector \mathbf{x}

D the vector of nodes displacement

K the matrix of the skin stiffness

F the vector of tactile force/external force

Figure 3.7: Vision-based tactile force sensing principle of TacLINK.

Material	Ecoflex™ 00-50
Specific Gravity	1.07 g/cc
Tensile strength	315 psi
Mix Ratio By Volume/Weight	1A:1B
Mixed Viscosity	8,000 cps
Cure Time	3 hours

Table 3.2: Material specifications (Ecoflex™ 00-50, Smooth-On Inc., USA).

structural stiffness matrix, the external force vector is determined in a linear relationship with the displacement vector (see Fig. 3.7). As a result, the distribution of contact force/tactile force on the skin surface can be treated as the acting concentrated force deriving from the nodal forces of the finite element force vector.

3.4 Artificial Skin Fabrication

TacLINK perceives tactile information through its skin, thus, the properties of the elastomer play an important role in the mechanical characteristics (e.g., softness, stretchability, and durability) and can largely affect the sensing range and sensitivity. A good choice for the elastomer skin material is good elasticity and low mixed viscosity. Here, the material chosen to fabricate is silicone rubber material Ecoflex00-50 (Smooth-On Inc., USA), whose

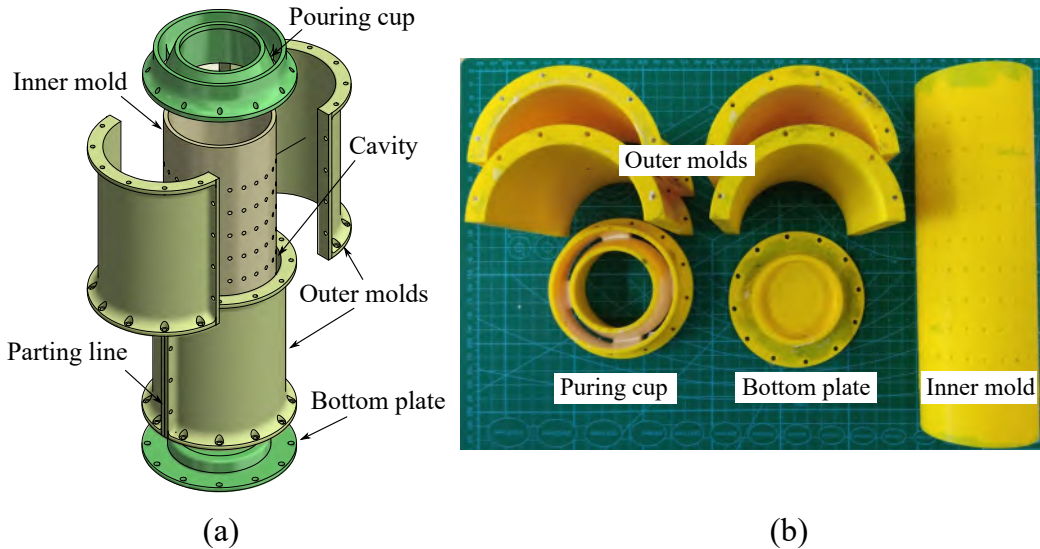


Figure 3.8: (a) CAD design of the mold. (b) The printed parts of the mold.

specifications are shown in Table 3.2.

Besides, the thickness is also an important property for the skin design i.e., a thick elastomer skin can carry out a larger degree of deformation. Here, the artificial skin is designed $t = 3.5$ mm in thick. The artificial skin is a hollow cylindrical shape with a pattern of markers sitting on the inner wall fabricated by the casting technique that is described as below:

1) Molding

Mold is a hollowed-out (cavity) block that shapes an object filled with a liquid material to make the model of the final object. Here, the parts of mold for artificial skin were built-in 3-D computer-aided design (CAD) Autodesk Inventor software (Autodesk Inc., USA) shown in Fig. 3.8(a), note that the design process can be designed in any modern CAD software. The part is then exported as a stereolithography (.STL) file for 3-D printing software. We used Z-SUITE software to prepare the printing file for a 3-D printer (M200, Zortrax S.A., Poland) that uses the Z-ABS material. The entirely

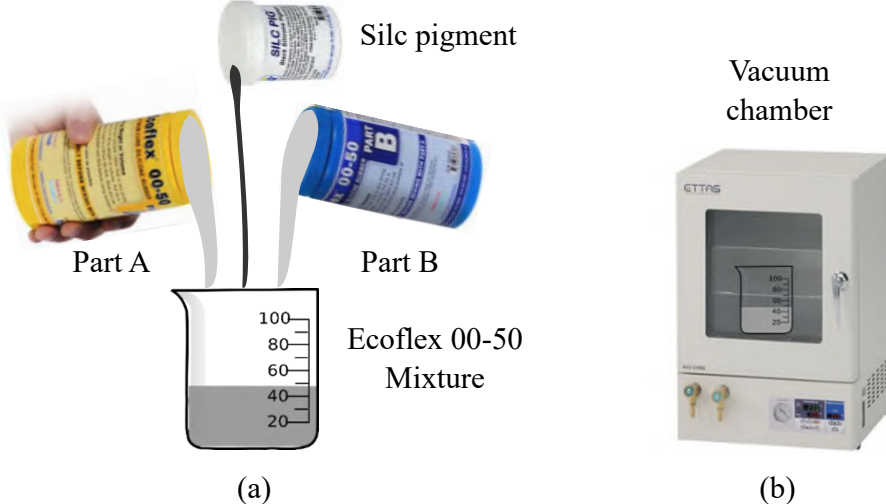


Figure 3.9: (a) Mixing the Ecoflex 00-50 materials of part A: part B with Silc pigment (black color for the skin body and white color for markers). (b) Degassing the silicone mixture in a vacuum chamber.

actual 3-D parts of the mold are shown in Fig. 3.8(b), including seven pieces i.e., inner mold (1 piece), outer molds (4 pieces), the bottom plate (1 piece), and top mold (1 piece) that is funnel-shaped and customized as a pouring cup.

2) Mixing silicone

The skin is made from silicone Ecoflex00-50 of parts A and B which are measured and mixed at an equal volume or weight (1:1 mix ratio) shown in Fig. 3.9(a). The desired pigment is also incorporated during the mixture of part A and Part B, here, the markers use white pigment and the skin body uses black pigment. The silicone mixing process should be implemented slowly and steadily for a short period of time because overmixing can cause a lot of air bubbles. Then, the mixture is placed into the vacuum chamber [see Fig. 3.9(b)] for degassing because the stirring process might generate some bubbles, which are harmful to the elastomer performance.

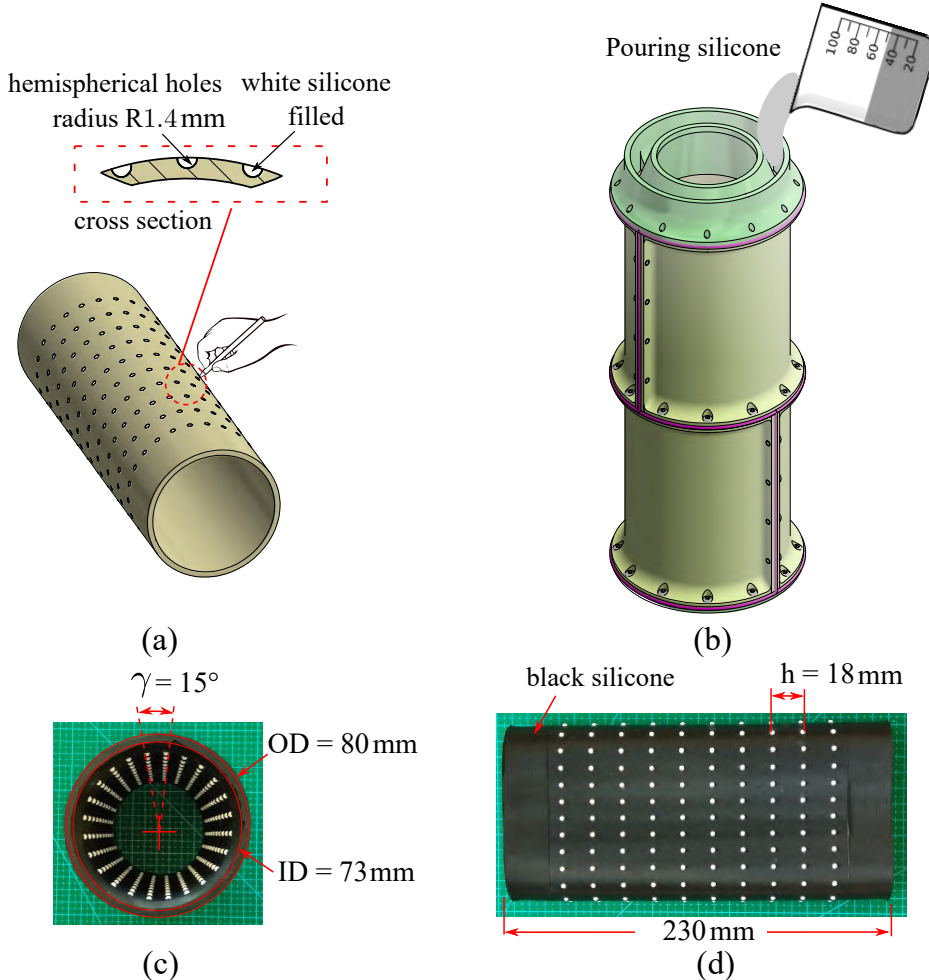


Figure 3.10: Casting mold for skin fabrication. (a) The 3-D printable casting mold. (b) Filling female holes of the inner mold with white silicone to cast the markers array. (c) The actual soft skin body after fabrication with distributed markers. (a) Top view. (b) Inside view.

3) Casting Process

Step 1: Casting markers

To cast the markers, an array of hemispherical holes, of radius 1.4 mm and pitch $18 \text{ mm} \times 15^\circ$, is printed on the outer surface of the inner mold (see Fig.

3.8). Once the Ecoflex mixture with white Silc pigment is ready. A stick is used to fill carefully white silicone onto these holes, as illustrated in Fig. 3.10(a).

Step 2: Assembling mold

After the white markers were formed, all parts of the mold are assembled. We use screws/nuts to assemble the parts. In order to avoid uncured silicone from leaking out during casting, we seal boundaries of parting lines with a thin layer of silicon.

Step 3: Pouring silicone

After the silicone parts have been mixed, slowly pour the silicone into the mold through the purring cup. Then leave the silicone at room temperature to cure within 24 h

Step 4: Demolding the skin

After the silicone is completely cured. Carefully use a knife to peel off outer molds. Finally, the skin body was removed manually from the casting mold. Fig. 3.10(c) shows the prototype of artificial skin with actual markers evenly distributed.

3.5 Summary

In this chapter, we introduced the design of TacLINK that is a large-scale vision-based tactile sensing system, built for robotic links. The mechanical design of TacLINK is revealed with two main components of the stereo camera and artificial skin. The artificial skin is soft and deformable with a dotted pattern inside without embedding any electronic components, enabling high durability of the proposed design during physical interaction with environments. The casting method with silicone materials for skin fabrication is also introduced. To sum up, we introduced our novel sensing system that is cost-effective, easy to manufacture, and highly scalable for other systems.

Chapter 4

Vision-Based Modeling

4.1 Stereo Camera Model

The objective of the vision-based system is to construct the 3-D shape of the soft skin by tracking the position of markers located on the inner skin surface. The camera is modeled by a usual pinhole [54], and the digital vision sensors assumes to be square in shape i.e., the focal lengths in pixels on the x - and y -axes are similar $f_x = f_y = f$ that is true for almost any digital camera.

Fig. 4.1 illustrates the proposed stereo vision system consisting of two coaxial cameras that form as a stereo camera. Its baseline/optical axes along the centerline of the skin surface. The Z-axis of the world (global) coordinate system (WCS) is concise the baseline, and its origin located at the center of the first end (on the side of camera 1) [see Fig. 4.1(a)]. The coordinates of 3-D point P presented in the world coordinate space is

$$P = \begin{bmatrix} X \\ Y \\ Z \end{bmatrix} \in \mathbb{R}^3 \quad (4.1)$$

which is captured by stereo cameras and two projected 2-D points on two

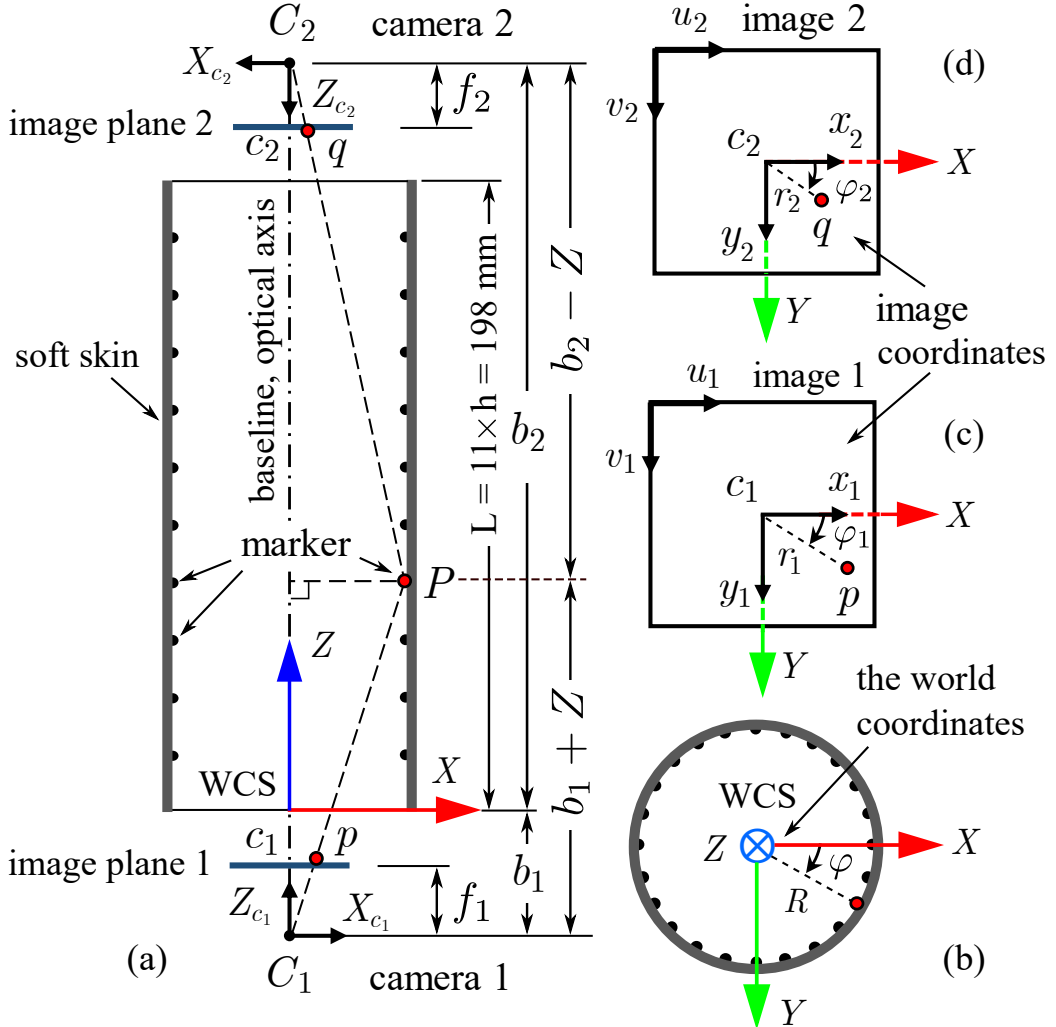


Figure 4.1: Configuration of the stereo vision system (stereo camera). The world coordinate system (WCS) is XYZ , whose Z -axis locates on the baseline that is the centreline of the skin. Its origin coincides with the center of the first end, and its X -axis is parallel to the X_{c_1} -axis and anti-parallel X_{c_2} -axis of the camera frames. Note that the image of camera 2 was inverted about its y_2 -axis to unify the direction of the coordinates of the two images. Thus, the image coordinates on the x_1/x_2 - and y_1/y_2 -axes are in the same directions as the X and Y -axes of WCS, respectively.

image planes are

$$p = \begin{bmatrix} x_1 \\ y_1 \end{bmatrix} \in \mathbb{R}^2, \quad q = \begin{bmatrix} x_2 \\ y_2 \end{bmatrix} \in \mathbb{R}^2, \quad (4.2)$$

where $\{x_1, y_1\}$ and $\{x_2, y_2\}$ are the image coordinate systems of image 1 and image 2, respectively [see Fig. 4.1(a)].

Based on the geometric relationships shown in Fig. 4.1(a), the stereo camera model describing the relationship between the position of a 3-D point P and their projections of 2-D points p and q is given as

$$\begin{bmatrix} x_1 \\ y_1 \end{bmatrix} = \frac{f_1}{b_1 + Z} \begin{bmatrix} X \\ Y \end{bmatrix}, \quad (4.3)$$

$$\begin{bmatrix} x_2 \\ y_2 \end{bmatrix} = \frac{f_2}{b_2 - Z} \begin{bmatrix} X \\ Y \end{bmatrix}, \quad (4.4)$$

with the image coordinates are determined from the computer image coordinates u_1, v_1 and u_2, v_2 are

$$x_1 = u_1 - c_{x_1}, \quad y_1 = v_1 - c_{y_1}, \quad (4.5)$$

$$x_2 = u_2 - c_{x_2}, \quad y_2 = v_2 - c_{y_2}. \quad (4.6)$$

where f_1 and f_2 correspond to the focal lengths of the two cameras in pixels, and $c_1(c_{x_1}, c_{y_1})$ and $c_2(c_{x_2}, c_{y_2})$ are the pixel locations of the principal points on the two pixel coordinate systems, $\{u_1, v_1\}$ and $\{u_2, v_2\}$, respectively.

From Eqs. 4.3–4.6, the proposed stereo vision can be fully modelled by four intrinsic parameters $\{f_1, f_2, c_1, c_2\}$ and two extrinsic parameters $\{b_1, b_2\}$. The intrinsic distance b_1 and b_2 denote the position of WCS origin in two camera frames $X_{C_1}Y_{C_1}Z_{C_1}$ and $X_{C_2}Y_{C_2}Z_{C_2}$, respectively [see Fig. 4.1(a)]. To determine such parameters, the method for self-automatic calibration is introduced in Section 4.7.

The stereo problem now is to determine the 3-D location of a point through information supplied by the two cameras. For convenience, Carte-

sian coordinates are converted to polar and cylindrical coordinates on the image and world coordinate systems, respectively, in which R and φ represent radial and angular coordinates of WCS, as shown in Fig. 4.1.

The other form of Eq. (4.3) can be expressed as:

$$r_1 = \frac{f_1}{b_1 + Z} R, \quad (4.7)$$

$$r_2 = \frac{f_2}{b_2 - Z} R, \quad (4.8)$$

where r_1 and r_2 are the observed radial coordinates, and the angular coordinates φ_1 and φ_2 (two arcs from $-\pi$ to π) of two image coordinate systems are calculated from data supplied by the two cameras as

$$r_1 = \sqrt{x_1^2 + y_1^2}, \quad \varphi_1 = \arctan 2(y_1, x_1), \quad (4.9)$$

$$r_2 = \sqrt{x_2^2 + y_2^2}, \quad \varphi_2 = \arctan 2(y_2, x_2). \quad (4.10)$$

The solutions of Eqs. (4.7) and (4.8) can be derived as follows:

$$Z = \frac{f_1 b_2 r_2 - f_2 b_1 r_1}{f_1 r_2 + f_2 r_1}, \quad (4.11)$$

$$R = (b_1 + b_2) \frac{r_1 r_2}{f_1 r_2 + f_2 r_1}. \quad (4.12)$$

Figure 4.1 indicates that the ideal angular coordinates obey the relationship as $\varphi = \varphi_1 = \varphi_2$. In fact, the angular φ_1 and φ_2 may slightly differ, because of mechanical misalignment of the axes x_1 and x_2 of the two installed cameras. Because cameras are fixed, thus this discrepancy is constant, and compensation factors can be used to correct. The angular coordinate could be approximated as $\varphi = \frac{1}{2}(\varphi_1 + \varphi_2)$.

However, because the angular coordinates discontinue at $-\pi$ and π , φ

can be calculated as

$$\varphi = \begin{cases} \frac{1}{2}(\varphi_1 + \varphi_2) & |\varphi_1 - \varphi_2| < \pi \\ \frac{1}{2}(\varphi_1 + \varphi_2) - \pi \text{sign}(\varphi_1 + \varphi_2) & |\varphi_1 - \varphi_2| > \pi \end{cases} \quad (4.13)$$

After φ is obtained, coordinates X and Y can be calculated:

$$X = R \cos(\varphi), \quad (4.14)$$

$$Y = R \sin(\varphi). \quad (4.15)$$

It should be noticed that the solution of stereo triangulation is presented by Eqs. (4.11), (4.14), and (4.15) that are straightforward relations. The stereo camera model is reasonably simple to enable the implementation of the proposed 3-D vision-based system performing in real-time.

4.2 Uncertainty Analysis

The goal of this section is to analyze the uncertainty of stereo reconstruction, relating to the effects of camera parameters. This content can help to optimize the best working space to select and evaluate the design. In particular, the detectability in both images associates with two types of possible errors on i.e., quantization error and localization error [55]. Because this vision-based system is to detect the location of markers, only localization error is considered. When observing and extracting the locations of the features, the uncertainty of localization associates with the specifications of the vision camera configurations (pixel size, lens), and stereo processing methods (image processing algorithms, and markers detection method).

For the ease of analysis, the localization error is characterized by the sensitivity of imaging parameters to errors that associates to the projections $p(r_1, \varphi_1)$ and $q(r_2, \varphi_2)$. Let Δr_1 and Δr_2 be the image plane coordinate error variables, which are independent from each other. The standard deviation

of pixel error of a digital camera varies from 0 to 1 pixels, therefore, the normalized error variables Δr_1 and Δr_2 of the radial coordinates are uniformly distributed within the interval $[-\frac{\sqrt{2}}{2}, \frac{\sqrt{2}}{2}]$ pixels [55].

To analysis, the calibrated stereo parameters are assumed to be determined beforehand as presented in Section 4.7. From Eqs. (4.11) and (4.12), taking the derivative of the coordinate Z and the radial coordinate R with respect to radial image coordinates r_1 and r_2 , the uncertainty of ranges Z and R are obtained as

$$\Delta Z = f_1 f_2 \frac{b_1 + b_2}{(f_1 r_2 + f_2 r_1)^2} (-r_2 \Delta r_1 + r_1 \Delta r_2), \quad (4.16)$$

$$\Delta R = \frac{b_1 + b_2}{(f_1 r_2 + f_2 r_1)^2} (f_1 r_2^2 \Delta r_1 + f_2 r_1^2 \Delta r_2). \quad (4.17)$$

Substituting variables r_1 and r_2 from Eqs. (4.7) and (4.8) into Eqs. (4.16) and (4.17) yields in the expressions of uncertainties as below

$$\Delta Z = \frac{(b_2 - Z)^2 (b_1 + Z)}{f_2 (b_1 + b_2) R} \Delta r_2 - \frac{(b_2 - Z) (b_1 + Z)^2}{f_1 (b_1 + b_2) R} \Delta r_1, \quad (4.18)$$

$$\Delta R = \frac{(b_1 + Z)^2}{f_1 (b_1 + b_2)} \Delta r_1 + \frac{(b_2 - Z)^2}{f_2 (b_1 + b_2)} \Delta r_2, \quad (4.19)$$

where $Z \in [0 L]$, $R \in [R_{\min} R_{\max}]$ are in the working ranges of the system.

According to Eqs. (4.18) and (4.19), the localization errors are non-linear in assessing the misalignments of normalized pixel deviations Δr_1 and Δr_2 that distribute within the interval of erroneously perturbed $[-\frac{1}{\sqrt{2}}, \frac{1}{\sqrt{2}}]$ pixels, thus, the highest uncertainties in ranges of ΔZ and ΔR in the designed working space are depicted in Fig. 4.2.

Fig. 4.2(b) indicates that the uncertainty ΔR depends solely on the Z -coordinate, with greater certainty (accurate detection) in the middle region of the skin (i.e., near the center plane $Z = \frac{L}{2}$). Generally, markers located in the middle region tend to be detected and measured in R -direction with higher

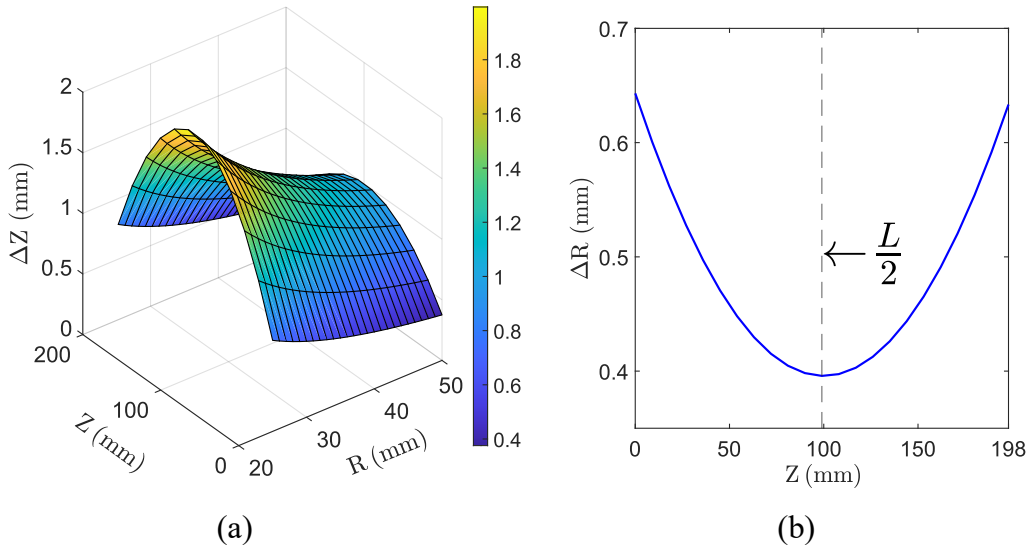


Figure 4.2: Stereo uncertainty evaluation results illustrating the highest variations of error in the working space. (a) Uncertainty of Z coordinate with deviations $\Delta r_1 = -1/\sqrt{2}$, $\Delta r_2 = 1/\sqrt{2}$. (b) Uncertainty of radial coordinate ΔR with deviations $\Delta r_1 = 1/\sqrt{2}$, $\Delta r_2 = 1/\sqrt{2}$.

accuracy than markers locating near the two ends (far the center plane). On contrary, the range uncertainty ΔZ is more complex and varies on the whole working space as shown in Fig. 4.2(a), it indicates that ΔZ is dependent on both Z - and R -directions. The uncertainty ΔZ increases significantly on the middle but reduces on the positive direction of R . Therefore, markers close to the two ends (near the camera plane) and away from the baseline (centerline of the skin) can be detected and localized with higher accuracy of Z -direction.

Moreover, equations (4.18) and (4.19) indicate that the certainty of this vision system could be enhanced by increasing digital focal lengths f_1 and f_2 in pixels (reducing the variations ΔZ and ΔR), which are obtained by installing camera with smaller pixel size, or adjusting the focal length of the lens (note that the latter will reduce the field of view of the lens).

4.3 Image Processing

In the previous sections, the stereo camera model and the uncertainty of 3-D measurement are introduced. The three-dimensional positions of markers are calculated from the two-dimensional positions of the markers in images captured by the stereo camera. The accuracy of the proposed vision sensing system would therefore also depend on the detection of the markers in the computer images. Here, the image processing method with MATLAB built-in functions is utilized to detect accurately the position of markers. The image processing technique shown in Fig. 4.3 is described by the following two steps:

Step 1: The stereo images are captured from two cameras by using the MATLAB built-in function, i.e, `frame = snapshot(cam)`. The `snapshot` function returns the current frame that is called in a loop to receive a new frame each time. The frame rate of camera in YUV2 format and resolution of 640×480 pixels² is 30 fps, while the captured frame rate is about 15 Hz.

The returned images are RGB color images that are preprocessed by removing the undesired bright areas [see Fig. 4.3(a) and (b)], then using the standard image processing algorithms to enhance the contrast of markers and transform them into a grayscale image i.e., `img = rgb2gray(frame)`.

Step 2: The principal points of two images are different so that to uniform the geometry and size of the image, the center square area of 400×400 pixels² at the principal points c_1 and c_2 on each stereo image is cropped to process, as shown in Fig. 4.3(b).

The regions of the white marker are extracted by using a threshold to binarize the grayscale image. The position of each marker is obtained by calculating the centroids of the markers area i.e., `Φ = regionprops(img,'centroid')`.

The positions of the markers have been obtained, however, the extracted sets of 2-D marker points $Φ_1$ and $Φ_2$ from stereo images are the unorganized sets [see Fig. 4.3(c)]. In order to obtain the 3-D positions, the markers must be identified and matched between two stereo images.

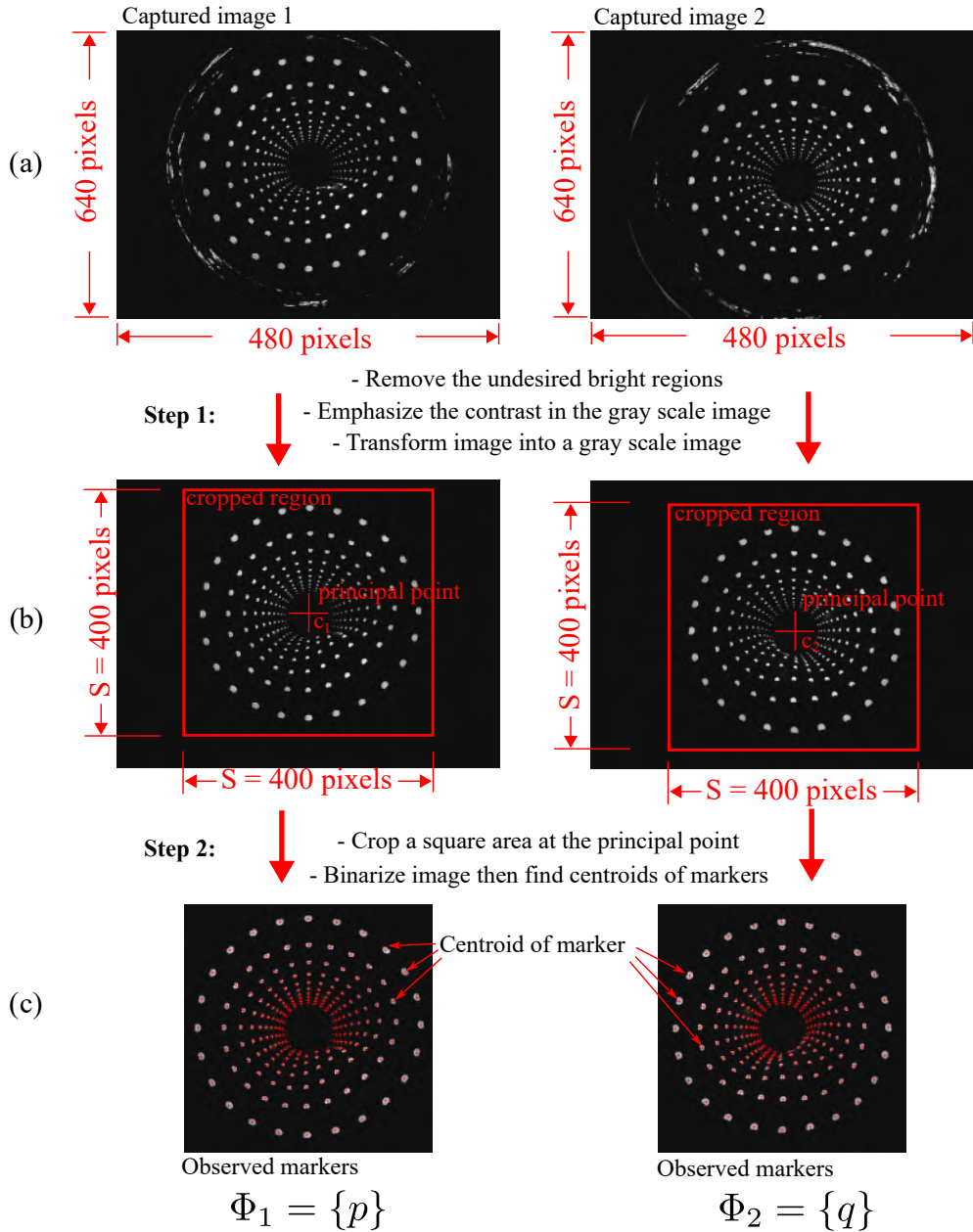


Figure 4.3: Image processing for marker detecting in captured images. (Left) Image processing of camera 1. (Right) Image processing of camera 2.

4.4 Notations and Marker Numbering

The stereo vision is designed to provide the 3-D positions of all nodes on the finite element mesh 24×11 of the skin shown in Fig. 4.6 and 5.6. Let $\ell \in \{1, \dots, n_1\}$ denotes the path and $j \in \{0, \dots, n_2\}$ represents the cell, which correspond to the grid locations on the φ -axis and Z -axis in WCS [see Fig. 4.6(b)], where $n_1 = 24, n_2 = 11$. The nodes are identified by labeling a node at location (ℓ, j) with a number ℓ_j defined as:

$$\ell_j := n_1 \times j + \ell. \quad (4.20)$$

Therefore, the nodes belonging to the finite element mesh could be represented by the set $\mathcal{N} = \{\ell_j\}, |\mathcal{N}| = N$. The total number of nodes is $N = 288$, which are numbered from 1 to N . Besides, set of all nodes \mathcal{N} could be divide into three sets of nodes as follows

$$\mathcal{N} = \mathcal{B}_1 \cup \mathcal{M} \cup \mathcal{B}_2, \quad (4.21)$$

with

$$\mathcal{B}_1 = \{\ell_0\}, |\mathcal{B}_1| = n_1, \quad \mathcal{B}_2 = \{\ell_{n_2}\}, |\mathcal{B}_2| = n_1 \quad (4.22)$$

$$\mathcal{M} = \{\ell_j\}_{j=1, \dots, n_2-1}, |\mathcal{M}| = n = 240 \quad (4.23)$$

where \mathcal{B}_1 and \mathcal{B}_2 the fixed nodes locate on the two clamped edges and \mathcal{M} the free nodes or markers are tracked by stereo camera [see Fig. 4.6(b)].

Let $\mathbf{X} \in \mathbb{R}^{3N}$ be the full 3-D coordinates vector of all N -nodes, with the sub-vector \mathbf{X}_i is the 3-D position of node i as below

$$\mathbf{X}_i = P(i) = \begin{bmatrix} X_i \\ Y_i \\ Z_i \end{bmatrix} \in \mathbb{R}^3, \forall i \in \mathcal{N} \quad (4.24)$$

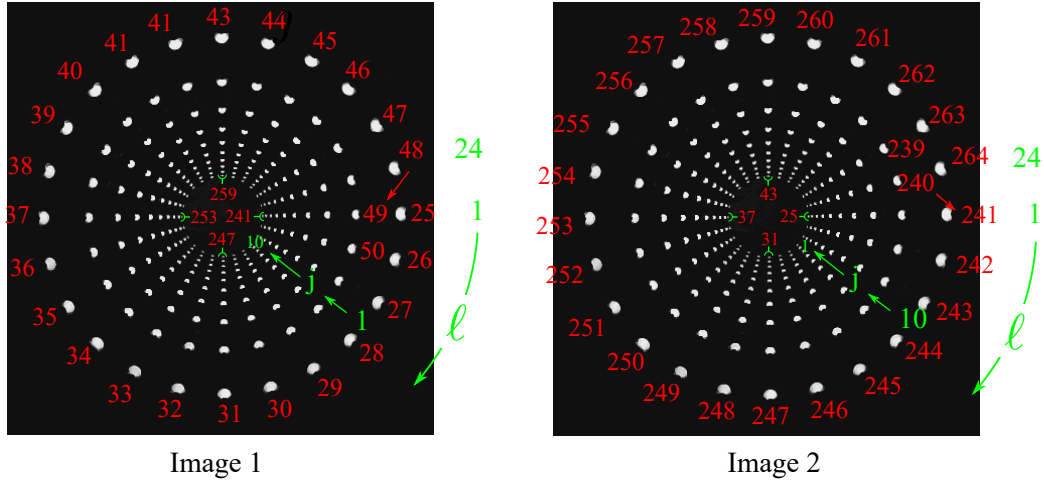


Figure 4.4: Marker numbering on the stereo images (i.e., sets I_1 and I_2).

Additionally, let $I_1 = \{p(i)\}$ and $I_2 = \{q(i)\}$ describe the sets of 2-D projections of all nodes on two images, respectively, [see Fig. 4.4], where $\forall i \in \mathcal{N}, |I_1| = |I_2| = N$. Thus, it needs to develop a stereo registration algorithm to map the observed markers sets Φ_1 and Φ_2 into the organized sets I_1 and I_2 , respectively.

4.5 Non-rigid Stereo Registration

By the method described in the previous section, the 2-D projections Φ_1 and Φ_2 of the markers on stereo images have been obtained. However, such data obtained from image processing are unorganized sets of 2-D points that are insufficient to calculate the 3-D positions of the markers. In order to obtain the displacements [see Eqs. (4.11)–(4.15)], or implementation of stereo reconstruction requires labeling and matching a marker's projections on the stereo images, as defined in Eq. (4.20). This process is known as image registration.

One approach is tracking the position of each marker based on the frame to frame updating [56]. However, if the markers move quickly and the dis-

placements of the marker with the previous position are large, or be affected by noise, this tracking method maybe fails, and could not be an efficient method. Another approach used the coherent point drift (CPD) for non-rigid registration [57], where one point set is the Gaussian Mixture Model (GMM) centroids and the other set is the data points. They iteratively fit the GMM centroids to the data points by maximizing the likelihood and then find the posterior probabilities of centroids, which give the corresponding probability. However, this iterative optimization approach is rather time-consuming with a large point set, resulting in a lack of robustness in real-time performance. To overcome drawbacks of these mentioned stereo registration methods, inspired by guidewire tracking for concentric tubes in fluoroscopic images, as described in [58], an intuitive tracking algorithm for non-rigid point set registration of stereo is developed for this stereo vision system.

Fig. 4.4 shows the distribution of all observed markers in stereo images, in which each 2-D path ℓ contains 10 makers, resulting in a total of 24 paths, as illustrated in Fig. 4.6(a). Notice that in each camera/image, markers appear close to each other when approaching the center point, making it difficult to detect and identify markers at the far distance to the image plane. Therefore, markers should be traced from the boundary area of each image to its center, which corresponds to a reduction in the detection possibility.

By similarity, each path can be described by a set of nodes $\{\vartheta_i\}, \vartheta_i \in \mathbb{R}^2, i = 0, 1, \dots, n_2$, where $\vartheta_0 \in \mathcal{B}_1$ and $\vartheta_{n_2} \in \mathcal{B}_2$ are the fixed nodes that corresponds to the start and end points locating on two end edges, respectively, as illustrated in Fig. 4.5. Assumed that under the condition of deformation, the path is strongly constrained along the control line $\vartheta_0\vartheta_{n_2}$, such that the constructed path line connecting nodes $\{\vartheta_i\}$ should be continuous and smooth. This hypothesis is used to develop the registration algorithm.

Let $\Phi \subset \mathbb{R}^2$ denotes the generalized set of detected markers in a frame of a camera. If ϑ_i is being tracked with former tracking markers $\vartheta_1, \dots, \vartheta_{i-1}$, as shown in Fig. 4.5, then to guarantee the node ϑ_i is the node closest

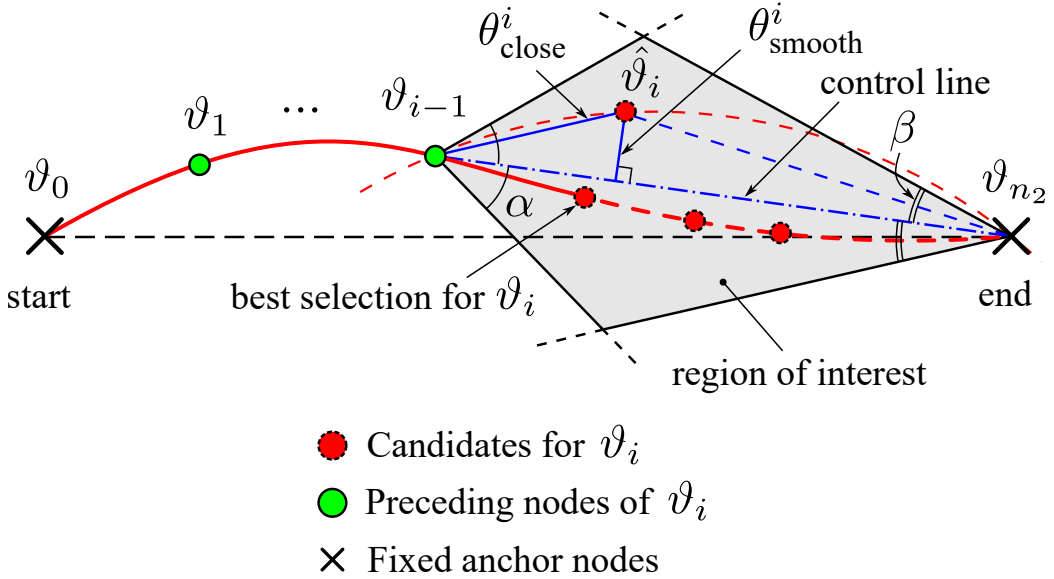


Figure 4.5: The intuitive curve tracking algorithm. Using the proposed objective function with two known anchor points, ϑ_0 and ϑ_{n_2} , the tracking process can trace unknown nodes sequentially $\vartheta_1, \vartheta_2, \dots, \vartheta_{n_2-1}$.

to preceding node ϑ_{i-1} , the closeness term for every candidate $\hat{\vartheta}_i \in \Phi$ is computed as follows

$$\theta_{\text{close}}^i(\hat{\vartheta}_i, \vartheta_{i-1}) = \|\hat{\vartheta}_i - \vartheta_{i-1}\|, \quad (4.25)$$

where $\|\cdot\|$ denotes the standard Euclidean distance.

In contrast, when considering the smoothness of a path, it may be sufficient to characterize the curvature of the arc $\vartheta_{i-1}\hat{\vartheta}_i\vartheta_{n_2}$ at vertex $\hat{\vartheta}_i$ shown in Fig. 4.5 as $\kappa = 1/\mathcal{R} = \frac{2\sin\angle\vartheta_{i-1}\hat{\vartheta}_i\vartheta_{n_2}}{\|\vartheta_{i-1}\vartheta_{n_2}\|}$.

Noticing that the triangle $\triangle\vartheta_{i-1}\hat{\vartheta}_i\vartheta_{n_2}$ with a determined closeness term of distance $\vartheta_{i-1}\hat{\vartheta}_i$, then the curvature at $\hat{\vartheta}_i$ would depend only on the distance of $\hat{\vartheta}_i$ and the control line $\vartheta_{i-1}\vartheta_{n_2}$ (see Fig. 4.5) (i.e., small deformation $\angle\vartheta_{i-1}\hat{\vartheta}_i\vartheta_{n_2} \approx \pi$, then $\sin\angle\vartheta_{i-1}\hat{\vartheta}_i\vartheta_{n_2} \propto d(\hat{\vartheta}_i, \vartheta_{i-1}\vartheta_{n_2})$). Thus, the smooth-

ness term is formulated as:

$$\begin{aligned}\theta_{\text{smooth}}^i(\hat{\vartheta}_i, \vartheta_{i-1}, \vartheta_{n_2}) &= d(\hat{\vartheta}_i, \vartheta_{i-1} \vartheta_{n_2}) \\ &= \frac{\|\hat{\vartheta}_i \vartheta_{i-1} \times \vartheta_{i-1} \vartheta_{n_2}\|}{\|\vartheta_{i-1} \vartheta_{n_2}\|}.\end{aligned}\quad (4.26)$$

As a result, the proposed objective function satisfying both the criteria of closeness and smoothness to search ϑ_i is expressed as:

$$\begin{aligned}\theta_{\text{obj}}^i(\hat{\vartheta}_i, \vartheta_{i-1}, \vartheta_{n_2}) &= (1 - \lambda) \theta_{\text{close}}^i(\hat{\vartheta}_i, \vartheta_{i-1}) \\ &\quad + \lambda \theta_{\text{smooth}}^i(\hat{\vartheta}_i, \vartheta_{i-1}, \vartheta_{n_2}),\end{aligned}\quad (4.27)$$

where $\lambda \in [0, 1]$ is the weight that determines the relative contribution of the two factors.

In addition, obviously, not all markers belonging to Φ are the ideal candidates for tracing the node ϑ_i . For instance, if point $\hat{\vartheta}_i$ possesses the geometric relationship $\angle \hat{\vartheta}_i \vartheta_{i-1} \vartheta_{n_2} > 90^\circ$ or $\angle \hat{\vartheta}_i \vartheta_{n_2} \vartheta_{i-1} > 90^\circ$, it is unlikely to be actual marker node ϑ_i (see Fig. 4.5).

Therefore, to ensure the reliability of the results, we define a limited search area (i.e., region of interest), constrained by two searching angles with respect to the control line $\vartheta_{i-1} \vartheta_{n_2}$ with upper limit angles α and β , as shown in Fig. 4.5. For this purpose, only points within region of interest were considered as candidate nodes. Therefore, for all points $\hat{\vartheta}_i \in \Phi$, the optimal tracking node ϑ_i is the node that minimizes the objective function:

$$\vartheta_i = \arg \min_{\hat{\vartheta}_i \in \Phi} \theta_{\text{obj}}^i(\hat{\vartheta}_i, \vartheta_{i-1}, \vartheta_{n_2}), \quad (4.28)$$

$$\text{subject to: } \angle \hat{\vartheta}_i \vartheta_{i-1} \vartheta_{n_2} < \alpha, \quad \angle \hat{\vartheta}_i \vartheta_{n_2} \vartheta_{i-1} < \beta. \quad (4.29)$$

Note that Eq. (4.29) is also a criterion to determine the breakpoint of the path tracking loop once unavailable candidates within region of interest (see path tracking in Algorithm 1).

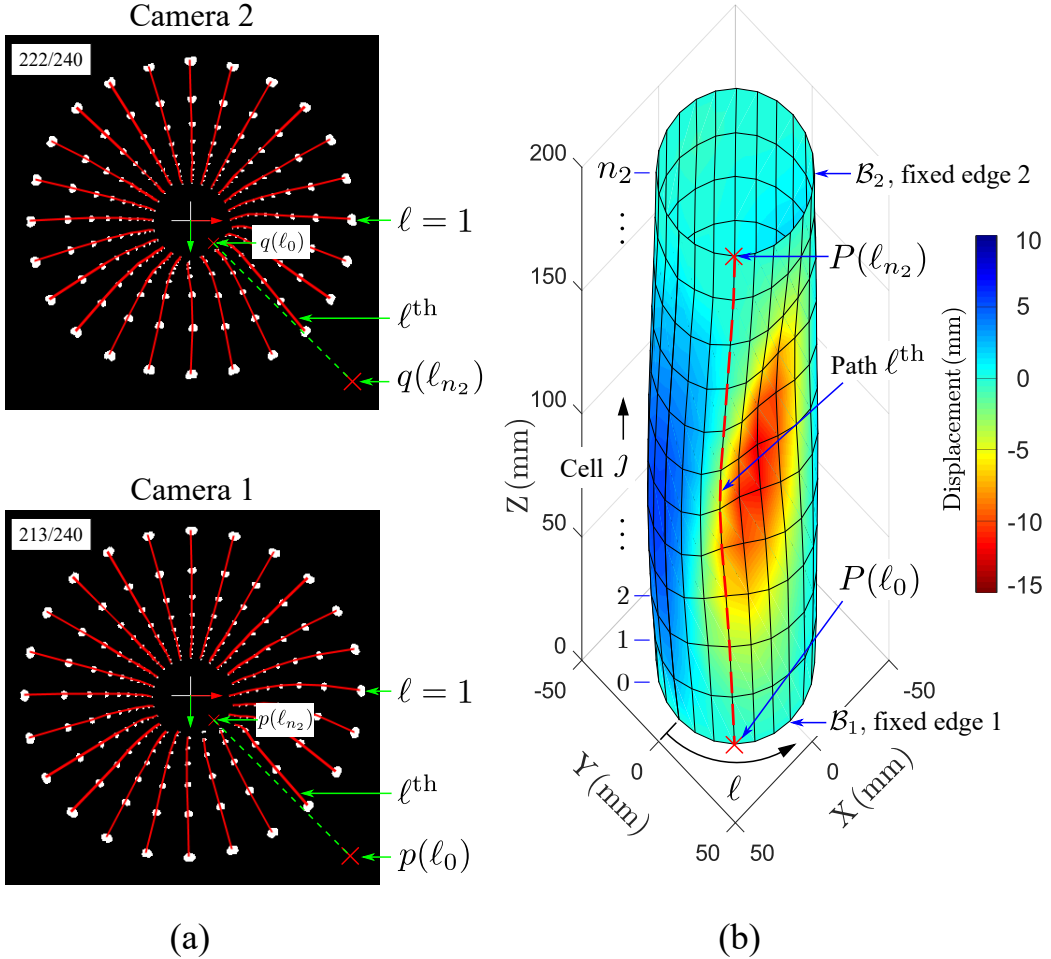


Figure 4.6: A scenario for illustration of the proposed stereo implementation, where the TacLINK is in contact with a long cylinder surface. (a) Stereo images with the proposed path tracking algorithm. (b) 3-D Reconstruction from stereo images of the 3-D shape of the skin.

The stereo registration problem can be stated as seeking the optimal set of nodes for every path on stereo images. Note that these 3-D paths through disparate stereo views are projected opposite on the radial direction of two image planes, as shown Fig. 4.6(a). That is, when we observe from the boundary area to the center of stereo images, the nodes on the first

Algorithm 1 pTRACK($\Phi, \vartheta_0, \vartheta_{n_2}, \alpha, \beta$) \triangleright path tracking function

Require: Given an unorganized set of markers Φ with start point ϑ_0 and end point ϑ_{n_2} of the path, parameters of tracking angles α and β .

```

1: Initialize:  $\vartheta \leftarrow \{\vartheta_0, \emptyset, \dots, \emptyset, \vartheta_{n_2}\}$   $\triangleright |\vartheta| = n_2 + 1$ 
2: for  $i \leftarrow 1$  to  $n_2 - 1$  do
3:    $\vartheta_i \leftarrow$  using Eqs. (4.28)–(4.29)
4:   if  $\vartheta_i = \emptyset$  then break  $\triangleright$  breakpoint
5:   Update:  $\Phi = \Phi / \{\vartheta_i\}$ 
6: end for
7: return Optimal set of nodes on the path  $\{\vartheta_i, i = 0, \dots, n_2\}$ 
end function
```

Algorithm 2 STEREOREGISTRATION(Φ_1, Φ_2) \triangleright registration algorithm

Require: Given the sets of extracted markers Φ_1 and Φ_2 on two images after image processing.

```

1: START Initialize:  $\alpha, \beta$ ,  $\{p(\ell_0), p(\ell_{n_2})\}_{\ell=1 \rightarrow n_1}, \{q(\ell_{n_2}), q(\ell_0)\}_{\ell=1 \rightarrow n_1}$   $\triangleright$  searching angles
    $\triangleright$  use Eqs. (4.7)–(4.8)
2: for  $\ell \leftarrow 1$  to  $n_1$  do
3:    $I_1(\ell_{0:n_2}) \leftarrow$  pTRACK( $\Phi_1, p(\ell_0), p(\ell_{n_2}), \alpha, \beta$ )
4:    $I_2(\ell_{n_2:0}) \leftarrow$  pTRACK( $\Phi_2, q(\ell_{n_2}), q(\ell_0), \alpha, \beta$ )
5: end for
6: return Organized sets  $I_1$  and  $I_2$ 
```

and second images vary as $p(\ell_0) \rightarrow p(\ell_{n_2})$, and $q(\ell_{n_2}) \rightarrow q(\ell_0)$. Note that these curve projections of an arbitrary path ℓ are very constrained by two fixed nodes laid on two boundary edges i.e., $\ell_0 \in \mathcal{B}_1$ and $\ell_{n_2} \in \mathcal{B}_2$, where $\ell = 1, \dots, n_1$ (see Fig. 4.6(b)).

Finally, if Φ_1 and Φ_2 are the sets of detected markers on stereo images resulting from image processing at each camera frame, then the proposed tracking process would start at the boundary area and approach to the center of the image in order to generate the organized sets I_1 and I_2 . This proposed algorithm runs in $\mathcal{O}(n^2)$ time and is presented in Algorithm 2.

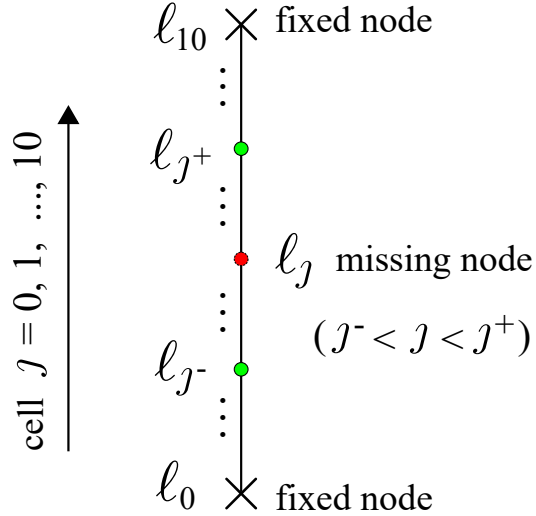


Figure 4.7: Linear interpolation in a path. The coordinates of the missing node ℓ_j is linearly interpolated between the nearest two known nodes ℓ_{j^-} and ℓ_{j^+} on the same path ℓ .

4.6 3-D Reconstruction

This section presents methods used to calculate the 3-D position of all markers based on the 2-D projections provided by the output of the proposed registration algorithm. The limitation of this vision system associates with elongated shapes, for instance, during physical contact, when multiple contacts at high contact depths, uncertainty in the detection of markers may be occurred due to a lack of sight and occlusion, etc. Although there are many circumstances in the detection of entire markers that could be occurred, three scenarios could be realized in the detection of a marker:

First, the 3-D coordinates of markers captured on both cameras' images

can be easily computed using Eqs. (4.11) and (4.15), i.e.,

$$\begin{bmatrix} X \\ Y \\ Z \end{bmatrix} = \begin{bmatrix} R \cos(\varphi) \\ R \sin(\varphi) \\ \frac{f_1 b_2 r_2 - f_2 b_1 r_1}{f_1 r_2 + f_2 r_1} \end{bmatrix} \quad (4.30)$$

where R and φ are determined in Eqs. (4.12) and (4.13), respectively.

Second, for markers not well captured or missed by only one camera, the Z -coordinate can be estimated as the initial value i.e., $Z(\ell_j) \cong j \times h$ (which is acceptable due to the small axial Z -deflection of a cylinder shape with two ends are fixed), and the X - and Y -coordinates can be derived by either camera, as indicated in Eq. (4.3) or Eq. (4.4), i.e., given by the equation:

$$\begin{bmatrix} X \\ Y \end{bmatrix} = \frac{b_1 + Z}{f_1} \begin{bmatrix} x_1 \\ y_1 \end{bmatrix}, \text{ or} \quad (4.31)$$

$$\begin{bmatrix} X \\ Y \end{bmatrix} = \frac{b_2 - Z}{f_2} \begin{bmatrix} x_2 \\ y_2 \end{bmatrix} \quad (4.32)$$

Third, the marker is not detected on both stereo images, resulting in a lack of information. Thus, to determine the coordinates of this marker, linear interpolation is utilized to estimate through its neighbor's node in the same path. Let j^- and j^+ be the nearest determined markers of the missing marker at cell j on path ℓ , where $j^- < j$ and $j^+ > j$, as shown Fig. 4.7. The linear interpolation can be formulated as

$$\mathbf{X}(\ell_j) = w^+ \mathbf{X}(\ell_{j^-}) + w^- \mathbf{X}(\ell_{j^+}), \quad 0 < j < n_2. \quad (4.33)$$

where

$$w^+ = \frac{j^+ - j}{j^+ - j^-}, \quad w^- = \frac{j - j^-}{j^+ - j^-} \quad (4.34)$$

where w^+ and w^- are weight functions.

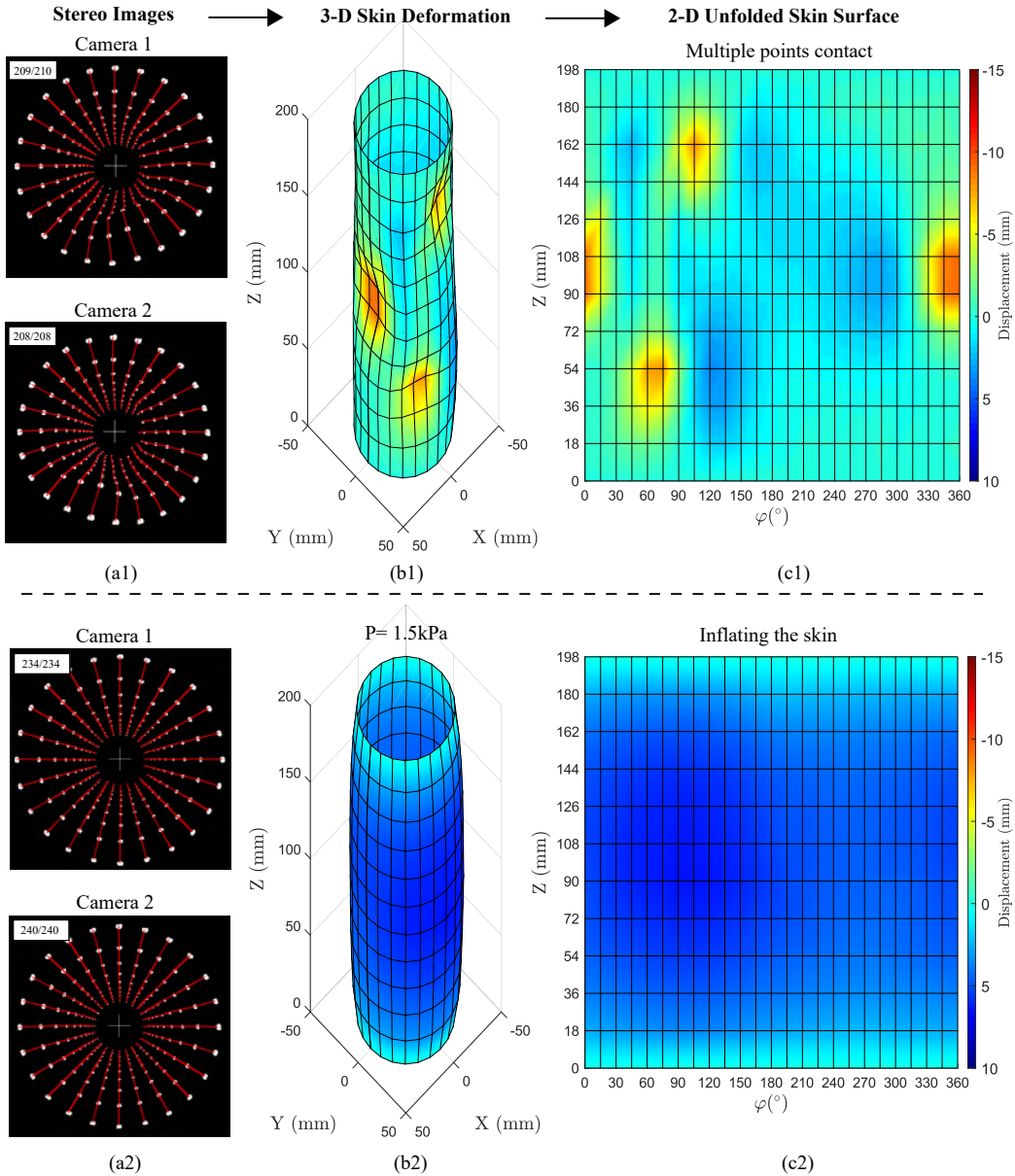


Figure 4.8: Illustration of the robust performance of proposed vision-based sensing for 3-D shape reconstruction of the skin surface. (a1), (b1), and (c1) The skin is subjected to multi-contact points (three points). (a2), (b2), and (c2) The skin is under pressurization of 1.5 kPa.

To implement the proposed tracking algorithm, weight λ in Eq. (4.27) and the searching angles $\{\alpha, \beta\}$ in Eq. (4.29) must be determined. In this system, based on the stability and geometric constraints of 2-D paths on stereo images [see Fig. 4.6(a)], we experimentally choose the tracking parameters α and β equal $2\gamma = 30^\circ$ (see Fig. 4.5), and weight $\lambda = 0.5$.

Using only two co-axial cameras on a simple structure, we proposed robust algorithms to efficiently reconstruct the 3-D surface of the entire skin by tracking markers on the inner wall, even in case of large deformation conditions of large deformation. For example, Fig. 4.8 illustrates the capability of the vision system in the reconstruction of the 3-D skin surface under external contacts, such as multiple points contact [see Fig. 4.8(a1)–(c1)], inflating the skin [see Fig. 4.8(a2)–(c2)]. Besides, the accuracy of the vision system is also verified in Section 4.8.

4.7 Camera Calibration

To perform this vision-based sensing system, the parameters of the stereo camera must be predetermined. Normally, camera calibration can be obtained with a reference planar pattern (e.g., [59]); nonetheless, this method is not suitable for two opposite cameras due to the difficulty and restriction of pattern observation.

In this paper, we utilized the initial geometrical position of markers as known designed positions for determining the parameters of the stereo vision system with self-calibration ability. To do this, let $(R_{0i}, \varphi_{0i}, Z_{0i}), \forall i \in \mathcal{M}$ be a set of 3-D positions of markers at their initial state (non-deformed) and (r_{1i}, φ_{1i}) and (r_{2i}, φ_{2i}) as its observed projections on two cameras.

Estimation of Camera Parameters

Geometrically, due to the 3-D positions of markers are designed symmetrically distributed around the Z -axis, the projections of markers on each image plane

should be symmetric relative to the origin of its coordinates. Therefore, as indicated in [60], the principal points c_1 and c_2 can be simply determined by computing the mean centroids of all markers in pixel coordinates as

$$c_{x_1} = \frac{1}{n} \sum_{i \in \mathcal{M}} u_{1i}, \quad c_{y_1} = \frac{1}{n} \sum_{i \in \mathcal{M}} v_{1i}, \quad (4.35)$$

$$c_{x_2} = \frac{1}{n} \sum_{i \in \mathcal{M}} u_{2i}, \quad c_{y_2} = \frac{1}{n} \sum_{i \in \mathcal{M}} v_{2i} \quad (4.36)$$

where $\forall i \in \mathcal{M}$, $n = 240$ represents the entire set of markers.

For ease of implementation, after retrieving the principal points, a center square of area $S \times S$ pixels² around each principal point is cropped to yield a uniform image size before image processing, here $S = 400$ pixels. The principal points are redefined as $(\frac{S}{2}, \frac{S}{2})$, and the calibration objective is to determine the primary stereo parameters $\mathcal{C} = [f_1, f_2, b_1, b_2]^\top$.

From the projective relationship Eqs. (4.3)–(4.4), the stereo parameters can be determined by solving the least-squares problem as:

$$\min_{\mathcal{C}} \sum_{i \in \mathcal{M}} (\|R_{0i}f_1 - r_{1i}b_1 - r_{1i}Z_{0i}\|^2 + \|R_{0i}f_2 - r_{2i}b_2 + r_{2i}Z_{0i}\|^2). \quad (4.37)$$

$$\text{s.t. } \mathcal{C} = \arg \min_{\mathcal{C}} \|\mathbf{AC} - \mathbf{b}\|^2 = (\mathbf{A}^\top \mathbf{A})^{-1} \mathbf{A}^\top \mathbf{b} \quad (4.38)$$

$$\text{with } \mathbf{A} = \begin{bmatrix} \mathbf{A}_1 \\ \mathbf{A}_2 \\ \vdots \\ \mathbf{A}_n \end{bmatrix}, \quad \mathbf{b} = \begin{bmatrix} \mathbf{b}_1 \\ \mathbf{b}_2 \\ \vdots \\ \mathbf{b}_n \end{bmatrix}, \quad \text{where} \quad (4.39)$$

$$\mathbf{A}_i = \begin{bmatrix} R_{0i} & -r_{1i} & 0 & 0 \\ 0 & 0 & R_{0i} & -r_{2i} \end{bmatrix}, \quad \mathbf{b}_i = \begin{bmatrix} r_{1i}Z_{0i} \\ r_{2i}Z_{0i} \end{bmatrix} \quad (4.40)$$

Note that Eq. (4.37) requires at least two reference points/markers to derive four unknown parameters \mathcal{C} . This linear minimization can be simply solved with MATLAB's built-in mldivide function as $\mathcal{C} = \text{mldivide}(\mathbf{A}, \mathbf{b})$.

Table 4.1: Self-Calibration Results of Stereo Camera Parameters ($\mu \pm \sigma$)

Parameters	Camera 1	Camera 2	Units
f_i	226.91 ± 0.09	226.54 ± 0.06	pixels
b_i	26.50 ± 0.04	226.49 ± 0.02	mm
c_{x_i}	322.76 ± 0.01	299.70 ± 0.00	pixels
c_{y_i}	225.23 ± 0.01	251.89 ± 0.01	pixels
k_{1i}	27.85 ± 0.09	21.08 ± 0.10	$\times 10^{-7}$
k_{2i}	-14.09 ± 0.04	-11.58 ± 0.05	$\times 10^{-11}$

Subscript i corresponds to the camera index, ($i = 1, 2$).

Correction of Lens Distortion

When using wide-angle lenses, it is necessary to consider the lens distortion of the camera. In this camera configuration, we only assessed the term for radial distortion. If \check{r}_1 and \check{r}_2 are the actual observed coordinates, and r_1 and r_2 are the ideal radial image coordinates according to the pinhole model described in Eq. (4.7), then the radial division distortion model [61] can be written as

$$r_1 = \frac{\check{r}_1}{1 + k_{11}\check{r}_1^2 + k_{21}\check{r}_1^4}, \quad (4.41)$$

$$r_2 = \frac{\check{r}_2}{1 + k_{12}\check{r}_2^2 + k_{22}\check{r}_2^4}, \quad (4.42)$$

where k_{11}, k_{21} and k_{12}, k_{22} are the coefficients of the radial distortion of the two camera lenses, respectively.

To determine the distorted coefficients, the preliminary parameters \mathcal{C} in Eq. (4.37) were estimated by ignoring distortion. Then, the ideal image coordinates r_1 and r_2 are determined using the equations in Eqs. (4.7)–(4.8). Thus, from Eqs. (4.41)–(4.42), the coefficients $\mathcal{L} = [k_{11}, k_{21}, k_{12}, k_{22}]^\top$ can be

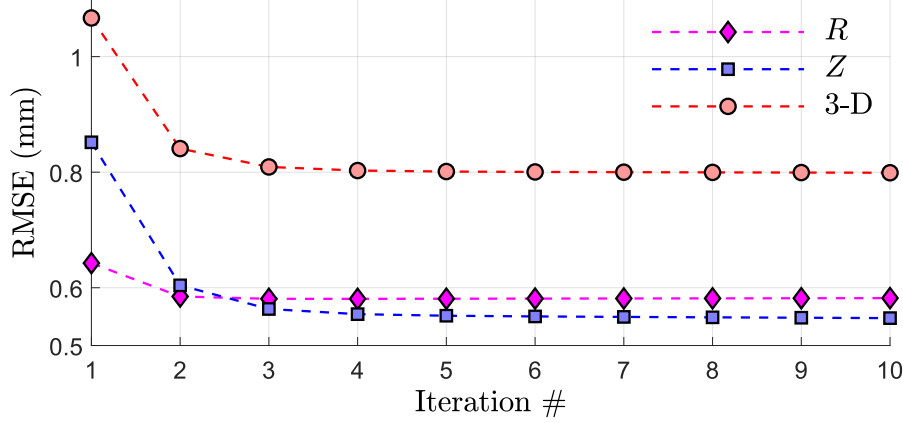


Figure 4.9: Calibration results for each iteration: RMSE of coordinates for estimating stereo parameters and lens distortion.

estimated by minimizing the cost function as

$$\begin{aligned}
 \min_{\mathcal{L}} \quad & \sum_{i \in \mathcal{M}} (\|r_{1i}\check{r}_{1i}^2 k_{11} + r_{1i}\check{r}_{1i}^4 k_{21} + (r_{1i} - \check{r}_{1i})\|^2 \\
 & + \|r_{2i}\check{r}_{2i}^2 k_{12} + r_{2i}\check{r}_{2i}^4 k_{22} + (r_{2i} - \check{r}_{2i})\|^2) \\
 \text{s.t.} \quad & \mathcal{L} = \arg \min_{\mathcal{L}} \|\mathbf{A}\mathcal{L} - \mathbf{b}\|^2 = (\mathbf{A}^\top \mathbf{A})^{-1} \mathbf{A}^\top \mathbf{b} \\
 \text{with} \quad & \mathbf{A} = \begin{bmatrix} \mathbf{A}_1 \\ \mathbf{A}_2 \\ \vdots \\ \mathbf{A}_n \end{bmatrix}, \quad \mathbf{b} = \begin{bmatrix} \mathbf{b}_1 \\ \mathbf{b}_2 \\ \vdots \\ \mathbf{b}_n \end{bmatrix}, \quad \text{where} \\
 & \mathbf{A}_i = \begin{bmatrix} r_{1i}\check{r}_{1i}^2 & r_{1i}\check{r}_{1i}^4 & 0 & 0 \\ 0 & 0 & r_{2i}\check{r}_{2i}^2 & r_{2i}\check{r}_{2i}^4 \end{bmatrix}, \mathbf{b}_i = \begin{bmatrix} \check{r}_{1i} - r_{1i} \\ \check{r}_{2i} - r_{2i} \end{bmatrix}
 \end{aligned} \tag{4.43}$$

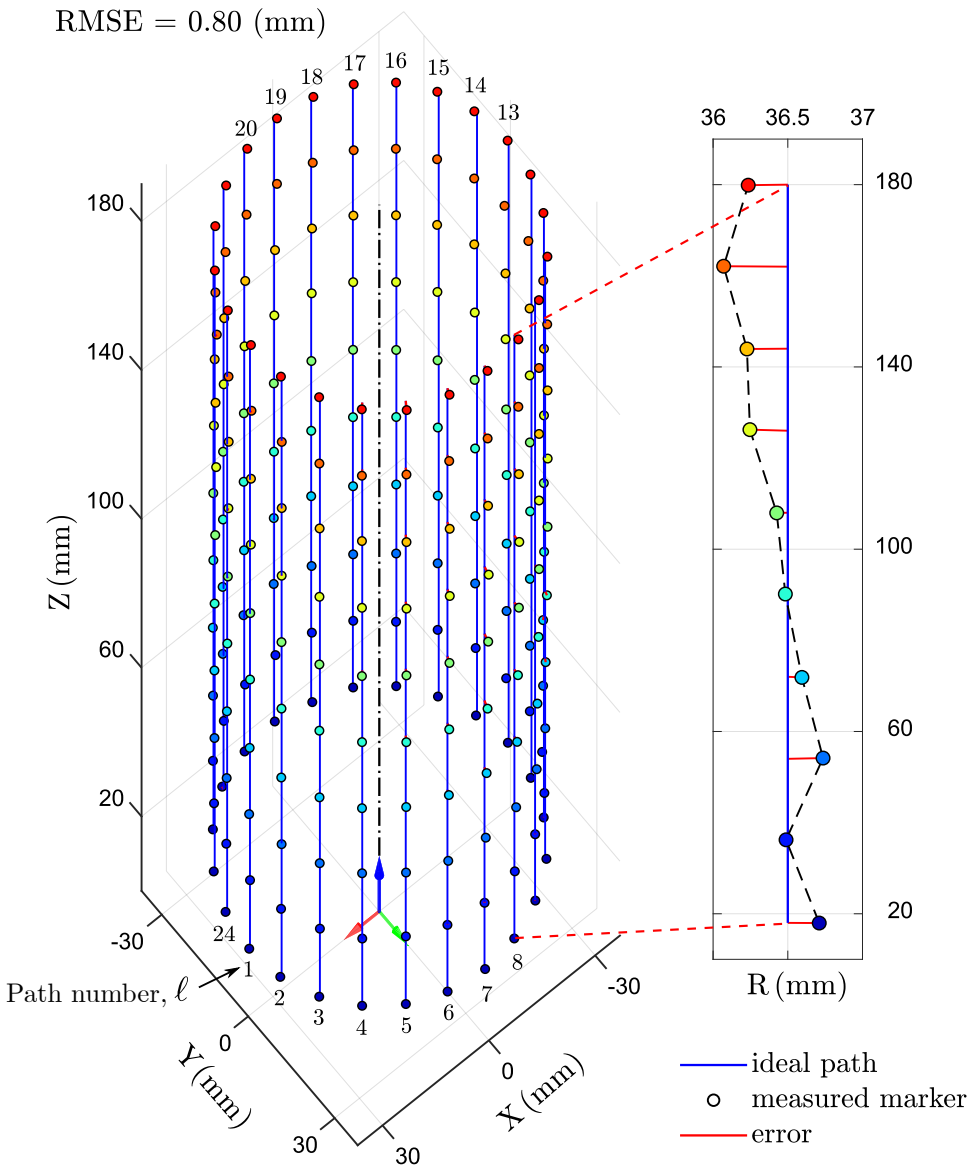


Figure 4.10: Illustration of the initial 3-D position of markers (roundly marked) using the calibrated parameters.

Once \mathcal{L} is obtained, the parameters \mathcal{C} can be recomputed by recalling Eq. (4.37) with the ideal radial coordinates are corrected by using the distortion model Eqs. (4.41)–(4.41) with this procedure repeated until reaching convergence. The root-mean-square error (RMSE) of coordinates is used to assess the calibration process, as shown in Fig. 4.9. This figure shows quick convergence of calibrated coordinates RMSE (R -, Z -axes, and 3-D) within fewer than four iterations and a significant reduction in RMSE results.

The calibration process was performed a total of 20 times, resulting in the parameters of camera and distortion coefficients shown in Table 4.1. These results could be used to verify the parameters of the vision system. For example, if two cameras are similar, the length of artificial skin after calibration can be calculated as $L = b_2 - b_1 \approx 200.0$ mm (see Fig. 4.1), while the designed value is 198.0 mm (see Fig. 3.2), i.e., the absolute error is 2.0 mm, or percent error $\delta = \frac{2.0}{198.0} = 1.01\%$.

With calibrated parameters, the 3-D position of markers in WCS is determined. Fig. 4.10 illustrates measured locations of markers comparing with their initial geometric 3-D paths. The average RMSE of the calibrated R -, Z -coordinates and 3-D were 0.58 mm, 0.55 mm and 0.80 mm, respectively.

By referring to the pattern of markers, we easily determined the intrinsic and extrinsic parameters of the stereo camera and lens distortion. In this application, this technique can be used for the automatic processing of the calibration procedure.

Note that the light traveling the acrylic tube would be refracted/bent as it passes from one transparent substance into another medium. Here, because the inner and outer surfaces of the transparent acrylic tube are parallel, as shown in Fig. 4.11, the incident ray and emergent ray toward the centerline are shifted. Besides, before hitting the vision sensor, the light refraction also occurred in the lens (glass material). However, the system's calibration used refracted images, resulting in the parameters of lens distortion covered this effect (multi-refraction).

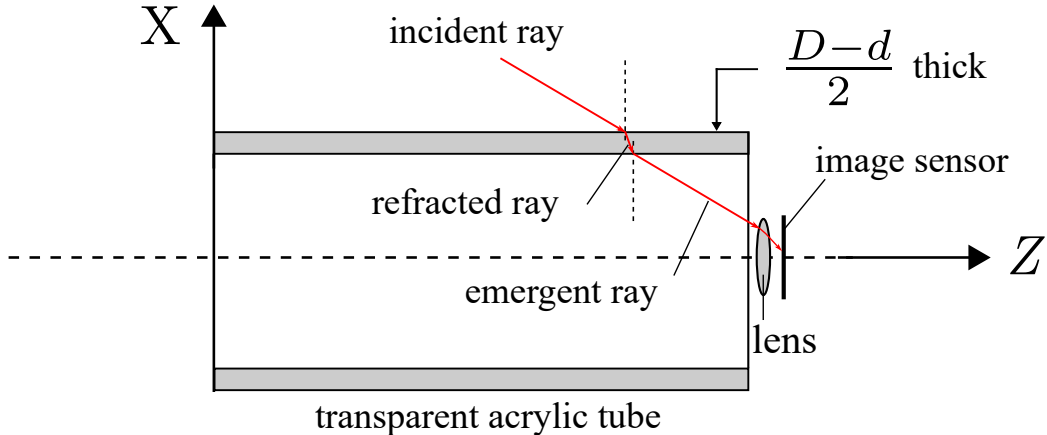


Figure 4.11: A ray of light being refracted in the transparent acrylic tube.

4.8 Experimental Accuracy

4.8.1 Setup

The experimental platform is installed to calibrate and evaluate the operation of the TacLINK, as shown in Fig. 4.12(a). TacLINK is fixed in a rigid vertical position on the platform. To create precise displacement of external contact with the skin of the TacLINK, we used a 6-DOF robotic arm (VP6242A, Denso Robotics, Japan) that can precisely displace with high repeatability of 0.02 mm. A probe is attached to the center of the robot's end-effector.

The robot was controlled to move the probe in-plane OYZ and push horizontally against the skin at different positions on the seventh path ($\ell = 7$). We used a cylindrical probe as a standard screw M3 with a larger diameter of $D_{\text{probe}} = 5.5$ mm to push accurately the entire cross-sectional area of the marker $D_{\text{marker}} = 2.8$ mm, i.e., $D_{\text{probe}} > D_{\text{marker}}$. Here, all data were acquired and processed on MATLAB 2019b.

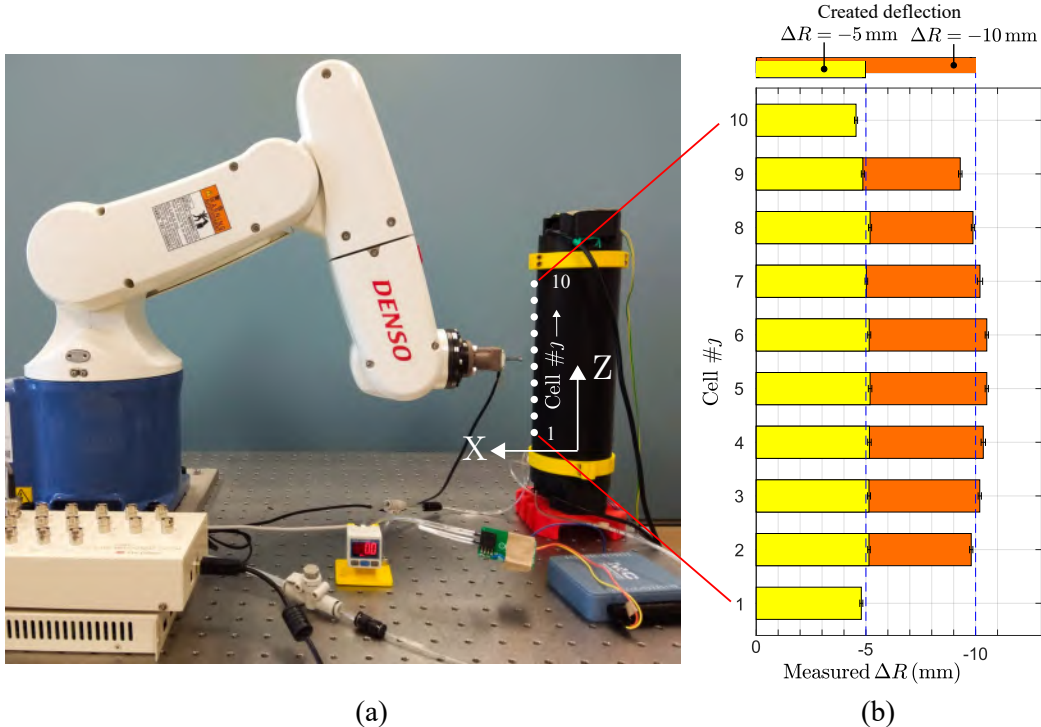


Figure 4.12: Experiment evaluating the measurement accuracy of the vision system in the radial direction. (a) Experimental setup. (b) Measured displacements of ten nodes on a path comparing with deflections created by robot motion.

4.8.2 Experimental Result

The performance of stereo-based 3-D reconstruction was verified by evaluating the measurement error of radial displacement (in working range) of ten free nodes/markers on a path. With cylinder shape, radial deflection of the skin plays the most important role, i.e., the displacements on other directions are trivial comparing with radial displacement (see Section 6.2) that is, therefore, easier to detect by the vision system. On the other hand, it is challenging to determine the true value of axial (Z-) direction. In this experiment, the robot arm was controlled, allowing the probe to displace the designed radial displacements ΔR of -5 and -10 mm every ten nodes

(markers) on the seventh path, as shown in Fig. 4.12(a).

In this test, ten experimental trials were performed at an inner air pressure of zero value $P = 0 \text{ Pa}$. Fig. 4.12(b) shows the measured radial deflections of every ten node $j = 1, \dots, 10$ compared with baseline robot motion ΔR . Note that because of geometric constraints on the skin, two nodes located near two ends $j = 1, 10$ could only be displaced by -5 mm .

The results of this testing showed that the absolute errors were below 0.7 mm , corresponding to a full scale error $= \frac{0.7}{\text{FS}} \sim 5\% \text{ FS}$ (designed full-scale $\text{FS} = 15 \text{ mm}$). Note that this error might also derive from several factors of the system, such as poor skin fabrication and installation tolerances with soft materials. These experimental results indicate that the proposed stereo system (including proposed algorithms) is both efficient and accurate in estimating 3-D deformation of the skin.

4.9 Summary

In this chapter, we introduced the vision system of TacLINK, built from two cameras. The mathematical model and analysis of the effect of vision parameters on the characteristics of 3-D measurement were provided with the self-calibration technique was also introduced for the development of the automatic calibration procedure. The robust techniques for stereo implementation of image processing, stereo registration, and 3-D reconstruction were developed. These techniques could be customized for similar systems.

As a result, the proposed vision system works efficiently providing the 3-D shape in real-time by tracking the position of markers, even in multiple points contact and under pressurization. The experiment was also carried to evaluate the error of the vision system (about $\sim 5\% \text{ FS}$). Finally, we introduced a novel vision sensing system that is high performance in 3-D reconstruction for a curved and elongated surface of TacLINK but very low in cost (about US100\$), and easy to manufacture, calibrate, and implement.

Chapter 5

Finite Element Modeling

5.1 Introduction

In the development of an advanced engineering system, engineers have to go through the design process steps of modeling, simulation, analysis, designing, prototyping, testing, and evaluation. As such, techniques related to modeling and simulation are effective ways to save cost and reduce time in building a new engineering product. The application of the finite element method (FEM) has therefore developed rapidly and widely utilized over the last few decades for solving mathematical problems of engineering from various fields, such as structural mechanics (e.g., stress, vibration), fluid flow, heat transfer, piezoelectric, and electromagnetics.

The finite element method (FEM) is a numerical technique to solve partial differential equations (PDEs). In general, for the vast majority of physical problems and object geometries, the PDEs cannot be modeled and solved with analytical methods. Instead, the FEM derives a large system into smaller parts that are called finite elements, which is achieved by the construction of a mesh of the object. The numerical domain for the FE solution has therefore a finite number of nodes. The simple approximations that model these finite element equations are then assembled into a global system

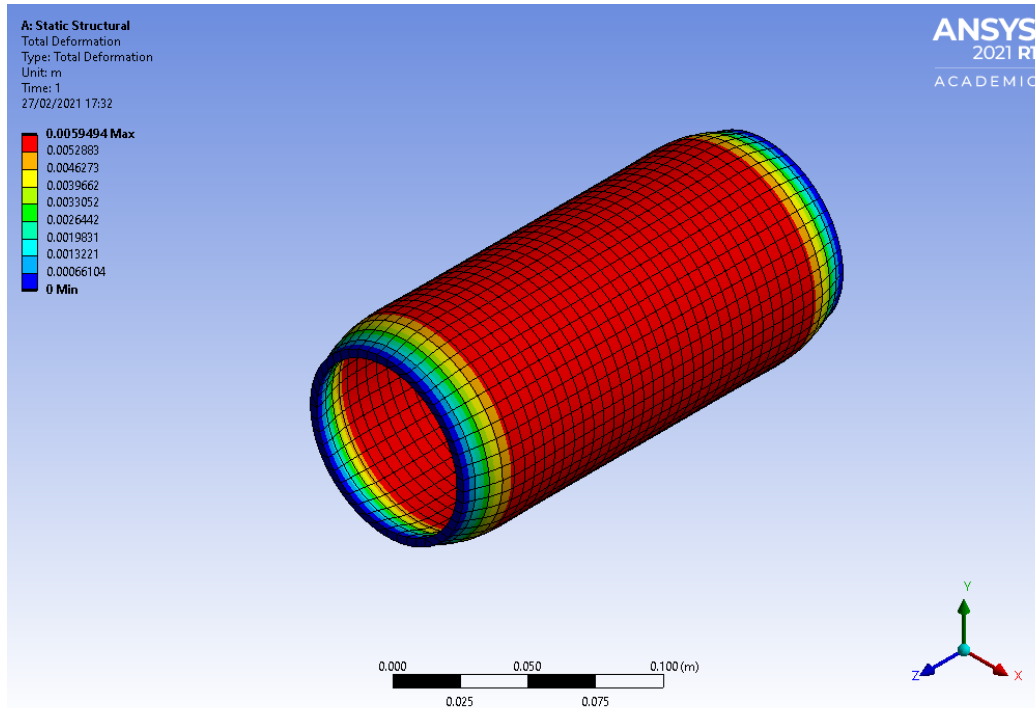


Figure 5.1: FE simulation for the skin using ANSYS student software. The skin is subjected to an inner pressure of 1.5 kPa.

of equations that models the entire system. The finite element method problem with boundary conditions finally results in a simple system of algebraic equations that can be easily solved with basic analytical methods.

For this purpose, many commercial software applications for finite element analysis are developed, such as ABAQUS, ANSYS, and COMSOL. These software packages provide a powerful tool for engineers to simulate, evaluate performance and optimize designs. For instance, the inflation response of the skin could be intuitively simulated on the educational ANSYS software (ANSYS Inc., USA) shown Fig. 5.1. Nonetheless, the commercial software only provides the preprocessing, solution, and postprocessing abilities, the core system of the FE model describing the relationship between the inputs (forces) and outputs (displacements, stresses, strains) is not re-

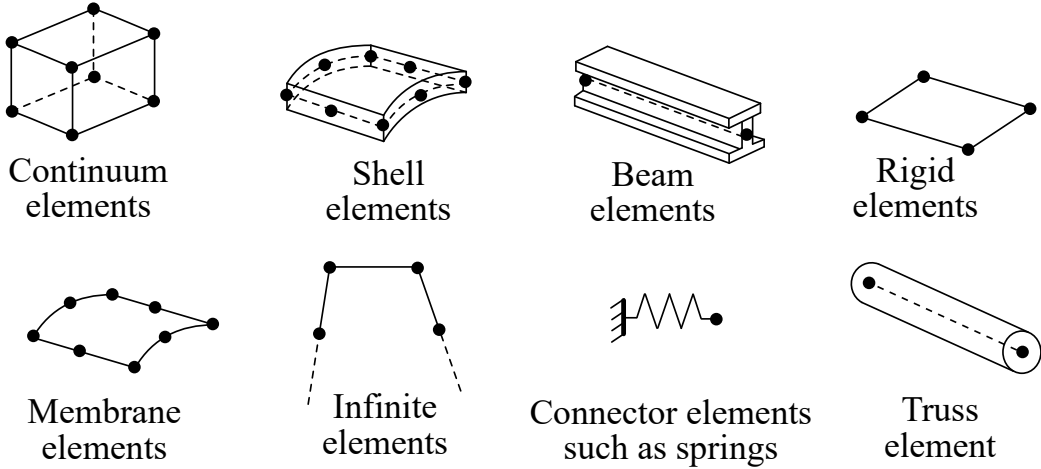


Figure 5.2: Common element families [62].

vealed. Thus, this chapter is to formulate the finite element (FE) model of the skin, establishing the skin stiffness describing the relationship between nodal forces and measured displacements provided by the vision system. The distribution of tactile force on the skin body of TacLINK could be treated as the concentrated force of the force vector.

5.2 Fundamentals

Figure 5.2 shows the element families that are commonly used in finite element analysis, i.e., trusses, beams, plates, shells, solids. The major distinction between these element families is the geometry type that each family assumes. Their elements could be divided into 3 categories: 1-D, 2-D, and 3-D spaces, as shown in Fig. 5.3.

The element geometry can be distinguished based on the number of nodes, and the degrees of freedom. The degrees of freedom define the variables being considered during analysis and originally control the element behavior. For instance, truss elements possess only translational degrees of freedom, whereas beam elements have both translational and rotational degrees of

Dimension	Degree	Element Shape	Element Type
1-D (Line)	Linear		Beam, Truss
	Quadratic		Beam
2-D (Area)	Linear		Plane stress, Plane strain, Plate, Shell
	Quadratic		
3-D (Volume)	Linear		Solid
	Quadratic		

Figure 5.3: Element categories [63].

freedom. The number of nodes of an element impacts directly the total degrees of freedom and has therefore a significant effect on the deformation ability of the element. Additionally, the number of nodes an element also implies the interpolation strategy used to compute the displacement vector of a point within the element domain. There are two orders of interpolation that are commonly used, i.e., linear and quadratic (see Fig. 5.3)

- Linear (first-order): Elements that have nodes only at their corners.
- Quadratic (second-order): Elements that have corner nodes and mid-side nodes.

The following five steps summarize the main steps of the finite element procedure as

1. First step (preprocessing):
 - Create geometry.
 - Define material properties.
 - Create mesh of the geometry.
 - Define initial and boundary conditions.
2. Second step (element formulation): development of equations for elements.
3. Third step (assembly): set up global problem, obtaining equations for the entire system from the equations for one element
4. Fourth step (solution): solve system of linear equations.
5. Fifth step (postprocessing): determining quantities of interest, such as stresses and strains and obtaining visualizations of the response.

It is also important to introduce the criteria to select the element type for a structure. For solid structures, automatic tetrahedral meshing can be selected. However, the complexity significantly reduces when considering other structures, such as beams, plates, and shells. This is illustrated in Fig. 5.4 when the structures are of the form of beams, plates, or shells, they can be classed as thin structures, in which if the thickness and breadth of the structure are much larger than its length, and it can be considered as a beam [see Fig. 5.4(a)]. If the thickness is much smaller than both the length and breadth, then the structure can be considered as a plate or shell [see Fig. 5.4(b),(c)]. Otherwise, if all the dimensions are comparable, then the structure can be considered to be a full solid element [see Fig. 5.4(d)].

Shell elements can be used to model structures if their thickness is remarkably smaller than the others dimension. Conventionally flat shell elements use this criterion to discretize a 3-D body by reducing the 3-D geometry approach to a 2-D domain in terms of nodal variables at the neutral surface

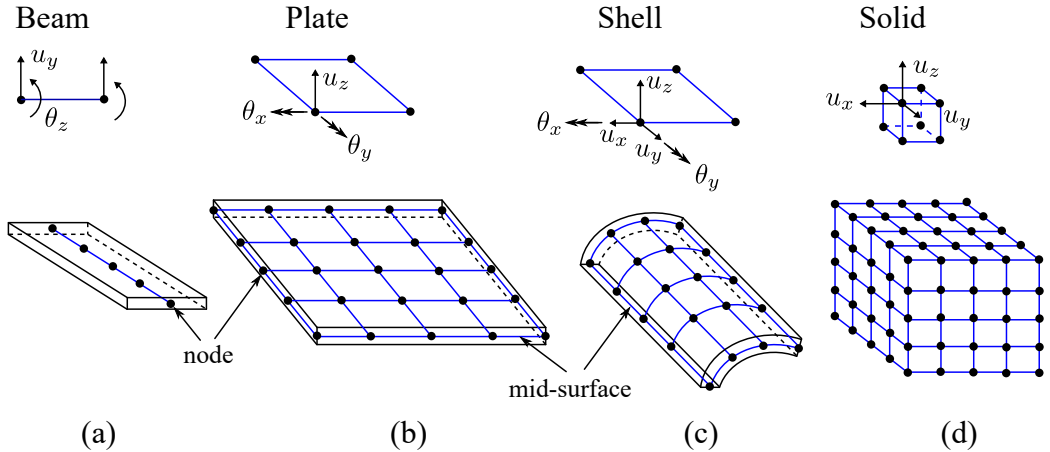


Figure 5.4: Finite element discretization.

Structural body \longrightarrow Finite element model \longrightarrow Element

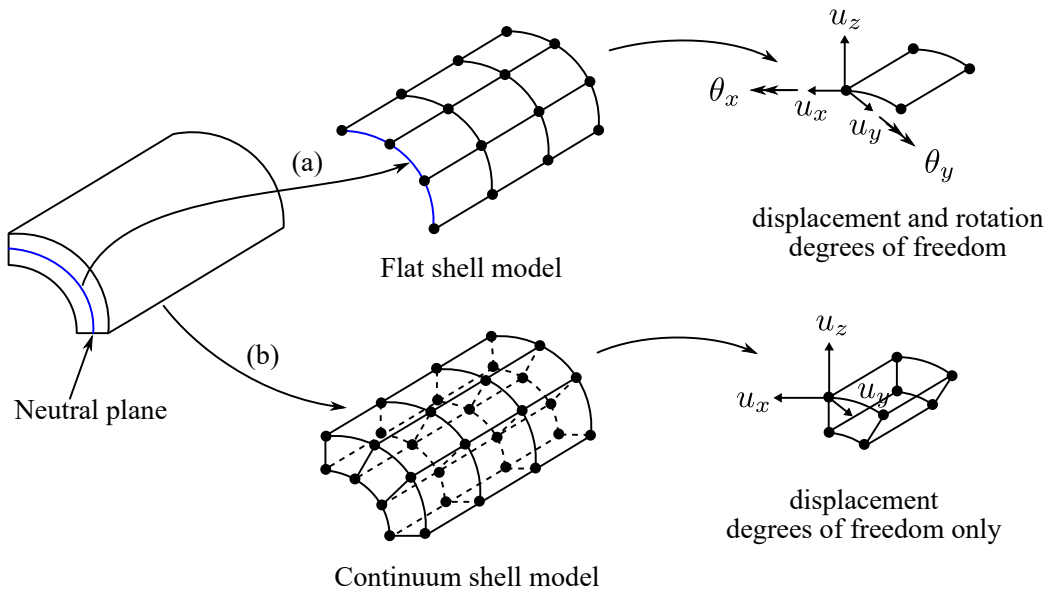


Figure 5.5: Discretization of solid and flat shell elements [64].

(mid-surface) [69], as shown in Fig. 5.5. In this case, the thickness is described via the definition of section property. Flat shell elements have both displacement u_x, u_y, u_z and rotational θ_x, θ_y degrees of freedom. The signifi-

cant advantage of this method is that the element is applicable over a wide range of thicknesses and curvatures. On the contrary, continuum shell elements discretize a whole 3-D body [64]. The thickness is described from the element nodal geometry, as well as, continuum shell elements that have only displacement u_x, u_y, u_z degrees of freedom. From a finite element method point of view, continuum shell elements is similar to 3-D continuum solids [see Fig. 5.4(d)], but their kinematic and constitutive behavior looks like flat shell elements.

5.3 FE Mesh and Element Geometry

In this study, the skin was assumed to be linearly elastic, the shell element was selected to discretize the skin body because the thickness is significantly smaller than the other dimensions i.e., $t \ll ID$ and $t \ll L$. To do this, conventional flat shell elements combining membrane and bending behaviors are formulated based on the Reissner-Mindlin theory, as indicated in [65]. Note that the thickness of the flat shell is assumed to be in the direction normal to the mid-surface. Besides, in this system, only the static model of the skin is considered, the gravitational effect on the skin is ignored, the effect of gravity on the skin is hypothesized to be much smaller than the effects of the range of measured tactile forces.

To approximate the elemental fields within each element, the shape functions can be of a different order, for example, linear (first-order), quadratic (second-order), and cubic (third-order) shape functions. Note that using high-order interpolation of quadratic or cubic shapes, which requires additional mid-nodes (1 or 2, respectively) by increasing the spatial resolution of markers/nodes, can give a better representation of the geometry. However, increasing the density of the marker results in reducing the detectability of the vision system. Here is a trade-off between the detectability of the vision system and the accuracy of the finite element model. Thus, to ensure

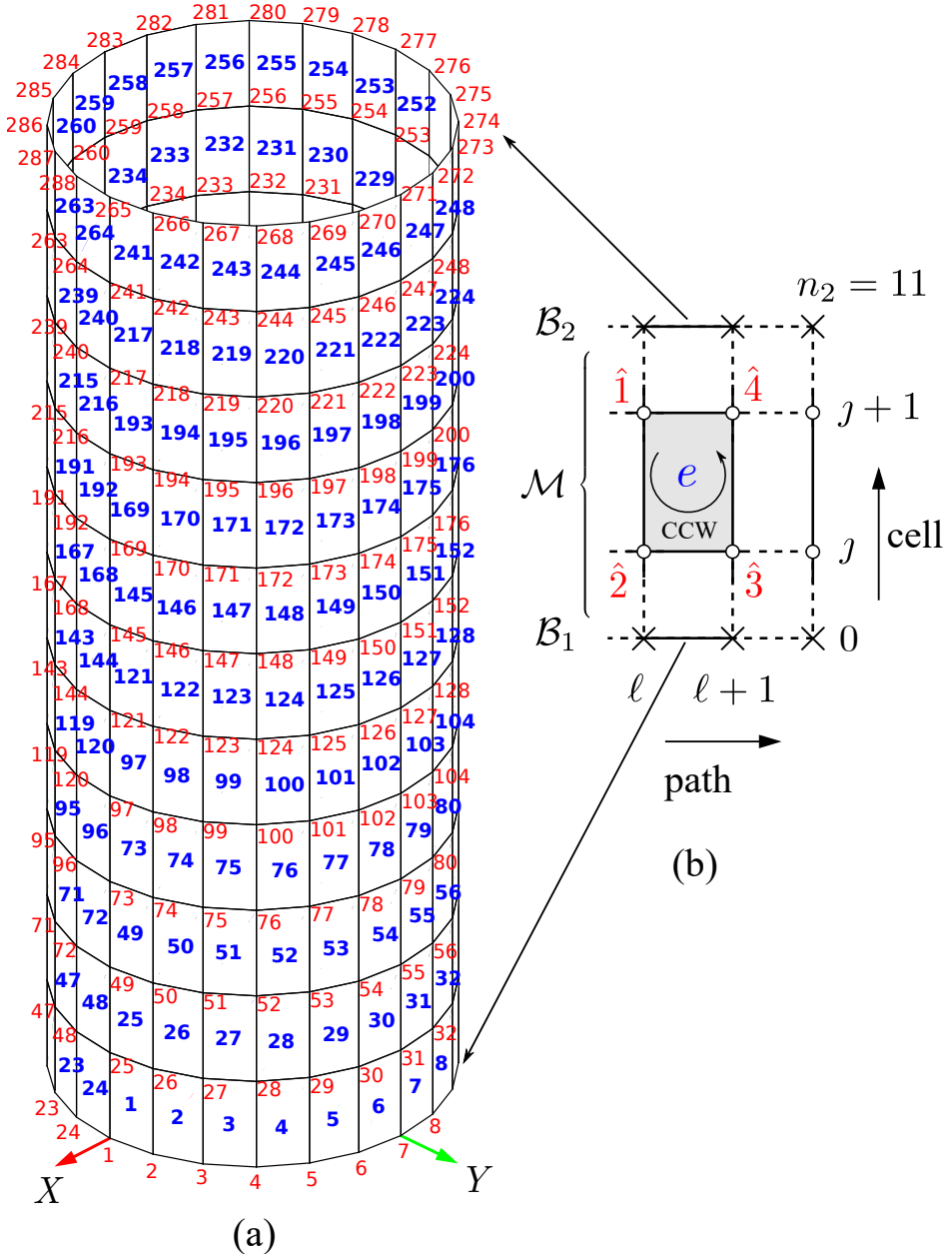


Figure 5.6: FEM discretization of a cylindrical skin surface in flat rectangular shell elements. (a) Finite element mesh of $N_e = 264$ elements and $N = 288$ nodes. (b) Mesh topology.

the stability of the entire system, the rectangular shell element with linear interpolation (four nodes) was selected to discretize the skin surface.

5.3.1 Meshing

Owing to its 3-D axis-symmetric shape, the skin body can be equally discretized into a mesh of $N_e = 264$ elements, as shown in Fig. 5.6(a). The rectangular domain of a flat shell element is approximated as $2a = h$ and $2b = 2R_0 \sin(\gamma/2)$ (see Fig. 5.7). On the other hand, to build the elemental and global vectors and matrices, it is necessary to define mesh topology providing a crucial nodal connectivity of elements. By positioning an element $e \in \{1, 2, \dots, N_e\}$ by the node associated with the left bottom corner shown in Fig. 5.6(b). Thus, the element at node (ℓ, j) is numbered $e = \ell_j$ defined in Eq. (4.20) and formed by four nodes distributed counterclockwise (CCW), i.e.,

$$\begin{aligned} & \hat{1}(\ell, j+1) \\ & \hat{2}(\ell, j) \\ & \hat{3}(\ell+1, j) \\ & \hat{4}(\ell+1, j+1) \end{aligned} \tag{5.1}$$

where $\ell = 1, \dots, n_1 - 1$. However, because of the circular cylinder surface, if $\ell = n_1$, nodes 3 and 4 change to $\hat{3}(1, j)$ and $\hat{4}(1, j+1)$, respectively.

5.3.2 Element Geometry

In general, the complexity of the finite element modelling requires the usage of several coordinate systems to describe the element geometry, such as displacement field, stress, and strain field. In this paper, beside the global coordinates $\{X, Y, Z\}$, the four-node shell element is formulated in the local coordinates $\{\hat{x}, \hat{y}, \hat{z}\}$ and natural coordinates $\{\xi, \eta\}$, where the \hat{z} -axis is perpendicular to the mid-surface, as shown in Fig. 5.7. In this system, the \hat{x} -axis is defined as the opposite of the Z -axis, and the edge 2-3 defines the

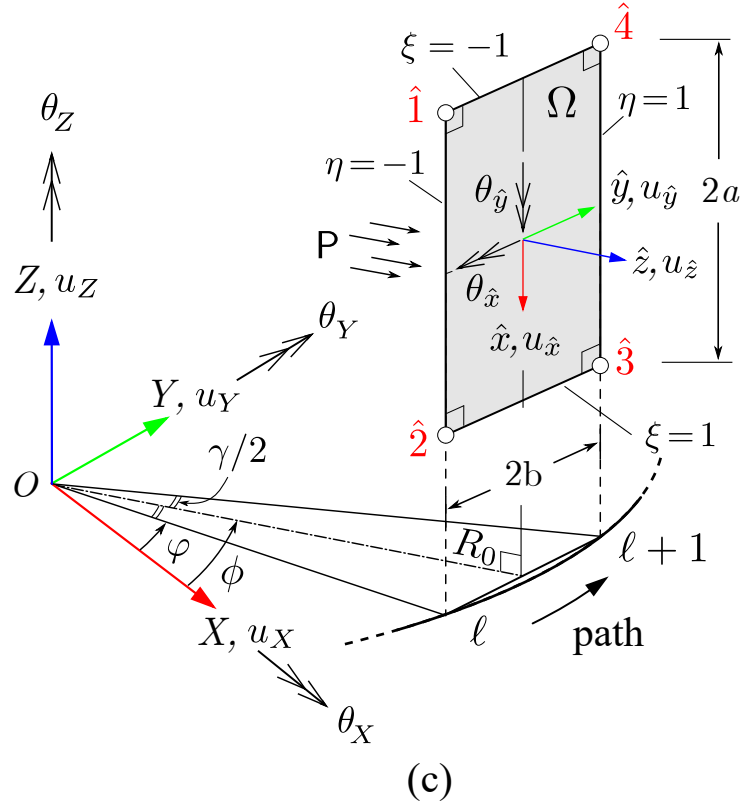


Figure 5.7: Element geometry and coordinate systems.

\hat{y} -direction, thus the \hat{z} -axis could be obtained by the cross product of \hat{x} - and \hat{y} -axes (see Fig. 5.7). Note that each thin shell element node has 5 degrees of freedom i.e., in-plane displacements $u_{\hat{x}}, u_{\hat{y}}$ and lateral displacement u_z , and rotations $\theta_{\hat{x}}$ and $\theta_{\hat{y}}$ of \hat{z} -axis in the planes $\hat{x}\hat{z}$ and $\hat{y}\hat{z}$, respectively. The nodal vectors of elemental displacements $\hat{\mathbf{d}} \in \mathbb{R}^{20}$ and forces $\hat{\mathbf{f}} \in \mathbb{R}^{20}$ are given by

$$\hat{\mathbf{d}}_i = \begin{bmatrix} u_{\hat{x}_i} \\ u_{\hat{y}_i} \\ u_{\hat{z}_i} \\ \theta_{\hat{x}_i} \\ \theta_{\hat{y}_i} \end{bmatrix}, \quad \hat{\mathbf{f}}_i = \begin{bmatrix} f_{\hat{x}_i} \\ f_{\hat{y}_i} \\ f_{\hat{z}_i} \\ m_{\hat{x}_i} \\ m_{\hat{y}_i} \end{bmatrix}, \quad \text{with } i = 1, 2, 3, 4. \quad (5.2)$$

where \hat{x}_i , \hat{y}_i and \hat{z}_i denote local coordinates at node $i = 1\text{--}4$ of the element.

5.4 Element Displacement Field

We consider the cylinder skin surface discretized into C(0) isoperimetric flat shell element shown in Fig. 5.6. Each element is presented in the local plane $\hat{x}\hat{y}$, as shown in Fig. 5.7. The displacement field of a point within element domain Ω is interpolated as

$$\hat{\mathbf{u}} = \begin{bmatrix} u_{\hat{x}} \\ u_{\hat{y}} \\ u_{\hat{z}} \\ \theta_{\hat{x}} \\ \theta_{\hat{y}} \end{bmatrix} = \sum_{i=1}^4 \mathbf{N}_i \hat{\mathbf{d}}_i \triangleq \mathbf{N} \hat{\mathbf{d}}, \quad (5.3)$$

with the shape matrix

$$\mathbf{N}_i = \begin{bmatrix} N_i & 0 & 0 & 0 \\ 0 & N_i & 0 & 0 \\ 0 & 0 & N_i & 0 \\ 0 & 0 & 0 & N_i \end{bmatrix}, \text{ and } \mathbf{N} = \begin{bmatrix} \mathbf{N}_1 & \mathbf{N}_2 & \mathbf{N}_3 & \mathbf{N}_4 \end{bmatrix} \quad (5.4)$$

where $N_i(i = 1, 2, 3, 4)$ are the shape functions corresponding to the four nodes of the rectangular element domain, formulated in the natural coordi-

nates $(\xi, \eta \in [-1, 1])$ [67] as follows

$$\begin{aligned} N_1 &= \frac{1}{4}(1 - \xi)(1 - \eta) \\ N_2 &= \frac{1}{4}(1 + \xi)(1 - \eta) \\ N_3 &= \frac{1}{4}(1 + \xi)(1 + \eta) \\ N_4 &= \frac{1}{4}(1 - \xi)(1 + \eta) \end{aligned} \quad (5.5)$$

Denoting the natural coordinates of node i by (ξ_i, η_i) , the above shape function N_i can be written in a concise form as

$$N_i = \frac{1}{4}(1 + \xi_i \xi)(1 + \eta_i \eta). \quad (5.6)$$

where $\xi_{1,4} = -1$, $\xi_{2,3} = 1$, and $\eta_{1,2} = -1$, $\eta_{3,4} = 1$ (see Fig. 5.7). It is easy to confirm that $\sum_{i=1}^4 N_i = N_1 + N_2 + N_3 + N_4 = 1$.

The coordinates of a point within the element domain is interpolated in terms of the nodal coordinates as

$$\hat{x}(\xi, \eta) = \sum_{i=1}^4 N_i(\xi, \eta) \hat{x}_i, \quad \hat{y}(\xi, \eta) = \sum_{i=1}^4 N_i(\xi, \eta) \hat{y}_i \quad (5.7)$$

where \hat{x}_i and \hat{y}_i are the typical coordinates of node i . Using the chain rule of derivation results in

$$\begin{aligned} \frac{\partial N_i}{\partial \xi} &= \frac{\partial N_i}{\partial \hat{x}} \frac{\partial \hat{x}}{\partial \xi} + \frac{\partial N_i}{\partial \hat{y}} \frac{\partial \hat{y}}{\partial \xi} \\ \frac{\partial N_i}{\partial \eta} &= \frac{\partial N_i}{\partial \hat{x}} \frac{\partial \hat{x}}{\partial \eta} + \frac{\partial N_i}{\partial \hat{y}} \frac{\partial \hat{y}}{\partial \eta} \end{aligned} \quad (5.8)$$

which results in the matrix form

$$\begin{bmatrix} \frac{\partial N_i}{\partial \xi} \\ \frac{\partial N_i}{\partial \eta} \end{bmatrix} = \begin{bmatrix} \frac{\partial \hat{x}}{\partial \xi} & \frac{\partial \hat{y}}{\partial \xi} \\ \frac{\partial \hat{x}}{\partial \eta} & \frac{\partial \hat{y}}{\partial \eta} \end{bmatrix} \begin{bmatrix} \frac{\partial N_i}{\partial \hat{x}} \\ \frac{\partial N_i}{\partial \hat{y}} \end{bmatrix} = \mathbf{J}_e \begin{bmatrix} \frac{\partial N_i}{\partial \hat{x}} \\ \frac{\partial N_i}{\partial \hat{y}} \end{bmatrix} \quad (5.9)$$

s.t.

$$\mathbf{J}_e = \begin{bmatrix} \frac{\partial \hat{x}}{\partial \xi} & \frac{\partial \hat{y}}{\partial \xi} \\ \frac{\partial \hat{x}}{\partial \eta} & \frac{\partial \hat{y}}{\partial \eta} \end{bmatrix} = \begin{bmatrix} \sum_{i=1}^4 \frac{\partial N_i}{\partial \xi} \hat{x}_i & \sum_{i=1}^4 \frac{\partial N_i}{\partial \xi} \hat{y}_i \\ \sum_{i=1}^4 \frac{\partial N_i}{\partial \eta} \hat{x}_i & \sum_{i=1}^4 \frac{\partial N_i}{\partial \eta} \hat{y}_i \end{bmatrix} \quad (5.10)$$

where \mathbf{J}_e is the Jacobian matrix describing the transformation of the derivatives of N_i in local to natural coordinates. For rectangular element $\hat{x} = a\xi$ and $\hat{y} = b\eta$, Jacobian matrix \mathbf{J}_e is

$$\mathbf{J}_e = \begin{bmatrix} a & 0 \\ 0 & b \end{bmatrix}, \quad \text{s.t.} \quad |\det(\mathbf{J}_e)| = ab \quad (5.11)$$

Substituting Eq. (5.11) into Eq. (5.9) yields in

$$\begin{bmatrix} \frac{\partial N_i}{\partial \hat{x}} \\ \frac{\partial N_i}{\partial \hat{y}} \end{bmatrix} = \mathbf{J}_e^{-1} \begin{bmatrix} \frac{\partial N_i}{\partial \xi} \\ \frac{\partial N_i}{\partial \eta} \end{bmatrix} = \begin{bmatrix} \frac{1}{a} & 0 \\ 0 & \frac{1}{b} \end{bmatrix} \begin{bmatrix} \frac{\partial N_i}{\partial \xi} \\ \frac{\partial N_i}{\partial \eta} \end{bmatrix} \quad (5.12)$$

Besides, from Eq. (5.9), the elemental area is determined by

$$d\Omega = d\hat{x}d\hat{y} = |\det(\mathbf{J}_e)| d\xi d\eta = ab d\xi d\eta \quad (5.13)$$

5.5 Element Strain Field

As indicated in [65], the membrane strains $\hat{\epsilon}_m$ of shell is expressed as

$$\begin{aligned}\hat{\epsilon}_m &= \begin{bmatrix} \epsilon_{\hat{x}} \\ \epsilon_{\hat{y}} \\ \gamma_{\hat{x}\hat{y}} \end{bmatrix} = \begin{bmatrix} \frac{\partial u_{\hat{x}}}{\partial \hat{x}} \\ \frac{\partial u_{\hat{y}}}{\partial \hat{y}} \\ \frac{\partial u_{\hat{x}}}{\partial \hat{y}} + \frac{\partial u_{\hat{y}}}{\partial \hat{x}} \end{bmatrix} = \sum_{i=1}^4 \begin{bmatrix} \frac{\partial N_i}{\partial \hat{x}} u_{\hat{x}_i} \\ \frac{\partial N_i}{\partial \hat{y}} u_{\hat{y}_i} \\ \frac{\partial N_i}{\partial \hat{y}} u_{\hat{x}_i} + \frac{\partial N_i}{\partial \hat{x}} u_{\hat{y}_i} \end{bmatrix} \\ &\triangleq \sum_{i=1}^4 \mathbf{B}_{m_i} \hat{\mathbf{d}}_i = \begin{bmatrix} \mathbf{B}_{m_1} & \mathbf{B}_{m_2} & \mathbf{B}_{m_3} & \mathbf{B}_{m_4} \end{bmatrix} \hat{\mathbf{d}} = \mathbf{B}_m \hat{\mathbf{d}}\end{aligned}\quad (5.14)$$

where

$$\mathbf{B}_{m_i} = \begin{bmatrix} \frac{\partial N_i}{\partial \hat{x}} & 0 & 0 & 0 & 0 \\ 0 & \frac{\partial N_i}{\partial \hat{y}} & 0 & 0 & 0 \\ \frac{\partial N_i}{\partial \hat{y}} & \frac{\partial N_i}{\partial \hat{x}} & 0 & 0 & 0 \end{bmatrix} \quad (5.15)$$

Similarly, the bending strains is expressed as

$$\begin{aligned}\hat{\epsilon}_b &= \begin{bmatrix} \kappa_{\hat{x}} \\ \kappa_{\hat{y}} \\ \kappa_{\hat{x}\hat{y}} \end{bmatrix} = \begin{bmatrix} \frac{\partial \theta_{\hat{x}}}{\partial \hat{x}} \\ \frac{\partial \theta_{\hat{y}}}{\partial \hat{y}} \\ \frac{\partial \theta_{\hat{x}}}{\partial \hat{y}} + \frac{\partial \theta_{\hat{y}}}{\partial \hat{x}} \end{bmatrix} = \sum_{i=1}^4 \begin{bmatrix} \frac{\partial N_i}{\partial \hat{x}} \theta_{\hat{x}_i} \\ \frac{\partial N_i}{\partial \hat{y}} \theta_{\hat{y}_i} \\ \frac{\partial N_i}{\partial \hat{y}} \theta_{\hat{x}_i} + \frac{\partial N_i}{\partial \hat{x}} \theta_{\hat{y}_i} \end{bmatrix} \\ &\triangleq \sum_{i=1}^4 \mathbf{B}_{b_i} \hat{\mathbf{d}}_i = \begin{bmatrix} \mathbf{B}_{b_1} & \mathbf{B}_{b_2} & \mathbf{B}_{b_3} & \mathbf{B}_{b_4} \end{bmatrix} \hat{\mathbf{d}} = \mathbf{B}_b \hat{\mathbf{d}}\end{aligned}\quad (5.16)$$

where

$$\mathbf{B}_{b_i} = \begin{bmatrix} 0 & 0 & 0 & \frac{\partial N_i}{\partial \hat{x}} & 0 \\ 0 & 0 & 0 & 0 & \frac{\partial N_i}{\partial \hat{y}} \\ 0 & 0 & 0 & \frac{\partial N_i}{\partial \hat{y}} & \frac{\partial N_i}{\partial \hat{x}} \end{bmatrix} \quad (5.17)$$

Also, the transverse shear strains are approximated as

$$\begin{aligned}\hat{\boldsymbol{\epsilon}}_s &= \begin{bmatrix} \gamma_{\hat{x}\hat{z}} \\ \gamma_{\hat{y}\hat{z}} \end{bmatrix} = \begin{bmatrix} \frac{\partial u_{\hat{z}}}{\partial \hat{x}} - \theta_{\hat{x}} \\ \frac{\partial u_{\hat{z}}}{\partial \hat{y}} - \theta_{\hat{y}} \end{bmatrix} = \sum_{i=1}^4 \begin{bmatrix} \frac{\partial N_i}{\partial \hat{x}} u_{\hat{z}_i} - N_i \theta_{\hat{x}_i} \\ \frac{\partial N_i}{\partial \hat{y}} u_{\hat{z}_i} - N_i \theta_{\hat{y}_i} \end{bmatrix} \\ &\triangleq \sum_{i=1}^4 \mathbf{B}_{s_i} \hat{\mathbf{d}}_i = \begin{bmatrix} \mathbf{B}_{s_1} & \mathbf{B}_{s_2} & \mathbf{B}_{s_3} & \mathbf{B}_{s_4} \end{bmatrix} \hat{\mathbf{d}} = \mathbf{B}_s \hat{\mathbf{d}}\end{aligned}\quad (5.18)$$

where

$$\mathbf{B}_{s_i} = \begin{bmatrix} 0 & 0 & \frac{\partial N_i}{\partial \hat{x}} & -N_i & 0 \\ 0 & 0 & \frac{\partial N_i}{\partial \hat{y}} & 0 & -N_i \end{bmatrix} \quad (5.19)$$

From Eqs. (5.14)–(5.18), combining the expression for the generalized local strain vectors gives

$$\hat{\boldsymbol{\epsilon}} = \begin{bmatrix} \hat{\boldsymbol{\epsilon}}_m \\ \hat{\boldsymbol{\epsilon}}_b \\ \hat{\boldsymbol{\epsilon}}_s \end{bmatrix} = \begin{bmatrix} \mathbf{B}_m \\ \mathbf{B}_b \\ \mathbf{B}_s \end{bmatrix} \hat{\mathbf{d}} \triangleq \mathbf{B} \hat{\mathbf{d}} \quad (5.20)$$

On the other hand, the stress vector is express as

$$\hat{\boldsymbol{\sigma}} = \mathbf{C} \hat{\boldsymbol{\epsilon}}, \quad \text{with} \quad \mathbf{C} = \begin{bmatrix} \mathbf{C}_m & \mathbf{0} & \mathbf{0} \\ \mathbf{0} & \mathbf{C}_b & \mathbf{0} \\ \mathbf{0} & \mathbf{0} & \mathbf{C}_s \end{bmatrix}, \quad (5.21)$$

with \mathbf{C}_m , \mathbf{C}_b , and \mathbf{C}_s the constitutive matrices of the membrane, bending, and transverse behaviors, respectively, are

$$\mathbf{C}_m = \frac{Et}{1-\nu^2} \begin{bmatrix} 1 & \nu & 0 \\ \nu & 1 & 0 \\ 0 & 0 & \frac{1-\nu}{2} \end{bmatrix}, \quad (5.22)$$

$$\mathbf{C}_b = \frac{t^2}{12} \mathbf{D}_m, \quad (5.23)$$

$$\mathbf{C}_s = \frac{\kappa Et}{2(1+\nu)} \begin{bmatrix} 1 & 0 \\ 0 & 1 \end{bmatrix} \quad (5.24)$$

where E , ν , and t are Young's modulus, Poisson's ratio, and thickness of the shell, respectively, and for elastic material, the shear correction factor is $\kappa = 5/6$.

5.6 Element Equation

The static state of an element in equilibrium can be obtained by applying the principle of virtual work (PVW) on its local domain (see Fig. 5.7) as

$$\underbrace{\int_{\Omega} \delta \hat{\boldsymbol{\epsilon}}^\top \hat{\boldsymbol{\sigma}} \, d\Omega}_{\text{Internal virtual strain energy}} = \underbrace{\int_{\Omega} \delta \hat{\mathbf{u}}^\top \hat{\mathbf{s}} \, d\Omega + \delta \hat{\mathbf{d}}^\top \hat{\mathbf{f}}^{\text{ext}}}_{\text{External virtual work}} \quad (5.25)$$

where $\hat{\mathbf{f}}^{\text{ext}} \in \mathbb{R}^{20}$ are the external concentrated forces. The surface load \mathbf{s} of the inner air pressure P is given by

$$\hat{\mathbf{s}} = \begin{bmatrix} 0 \\ 0 \\ P \\ 0 \\ 0 \end{bmatrix} \quad (5.26)$$

Substituting Eqs. (5.3), (5.21), (5.20), and (5.26) into Eq. (5.25) results in

$$\hat{\mathbf{k}}\hat{\mathbf{d}} = \hat{\mathbf{f}}_{\text{pressured}} + \hat{\mathbf{f}}^{\text{ext}}. \quad (5.27)$$

where the distributed forces $\hat{\mathbf{f}}_{\text{pressured}} \in \mathbb{R}^{20}$ resulting from inner air pressure P is calculated as

$$\hat{\mathbf{f}}_{\text{pressured},i} = \int_{\Omega} \mathbf{N}_i \hat{\mathbf{s}} d\Omega = \begin{bmatrix} 0 \\ 0 \\ abP \\ 0 \\ 0 \end{bmatrix} \propto P, \quad (5.28)$$

and the local element stiffness matrix $\hat{\mathbf{k}} \in \mathbb{R}^{20 \times 20}$ is computed as

$$\begin{aligned} \hat{\mathbf{k}} &= \int_{\Omega} \mathbf{B}^T \mathbf{C} \mathbf{B} d\Omega = \int_{-1}^1 \int_{-1}^1 [\mathbf{B}(\xi, \eta)]^T \mathbf{C} \mathbf{B}(\xi, \eta) ab d\xi d\eta \\ &\triangleq \int_{-1}^1 \int_{-1}^1 \mathbf{g}(\xi, \eta) d\xi d\eta \end{aligned} \quad (5.29)$$

The integral of the term $\mathbf{g}(\xi, \eta) = ab[\mathbf{B}(\xi, \eta)]^T \mathbf{C} \mathbf{B}(\xi, \eta)$ over the normalized isoparametric quadrilateral domain ($\xi, \eta \in [-1, 1]$) can be conveniently

Points n_p/n_q	Coordinates ξ_p/η_q	Weight W_p/W_q
1	0.0	2.0
2	± 0.5773502692	1.0
3	± 0.774596697 0.0	0.5555555556 0.8888888889
4	± 0.8611363116 ± 0.3399810436	0.3478548451 0.6521451549

Table 5.1: Coordinates and weights for Gauss integration [66].

evaluated by using a 2-D Gauss quadrature [66] as below

$$\hat{\mathbf{k}} = \int_{-1}^1 \int_{-1}^1 \mathbf{g}(\xi, \eta) d\xi d\eta \approx \sum_{p=1}^{n_p} \sum_{q=1}^{n_q} \mathbf{g}(\xi_p, \eta_q) W_p W_q \quad (5.30)$$

where n_p and n_q are the number of integration points along each natural coordinate ξ and η , respectively, while ξ_p and η_q are the integration points with the corresponding weights W_p and W_q , respectively. In this paper, the four Gauss points (i.e., $n_p = 2$, $n_q = 2$) shown in Table 5.1 was used to approximate the integration of $\hat{\mathbf{k}}$ in Eq. (5.30).

5.7 Global Finite Element Equation

Note that although the stiffness $\hat{\mathbf{k}}^{(e)}$ of element $e = 1-N_e$ in the local coordinates is the same (because discretized rectangular domain $a \times b$ and the local coordinate system of every element is identical), these elements locate on different planes (orientation). Therefore, to assemble the global equation of the system, the element equation (5.27) must be expressed in the global coordinates, given by:

$$\mathbf{k}\mathbf{d} = \mathbf{f}_{\text{pressured}} + \mathbf{f}^{\text{ext}}. \quad (5.31)$$

The relationship between displacements in the local and global coordinates is described by the transformation matrix $\mathbf{L}^{(e)} \in \mathbb{R}^{20 \times 24}$ as

$$\hat{\mathbf{d}}^{(e)} = \mathbf{L}^{(e)} \mathbf{d}^{(e)}, \quad \mathbf{d}^{(e)} = [\mathbf{L}^{(e)}]^\top \hat{\mathbf{d}}^{(e)} \quad (5.32)$$

with

$$\mathbf{L}^{(e)} = \text{diagblock}(\mathbf{L}_1^{(e)}, \mathbf{L}_2^{(e)}, \mathbf{L}_3^{(e)}, \mathbf{L}_4^{(e)}) \quad (5.33)$$

The stiffness matrix and force vector are also calculated as below

$$\mathbf{k}^{(e)} = [\mathbf{L}^{(e)}]^\top \hat{\mathbf{k}}^{(e)} \mathbf{L}^{(e)}, \quad \mathbf{f}_{\text{pressured}}^{(e)} = [\mathbf{L}^{(e)}]^\top \hat{\mathbf{f}}_{\text{pressured}}^{(e)}. \quad (5.34)$$

As the flat element, the transformation matrices $\mathbf{L}_i^{(e)} (i = 1, 2, 3, 4)$ of the element e are identical for 4-nodes, determined as follows

$$\mathbf{L}_i^{(e)}(\phi) = \begin{bmatrix} 0 & 0 & -1 & 0 & 0 & 0 \\ -\sin(\phi) & \cos(\phi) & 0 & 0 & 0 & 0 \\ \cos(\phi) & \sin(\phi) & 0 & 0 & 0 & 0 \\ 0 & 0 & 0 & \sin(\phi) & -\cos(\phi) & 0 \\ 0 & 0 & 0 & 0 & 0 & -1 \end{bmatrix} \in \mathbb{R}^{5 \times 6} \quad (5.35)$$

where $\phi = (\ell - 0.5)\gamma$ is the angular position of an element e at path ℓ shown in Fig. 5.7.

The global equation of the FE model is then established by assembling together all Eq. (5.31) of elements $e = 1, 2, \dots, N_e$ based on the connected nodes in the meshing topology. The assembly algorithm adds up the contribution of all element connected at a node, resulting in

$$\mathbf{KD} = \mathbf{F}_{\text{pressured}} + \mathbf{F}^{\text{ext}} \quad (5.36)$$

where \mathbf{K} is the global stiffness matrix (structural stiffness); $\mathbf{F}_{\text{pressured}}, \mathbf{F}^{\text{ext}}$

and \mathbf{D} are the global force vectors and displacement vector which contain forces and displacements of all nodes, respectively, i.e.,

$$\mathbf{F}_i = \begin{bmatrix} F_{\hat{X}_i} \\ F_{\hat{Y}_i} \\ F_{\hat{Z}_i} \\ M_{\hat{X}_i} \\ M_{\hat{Y}_i} \\ M_{\hat{Z}_i} \end{bmatrix}, \quad \hat{\mathbf{D}}_i = \begin{bmatrix} u_{\hat{X}_i} \\ u_{\hat{Y}_i} \\ u_{\hat{Z}_i} \\ \theta_{\hat{X}_i} \\ \theta_{\hat{Y}_i} \\ \theta_{\hat{Z}_i} \end{bmatrix}, \quad \text{with } i = 1-N \quad (5.37)$$

On the other hand, as the skin of the TacLINK is clamped at both ends, therefore the degrees of freedom of all nodes are set to a zero value. The boundary conditions of the FE equation (5.36) can be expressed as:

$$\mathbf{D}_i = \mathbf{0}, \quad \forall i \in \mathcal{B}_1 \cup \mathcal{B}_2 \quad (5.38)$$

5.8 Simulation Result

To verify the ability of the FE model to describe and simulate the physical characteristics and response of the skin, the model was built numerically and implemented in MATLAB. Young's modulus of silicone material was calibrated to be 0.1 MPa (see Section 5.9) and Poisson's ratio was set as 0.5.

TacLINK could be simulated under multiple contacts at different locations with varied inner air pressure. The displacement vector \mathbf{D} in Eq. (5.36) is basically solvable with the boundary conditions in Eq. (5.38), as indicated in [68], i.e., the modified system of Eq. (5.36) could be written as

$$\bar{\mathbf{K}}\bar{\mathbf{D}} = \bar{\mathbf{F}} \quad (5.39)$$

where the modified matrix $\bar{\mathbf{K}}$ is obtained from matrix \mathbf{K} by removing rows and columns corresponding to degrees of freedom of nodes constrained by

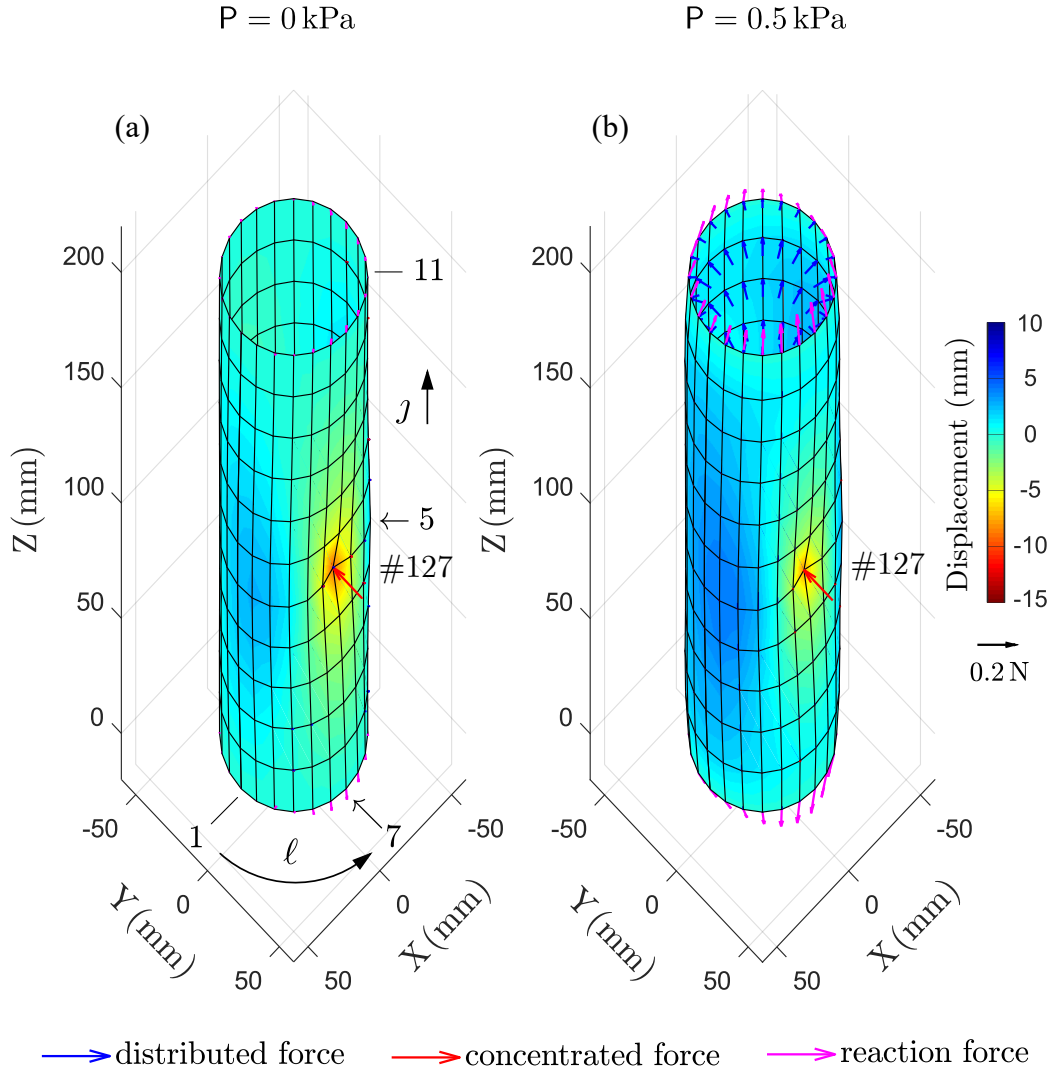


Figure 5.8: FE model simulation results for soft artificial skin. (a) Skin deformation by a normal force 0.2 N at node #127(7,5). (b) Response of skin to additional inner air pressure $P = 0.5 \text{ kPa}$.

boundary condition Eq. (5.38) i.e., fixed nodes $i \in \mathcal{B}_1 \cup \mathcal{B}_2$ at two ends of the skin. Similarly, eliminating the these rows of system force vector $\mathbf{F} = \mathbf{F}_{\text{pressured}} + \mathbf{F}^{\text{ext}}$ results in modified system force vector $\bar{\mathbf{F}}$.

As a result, the modified displacement is easily derived as

$$\bar{\mathbf{D}} = [\bar{\mathbf{K}}]^{-1} \bar{\mathbf{F}} \quad (5.40)$$

Once the modified displacement vector $\bar{\mathbf{D}}$ is determined, combining with boundary condition Eq. (1.1), the system displacement vector \mathbf{D} is obtained. Then, the system force vector is determined as follows

$$\mathbf{F} = \mathbf{KD} \rightarrow \mathbf{F}^{\text{ext}} = \mathbf{F} - \mathbf{F}_{\text{pressured}} \quad (5.41)$$

in which the acting forces exerting on the skin body are $\mathbf{F}_i^{\text{ext}}$ with $i \in \mathcal{N}$, while the reaction forces exerting on constrained nodes are $\mathbf{F}_i^{\text{ext}}$ with $i \in \mathcal{B}_1 \cup \mathcal{B}_2$.

Fig. 5.8 illustrates results of subjecting the TacLINK to a normal force 0.2 N at node #127(7, 5), as shown in Fig. 5.8(a). Moreover, the application of additional inner pressure of 0.5 kPa was also simulated, and shown in Fig. 5.8(b). The simulation results indicate that the finite element modeling can robustly provide a realistic response of the skin, including 3-D deformation, strain, stress, and reaction forces at fixed ends. Based on the FE modeling technique, we can evaluate the overall stiffness of the skin to evaluate the performance and choose the suitable skin material for a specified application. Besides, structural stiffness is the key technique to determine the contact force, in which the displacement is measured by the vision system.

5.9 Young's modulus Calibration

In this system, the elastic Young's modulus E of the skin material was estimated from a compression test performed under quasi-static conditions. Air was provided at different levels of pressure $P \in \mathcal{P} = \{0.5, 1.0, 1.5\}$ kPa. The experiment has conducted a total of 30 times.

In this experiment, the air was provided slowly to avoid undesired influences. During inflation, a testing program automatically recorded deforma-

tion data at these designed pressures. The inner air pressure is detected by a pressure sensor MPXV7007 (NXP Inc., USA) with a range of -7 to 7 kPa and output of 0 to 5 V, which is measured via a high speed (50 kS/s) 16-bit ADC data acquisition board USB-231 (Measurement Computing Corp., USA) with a range of -10 to 10 V. Thus, the resolution of this ADC pressure measurement is 1 LSB(least significant bit) = $\frac{7000 - (-7000)}{5} \times \frac{10 - (-10)}{2^{16}-1} \approx 0.85$ Pa.

As a result, the parameter E is obtained by minimizing the difference between experimentally determined deformation and deformation predicted by the FE model as below

$$\min_E \underbrace{\sum_{P \in \mathcal{P}} \left\| \mathbf{D}_{\text{measured}} - \frac{E^*}{E} \mathbf{D}_{\text{FEM}^*} \right\|^2}_{f(E)} \quad (5.42)$$

where $\mathbf{D}_{\text{measured}}$ and $\mathbf{D}_{\text{FEM}^*}$ are the displacement vectors obtained from experimental data and the FE model, respectively. Here, the linear FE model is preassigned with Young's modulus $E^* = 1$ MPa.

The sum of the squares errors in Eq. (5.42) could be written in a quadratic function of $\left(\frac{E^*}{E}\right)$ as follows

$$\begin{aligned} f(E) &= \\ &\sum_{P \in \mathcal{P}} \left(\left\| \mathbf{D}_{\text{FEM}^*} \right\|^2 \frac{E^{*2}}{E^2} - 2 \mathbf{D}_{\text{measured}} \cdot \mathbf{D}_{\text{FEM}^*} \frac{E^*}{E} + \left\| \mathbf{D}_{\text{measured}} \right\|^2 \right) = \\ &\underbrace{\left(\sum_{P \in \mathcal{P}} \left\| \mathbf{D}_{\text{FEM}^*} \right\|^2 \right) \frac{E^{*2}}{E^2}}_A - 2 \underbrace{\left(\sum_{P \in \mathcal{P}} \mathbf{D}_{\text{measured}} \cdot \mathbf{D}_{\text{FEM}^*} \right)}_B \frac{E^*}{E} + \underbrace{\left(\sum_{P \in \mathcal{P}} \left\| \mathbf{D}_{\text{measured}} \right\|^2 \right)}_C \\ &= A \left(\frac{E^*}{E} \right)^2 + B \left(\frac{E^*}{E} \right) + C, \quad \text{with } \frac{E^*}{E} > 0. \end{aligned} \quad (5.43)$$

Obviously, the quadratic equation (5.43) minimized if

$$\frac{E^*}{E} = \frac{B}{2A} = \frac{\sum_{P \in \mathcal{P}} \mathbf{D}_{\text{measured}} \cdot \mathbf{D}_{\text{FEM}^*}}{\sum_{P \in \mathcal{P}} \|\mathbf{D}_{\text{FEM}^*}\|^2} \quad (5.44)$$

so that

$$E = E^* \frac{\sum_{P \in \mathcal{P}} \|\mathbf{D}_{\text{FEM}^*}\|^2}{\sum_{P \in \mathcal{P}} \mathbf{D}_{\text{measured}} \cdot \mathbf{D}_{\text{FEM}^*}} \quad (5.45)$$

Therefore, based on the measured displacements of markers providing by the vision system, Young's modulus E can be easily derived as in Eq. (5.45).

Note that vectors $\mathbf{D}_{\text{measured}}$ and $\mathbf{D}_{\text{FEM}^*}$ in Eq. (5.45) require displacement of all nodes, however, because of the symmetric shape of the FE model under inner air pressure (i.e., similar curvature of every path), the experimental displacement of all paths was averaged to compute the path curvature instead. Fig. 5.9 shows the path curvature of ten nodes on a path along the skin, together with the theoretical curvature (lines) of the FE model in response to varying levels of inner pressure. The experimental data fit those of the FE model well with an estimated Young's modulus value $E \approx 0.1 \text{ MPa}$. The average RMSE for 3-D nodal displacements is 0.38 mm.

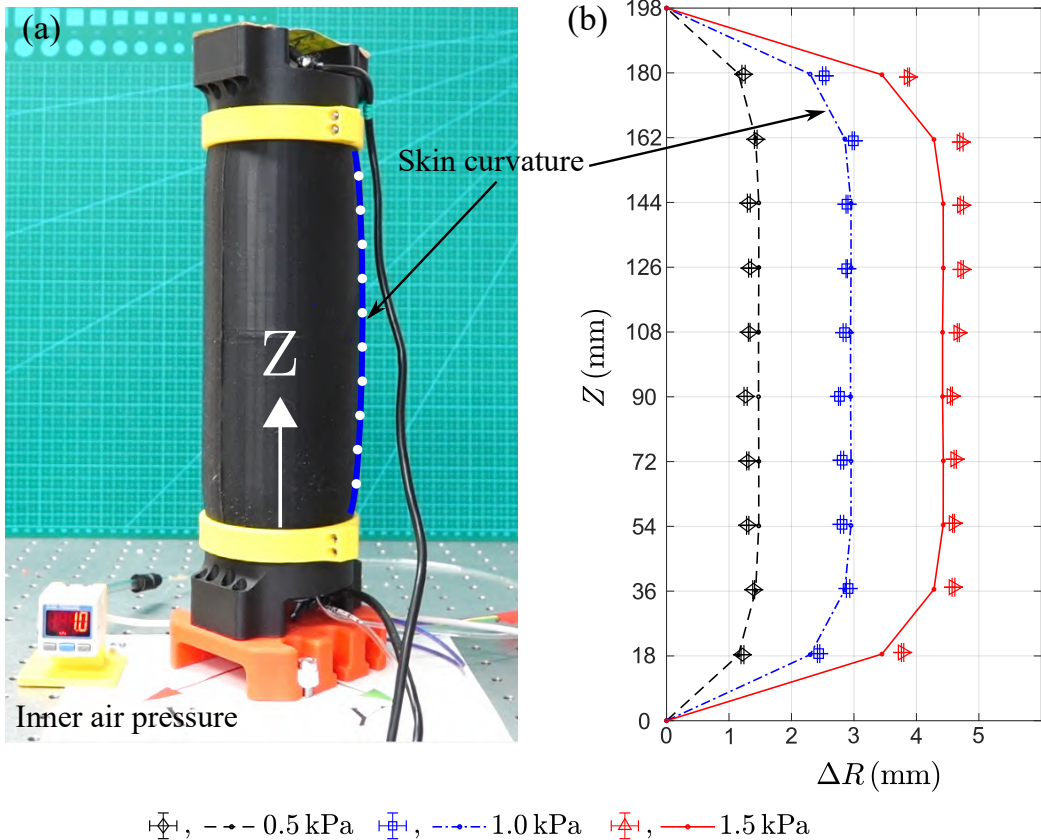


Figure 5.9: Inflation experiment for calibrating Young's modulus of the silicone material (Ecoflex 00-50). (a) Measuring the curvature of the skin under inner air pressure. (b) Comparison of experimental data (solids) and FE model (lines) with calibrated Young's modulus E of skin curvature in response to applied inner pressures of 0.5, 1, and 1.5 kPa.

5.10 Summary

In this chapter, the finite element method for solving problems in structure modeling is introduced. Here, artificial skin is discretized into a FE mesh of $N_e = 264$ flat rectangular shell elements with a total of $N = 288$ nodes. The formulation of conventional flat shell elements is introduced, including defining element geometry, computing elemental displacement, strain, and stress fields. The element equation is then derived, and the global equation is established by assembling all element equations. The structural stiffness of the skin is therefore obtained, enabling simulate and predict the performance of the skin to optimize the design, as well as choose suitable skin material for a specified application.

Based on the FE model, Young's modulus of Ecoflex 00-50 material was calibrated by a compression test i.e., $E \approx 0.1 \text{ MPa}$. Importantly, thanks to structural stiffness describing the relationship between nodal forces and displacements, the tactile force of TacLINK representing the external contact force can be determined, in which the displacements are provided by the vision system. Thus, the finite element method in this chapter enables the complete modeling technique for the finite element model of artificial skin with shell structure to be realized.

Chapter 6

Tactile Force Reconstruction

6.1 Tactile Force Calculation

The finite element model shown in Eq. (5.36) give the specific relationship between forces and displacements, enabling tactile sensing forces $\mathbf{F}^{\text{tac}} \in \mathbb{R}^{6N}$ of TacLINK can be defined as the external force \mathbf{F}^{ext} acting on the skin surface, excluding the distributed forces generated by inner air pressure $\mathbf{F}_{\text{pressured}}$. From Eq. (5.36), the tactile forces are computed as follows

$$\mathbf{F}^{\text{tac}} = \mathbf{K}\mathbf{D}_{\text{measured}} - \mathbf{F}_{\text{pressured}}. \quad (6.1)$$

where equivalent distributed force vector $\mathbf{F}_{\text{pressured}}$ is computed from measured pressure P of the pressure sensor [see Eq. (5.28)].

Note that because of limitation of the vision system, the scope of this system considers only measured translations (u_X, u_Y, u_Z) and force components (F_X, F_Y, F_Z). The degrees of freedom of nodal rotations ($\theta_X, \theta_Y, \theta_Z$) and moments (M_X, M_Y, M_Z) are ignored. Therefore, the measured nodal displacement vector $\mathbf{D}_{\text{measured}}$ is derived from the coordinates vector \mathbf{X} of

the vision system (see Section 4.4) as below

$$\mathbf{D}_{\text{measured},i} = \begin{bmatrix} \underbrace{\Delta \mathbf{X}_i^\top}_{\text{translations}} & \underbrace{\begin{matrix} 0 & 0 & 0 \end{matrix}}_{\text{rotations}} \end{bmatrix}^\top, \forall i \in \mathcal{N}. \quad (6.2)$$

where $\Delta \mathbf{X} = \mathbf{X} - \mathbf{x}$, with $\mathbf{x} \in \mathbb{R}^{3N}$ the initial coordinates vector of nodes in the undeformed state of the skin, i.e., $\mathbf{x}_i = [X_{0i} \ Y_{0i} \ Z_{0i}]^\top, \forall i \in \mathcal{N}$.

6.2 Sensitivity Analysis

Noticing that the tactile force vector \mathbf{F}^{tac} is computed from a large number of sampling points i.e., $N = 288$ nodes with $3 \times N$ force components and $3 \times N$ torque components. Obviously, errors during 3-D reconstruction significantly induce errors in force calculations, as well as because of the cylindrically shaped skin surface, we simulated to evaluate this effect in the tangential, axial, and radial directions.

For ease of analysis, let us assume that δ_{error} mm is the absolute error in every direction, i.e., $\delta_{\text{error}}^X = \delta_{\text{error}}^Y = \delta_{\text{error}}^Z = \delta_{\text{error}}$. In this simulated analysis, node #127 (see Fig. 6.1) is chosen and constrained in the tangential (X -axis), radial (Y -axis), and axial (Z -axis) deflections as follows

$$\mathbf{D}_{127} := \begin{bmatrix} \delta_{\text{error}}(\text{mm}) \\ \delta_{\text{error}}(\text{mm}) \\ \delta_{\text{error}}(\text{mm}) \\ 0(\text{rad}) \\ 0(\text{rad}) \\ 0(\text{rad}) \end{bmatrix} \quad (6.3)$$

Then, solving with finite element equation (5.36) and boundary condition

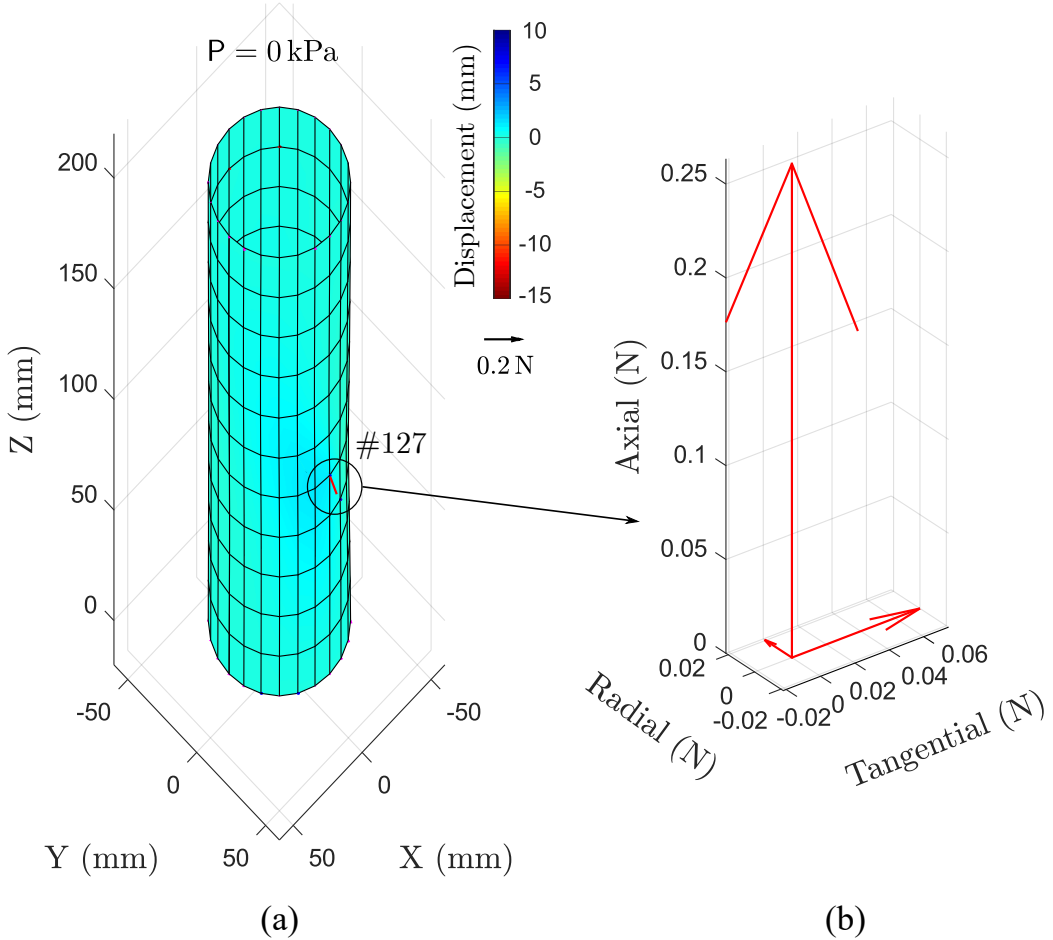


Figure 6.1: FE model simulation of the reaction force at node #127(7,5) for evaluating the force reconstruction error in each direction. (a) The response of the skin constrained at node #127 by Eq. (6.3). (b) Illustration of three tangential, radial, and axial components of the reaction force at node #127.

(5.38), the reaction force is derived at node #127 as below

$$\mathbf{F}_{127} = \begin{bmatrix} 0.08\delta_{\text{error}}(\text{N}) \\ 0.02\delta_{\text{error}}(\text{N}) \\ 0.30\delta_{\text{error}}(\text{N}) \\ 0(\text{N} \cdot \text{mm}) \\ 0(\text{N} \cdot \text{mm}) \\ 0(\text{N} \cdot \text{mm}) \end{bmatrix} \quad (6.4)$$

The results shown in Eq. (6.4) reveals that spatial measurement errors of the vision system result in much higher errors of force reconstruction in the tangential (i.e., ~ 4 times) and axial (i.e., ~ 15 times) directions than in the radial direction. Besides, with the configuration of the cylindrical skin surface, under conditions of normal contact, the radial displacement would be much greater than displacements in other directions, making it more accurately detected by the vision system. Therefore, to ensure the reliability of each nodal force, only force component in the radial direction is considered, i.e.,

$$F_{R_i}^{\text{tac}} = F_{X_i} \cos \varphi_i + F_{Y_i} \sin \varphi_i, \quad \forall i \in \mathcal{N} \quad (6.5)$$

where F_{X_i} and F_{Y_i} are the force components on the X - and Y -axes of node i , respectively, with its angular coordinate is denoted by φ_i . Thus, the computed tactile force at node $i \in \mathcal{N}$ is then given as follows

$$\mathbf{F}_i^{\text{tac}} = \begin{bmatrix} F_{R_i}^{\text{tac}} \cos \varphi_i & F_{R_i}^{\text{tac}} \sin \varphi_i & \underbrace{\dots}_{\text{ignoring}} \end{bmatrix}^\top \in \mathbb{R}^6 \quad (6.6)$$

On the other hand, for practical reasons, we should only consider the computed force F_R that is above a certain threshold f_{thresh} , i.e., $F_R > f_{\text{thresh}} = 0.02\delta_{\text{error}}(N)$ [see Eq. (6.4)]. Finally, the tactile forces regarded as the concentrated forces acting at free nodes/markers are $\mathbf{F}_i^{\text{tac}}, \forall i \in \mathcal{M}$, and the reaction forces exerting at two boundary edges of TacLINK are $\mathbf{F}_i^{\text{tac}}, \forall i \in \mathcal{B}_1 \cup \mathcal{B}_2$.

6.3 Experimental Evaluation

6.3.1 Experimental Setup

The experimental platform shown in Fig. 6.2 set up to evaluate the operation of the TacLINK. Within the platform, TacLINK is fixed in a rigid vertical

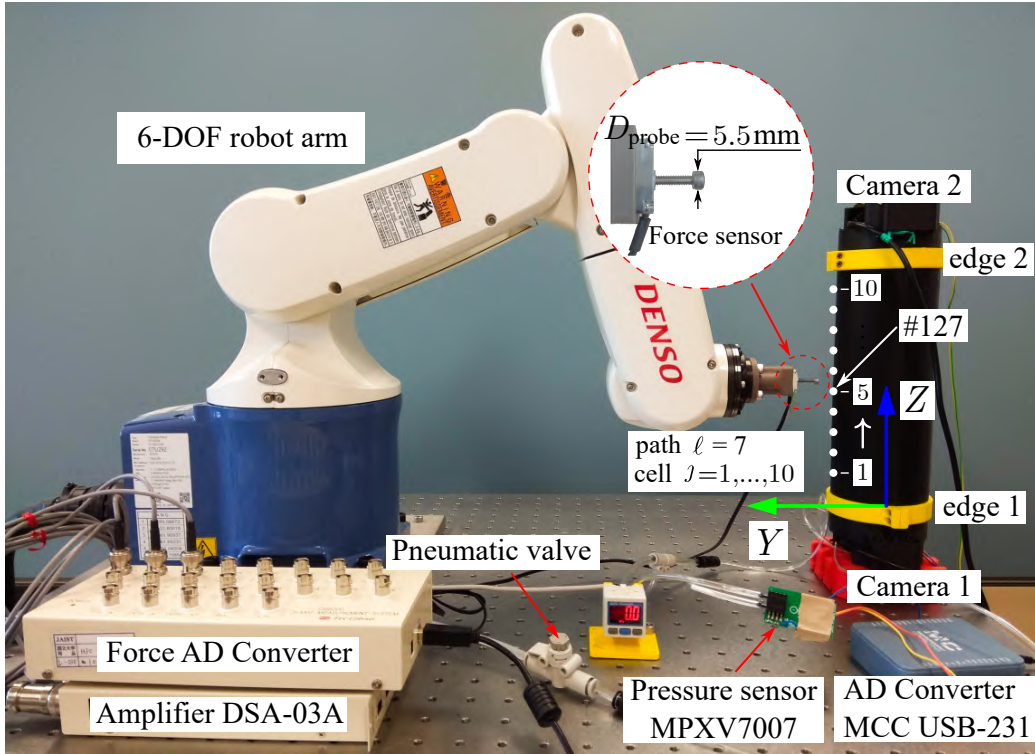


Figure 6.2: The experimental platform for measurement.

position. The inner pressure is adjusted by using a pneumatic throttle valve. The pressure is detected by a pressure sensor (MPXV7007, NXP Inc., USA) with a measurement range of -7 kPa to 7 kPa and output of 0 V to 5 V which is measured accurately through a 16-bit ADC data acquisition board (USB-231, Measurement Computing Corp., USA). The resolution of this pressure measurement is about 0.85 Pa . In order to provide precise displacement of external contact with the skin surface, a 6-DOF robotic arm (VP-6242, Denso Robotics, Japan) is used (see Fig. 6.2). The robot arm can precisely displace with high repeatability of $\pm 0.02\text{ mm}$. A probe was attached to the center of the robot's end-effector through a 3-axes force sensor (USL06-H5-50N, Tec Gihan, Japan). Note that in order to accurately push the entire cross-sectional area of the marker, we utilized a cylindrical probe as a standard

screw M3 with a larger diameter of $D_{\text{probe}} = 5.5$ mm. In this experiment, the robot was installed to drive the probe in-plane OYZ and push it horizontally against the skin at different nodes on the seventh path, i.e., $\ell = 7$ shown in Fig. 6.2. Note that although the ideal probe for point load should be narrow enough to represent a point load, a small probe may cause damage and undesired deformation in the thickness direction at the contact point. Therefore, to mitigate these issues, the cylindrical probe of diameter D_{probe} was throughout used.

The experiment software environment was run on a desktop computer with specifications: processor i7-7700 running at 3.60 GHz with 8 GB of RAM memory. The testing software performed on MATLAB environment in real-time at about 13 Hz, with time to capture stereo pictures ~ 0.003 s, image processing ~ 0.025 s, stereo registration algorithm ~ 0.037 s, and both 3-D shape and force reconstruction completed within 0.0002 s. Thus, the most processing time is for image processing and stereo registration, yet, the computation time for the proposed 3-D shape and force is very rapid. Note that the testing computer based on Microsoft Windows 10 operating system had also to run many irrelevant tasks due to the MATLAB environment, as well as other applications.

6.3.2 Single Point Contact

The finite element model of the skin in Eq. (5.36) enables TacLINK to estimate the external force distribution acting on the whole skin body \mathbf{F}^{tac} (i.e., tactile force) shown in Eq. (6.1) with $\mathbf{F}_i^{\text{tac}}, \forall i \in \mathcal{M}$. Thus, this experiment is to evaluate the tactile force-sensing ability and assess the sensing characteristics of TacLINK when contacting at a single point under varying condition of inner air pressures.

In this experiment, the probe was controlled to push horizontally the skin surface at the node #127 along the Y-axis creating accurately two desired radial displacements $\Delta R = -5.0$ mm and $\Delta R = -10.0$ mm, as shown in

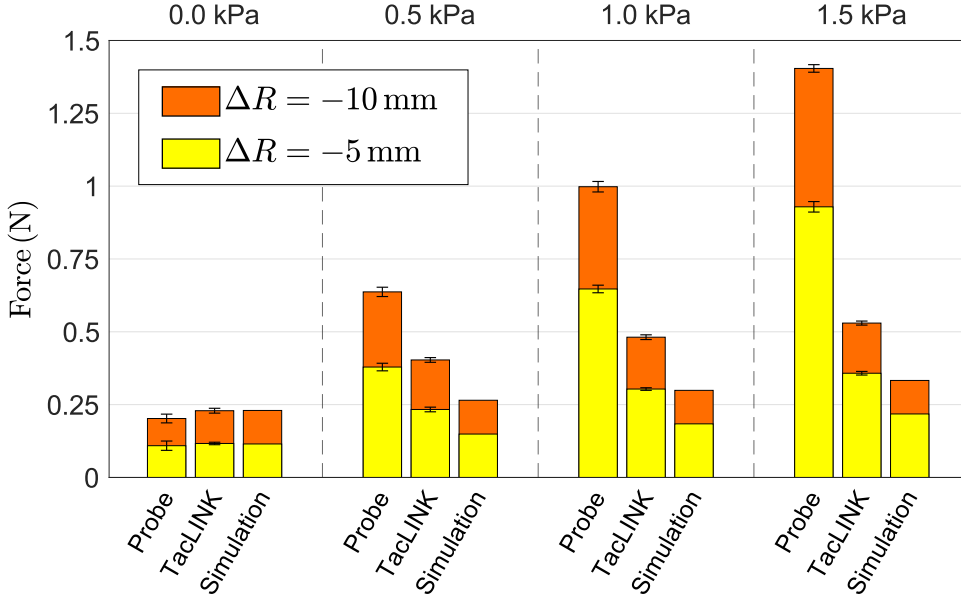


Figure 6.3: Probe forces applied yielding radial deflections ΔR at node #127 compared with the nodal tactile forces at node #127 obtained from TacLINK and simulation under different inner air pressures.

Fig. 6.2. For each designed position, the inner air pressure was controlled at different level of pressure $P = 0, 0.5, 1.0$, and 1.5 kPa , allowing a software to automatically record stereo images that outputs the tactile forces \mathbf{F}^{tac} . This experiment was carried in ten times.

On the other hand, the tactile force of TacLINK was also simulated by setting an additional boundary condition for the finite element model in Eq. (5.36) on the Y -axis as

$$\mathbf{D}_{127,Y} = \Delta R, \quad \text{where} \quad \mathbf{D}_{127} = \begin{bmatrix} \mathbf{D}_{127,X} \\ \mathbf{D}_{127,Y} \\ \mathbf{D}_{127,Z} \\ \mathbf{D}_{127,\theta_X} \\ \mathbf{D}_{127,\theta_Y} \\ \mathbf{D}_{127,\theta_Z} \end{bmatrix} \quad (6.7)$$

Solving Eq. (5.36) with boundary conditions Eqs. (5.38) and (6.7) yields to system force vector \mathbf{F}^{ext} . As a result, the results of the probe force and the tactile forces at node #127 resulting from TacLINK (i.e., $\mathbf{F}_{127}^{\text{tac}}$) and simulation (i.e., $\mathbf{F}_{127}^{\text{ext}}$) at each level of deflection ΔR and pressure P are shown in Fig. 6.3. Besides, the performance of whole body tactile force sensing at each pressure level of $P = 0, 0.5, 1.0$, and 1.5 kPa is also shown in Fig. 6.4, 6.5, 6.6, and 6.7, respectively.

In the absence of inner air pressure (i.e., $P = 0 \text{ kPa}$), the resultant forces of probe, TacLINK, and simulation matched well at every created deflection $\Delta R = -5.0 \text{ mm}$ and $\Delta R = -10.0 \text{ mm}$, as shown in Fig. 6.3. When pressured ($P > 0 \text{ kPa}$), the resultant forces change linearly in terms of displacement and pressure. However, the nodal tactile force of TacLINK is slightly higher than FE simulation but significantly lower than the probe force.

The difference when air supplied may be mainly due to the real probe not being small enough (i.e., $D_{\text{probe}} \gg 0$) to represent an ideal point load contact scenario as in FEM simulation. The inner air pressure acting on the inner wall of the skin surface gave rise to tension stresses circumferential σ_y and longitudinal σ_x stresses in its wall that results in a highly increased probe force to move the probe with finite contact area $S_{\text{probe}} = \frac{\pi}{4} D_{\text{probe}}^2 = 23.8 \text{ mm}^2 \gg 0$ that obviously caused greater deformed contact area surrounding the contacted node #127. As well as, the divided size of FE mesh ($2a = 9.5 \text{ mm}$, $2b = 18 \text{ mm}$) was also not dense enough to describe actual deformation of the skin surface in the contact area created by the probe, i.e., $2a \times 2b \gg S_{\text{probe}}$. The computed whole-body tactile force sensing of TacLINK representing the probe force contact would also distribute on the neighbor nodes, but the largest nodal tactile force should be at contacted node #127, which are indicated intuitively in Figures 6.4–6.7.

Besides, varying the probe forces reveals actual response characteristics of artificial skin. Here, the probe forces per unit area ($\equiv \frac{F_{\text{probe}}}{S_{\text{probe}}}$) could be used to evaluate the working range of TacLINK, i.e., as shown in Fig. 6.3

- At 0 kPa, probe forces of ~ 0.11 N and ~ 0.2 N were applied to deform the skin to 5 mm, and 10 mm, corresponding to forces applied per unit area $\frac{0.11(\text{N})}{23.8 \times 10^{-2}(\text{cm}^2)} = 0.46 \text{ N/cm}^2$ and $\frac{0.2(\text{N})}{23.8 \times 10^{-2}(\text{cm}^2)} = 0.84 \text{ N/cm}^2$, respectively.

- At 0.5 kPa, probe forces of ~ 0.38 N and ~ 0.64 N were applied to deform the skin to 5 mm, and 10 mm, corresponding to forces applied per unit area $\frac{0.38(\text{N})}{23.8 \times 10^{-2}(\text{cm}^2)} = 1.60 \text{ N/cm}^2$ and $\frac{0.64(\text{N})}{23.8 \times 10^{-2}(\text{cm}^2)} = 2.69 \text{ N/cm}^2$, respectively.

- At 1.0 kPa, probe forces of ~ 0.65 N and ~ 1.0 N were applied to deform the skin to 5 mm, and 10 mm, corresponding to forces applied per unit area $\frac{0.65(\text{N})}{23.8 \times 10^{-2}(\text{cm}^2)} = 2.73 \text{ N/cm}^2$ and $\frac{0.2(\text{N})}{23.8 \times 10^{-2}(\text{cm}^2)} = 4.20 \text{ N/cm}^2$, respectively.

- At 1.5 kPa, probe forces of ~ 0.93 N and ~ 1.4 N were applied to deform the skin to 5 mm, and 10 mm, corresponding to forces applied per unit area $\frac{0.93(\text{N})}{23.8 \times 10^{-2}(\text{cm}^2)} = 3.90 \text{ N/cm}^2$ and $\frac{1.4(\text{N})}{23.8 \times 10^{-2}(\text{cm}^2)} = 5.6 \text{ N/cm}^2$, respectively.

As the inner pressure increased, we can observe that the probe force rapidly increased, thus by controlling the inner pressure we could alter significantly the nominal stiffness of the skin and change the interactive interface of TacLINK in various applications. To sum up, a single-point force contact scenario using a probe attached in a loadcell is very challenging (i.e., create a point load and perceive the entire force applied by a nodal tactile force), because the real probe has a finite area and the skin is also non-ideal (soft, thick), etc. The obtained results indicate that TacLINK is capable of determining and representing the distribution of external contact force.

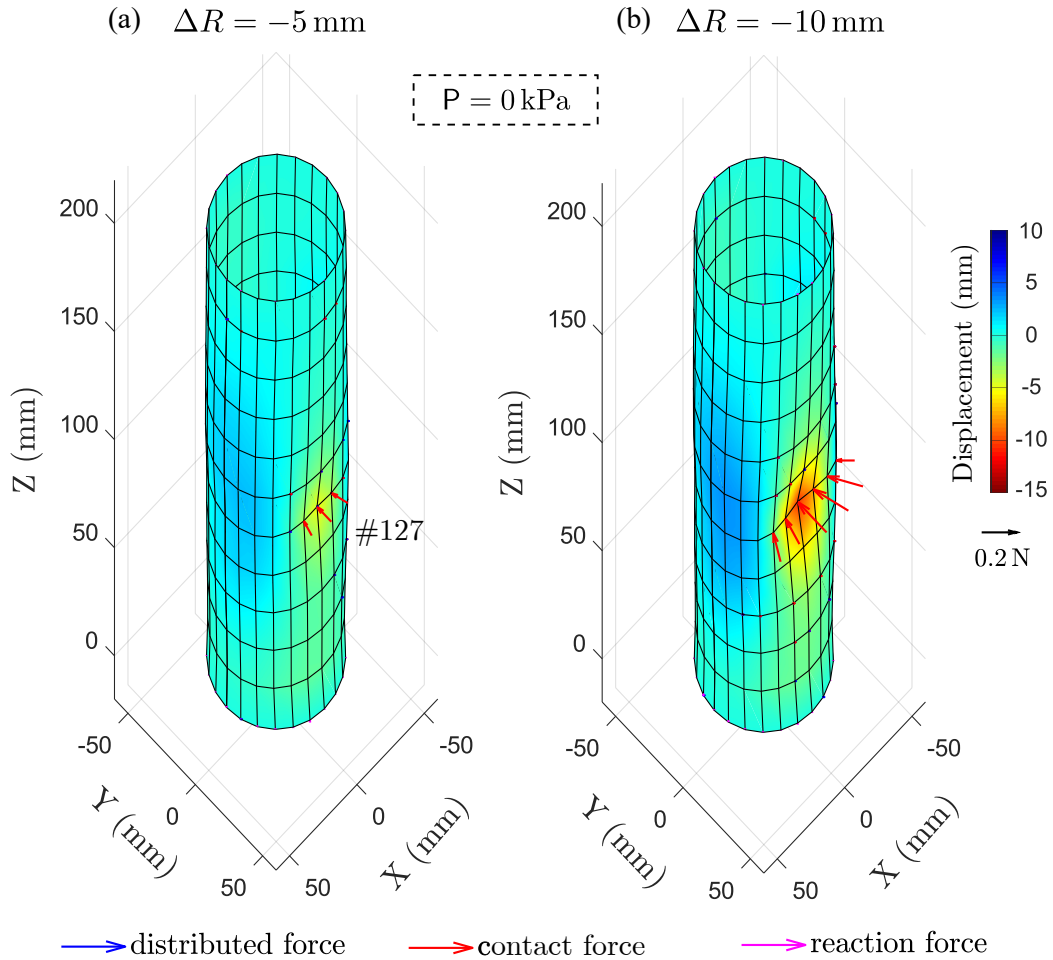


Figure 6.4: Contact force reconstruction of the probe applied yielding radial deflections ΔR at node #127 with inner air pressure $P = 0 \text{ kPa}$.

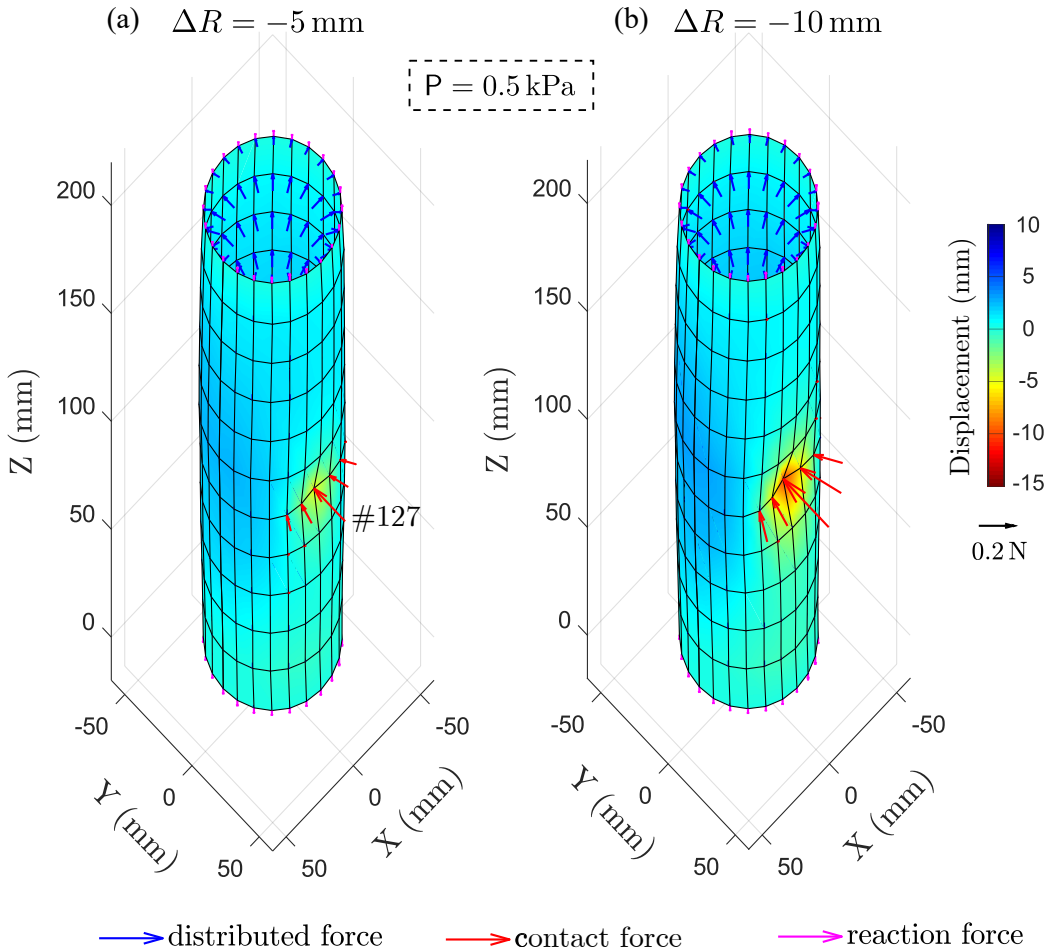


Figure 6.5: Contact force reconstruction of the probe applied yielding radial deflections ΔR at node #127 with inner air pressure $P = 0.5 \text{ kPa}$.

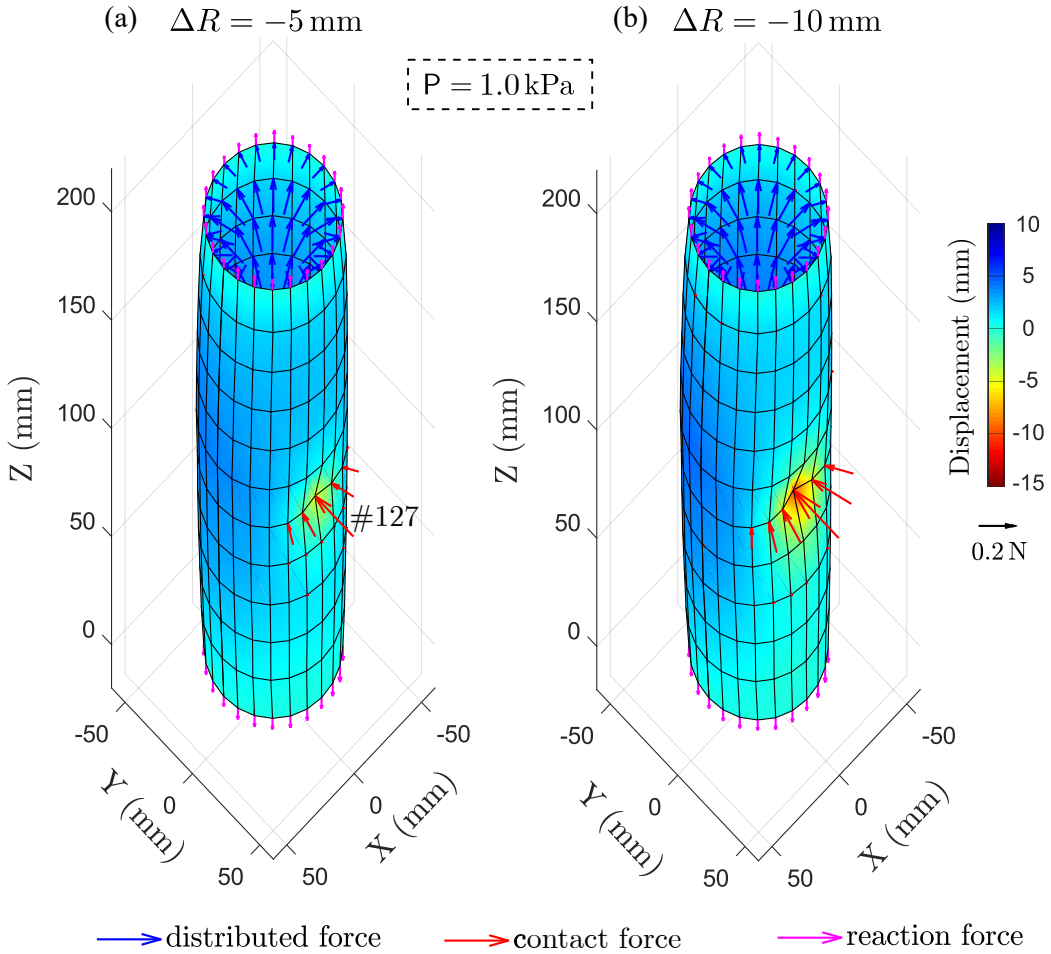


Figure 6.6: Contact force reconstruction of the probe applied yielding radial deflections ΔR at node #127 with inner air pressure $P = 1.0 \text{ kPa}$.

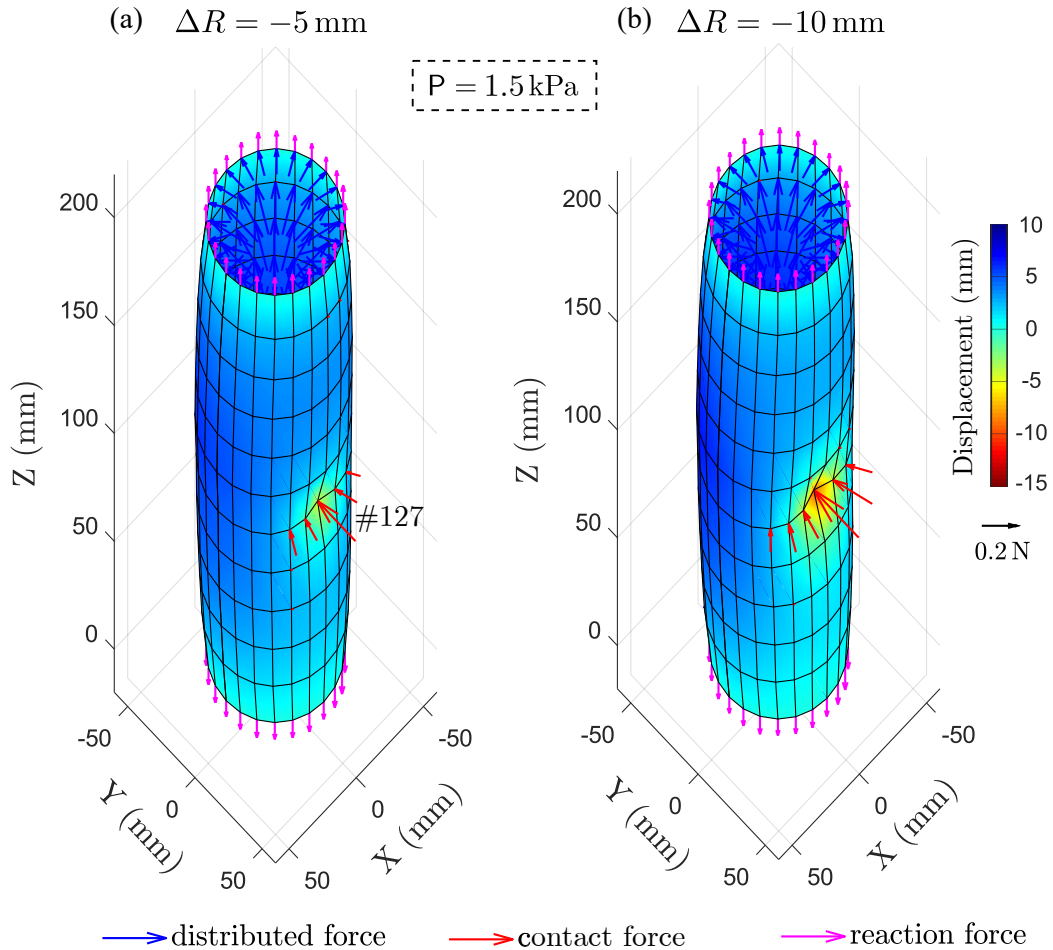


Figure 6.7: Contact force reconstruction of the probe applied yielding radial deflections ΔR at node #127 with inner air pressures $P = 1.5 \text{ kPa}$.

6.3.3 Multiple Large Area Contacts

The design aim of TacLINK is to sense various contacts with real-world objects and humans. Thus, we performed interactive experiments in which TacLINK contacts real objects, and with humans. Figures 6.8 and 6.9 show the sensing performance of TacLINK contacting with flat and cylindrical surfaces, respectively. We can observe that not only the shape of the contacted surface is robustly reconstructed, but also the location and intensity of contact force are provided in detail on the whole skin surface. Tactile forces are distributed only in contact regions but are absent from other regions, even those that showed deformation.

Similarly, although diverse actions could be derived from human fingers and hands, such as touch, press, poke, tickle, rub, pinch, etc. TacLINK could efficiently sense these various contact scenarios. For example, press and tinkle with a finger and multiple fingers are shown in Fig. 6.10 and 6.11, respectively. Figures 6.12 and 6.13 illustrate the skin are under pinching and squeezing, respectively. These results indicate that TacLINK can robustly reconstruct both 3-D deformation and external acting forces in large and multi-contact regions. Generally, under conditions of physical interaction, TacLINK documents detailed 3-D deformation of the skin surface caused by external forces, of which location and intensity are represented by the distribution of tactile force. It is noteworthy that previous vision-based tactile force sensing techniques with markers, such as machine learning [42], and experimental calibration [43], [45], could estimate the total force applied, but not able to determine the distribution of applied forces in scenarios such as under large area and multiple point contacts. Besides, tactile skin designs with discrete electronic sensing elements [10], [38] can not detect a touch in regions not occupied by such sensing elements. However, using the proposed FEM approach to reconstruct contact forces over a large and continuous area, the proposed vision sensing system can simultaneously perceive contact forces throughout the skin surface efficiently.

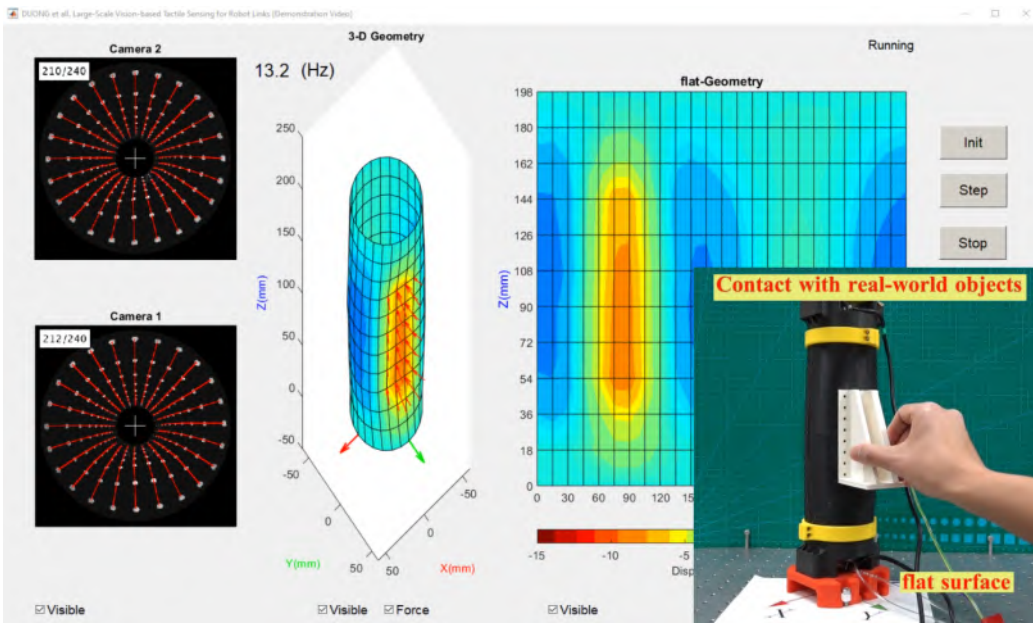


Figure 6.8: Touching TacLINK with a flat surface.

The open source and a demonstration video of TacLINK can be found at <https://github.com/lacduong/TacLINK>.

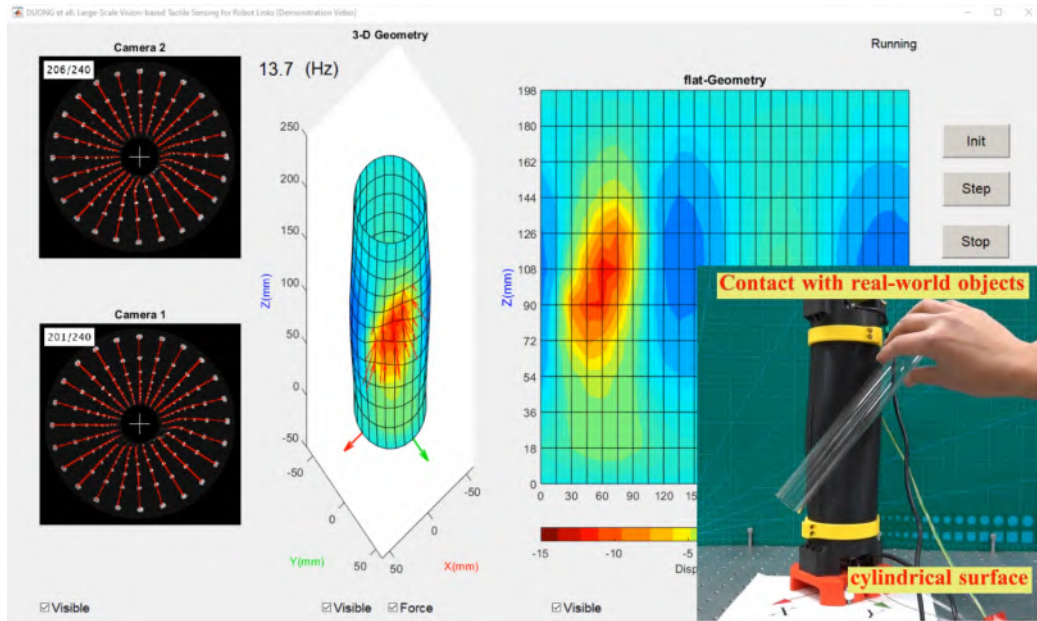


Figure 6.9: Touching TacLINK with a curved cylinder surface.

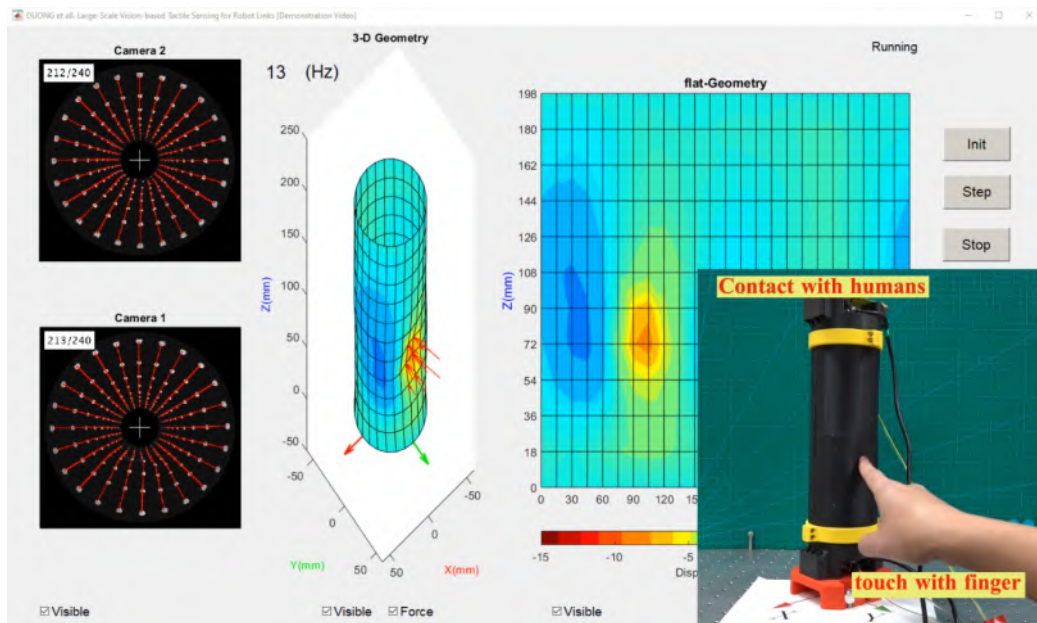


Figure 6.10: Touching TacLINK with a finger.

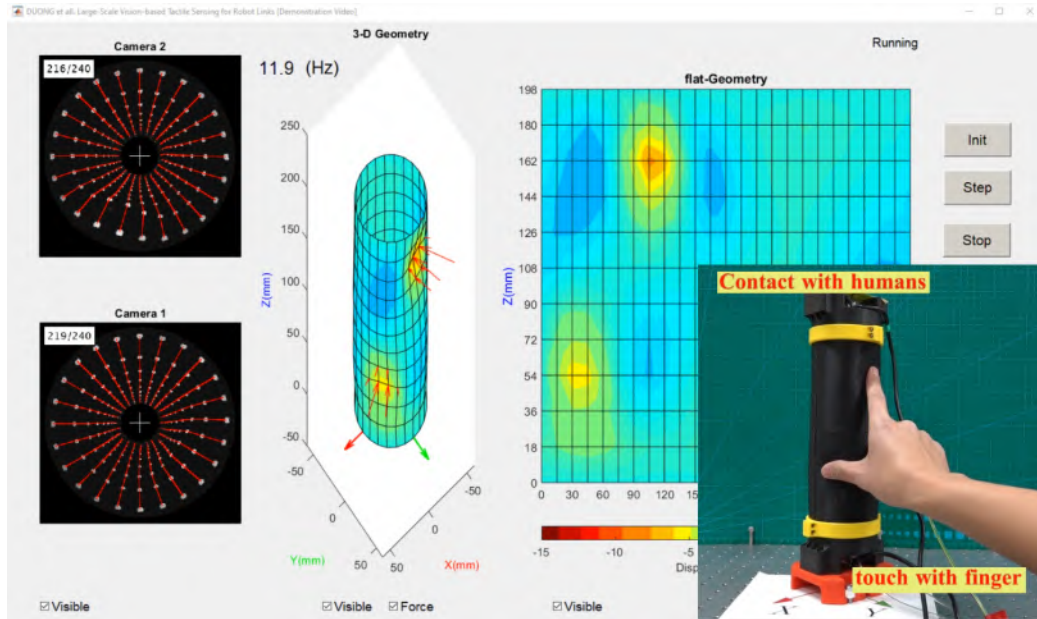


Figure 6.11: Touching TacLINK with multiple fingers.

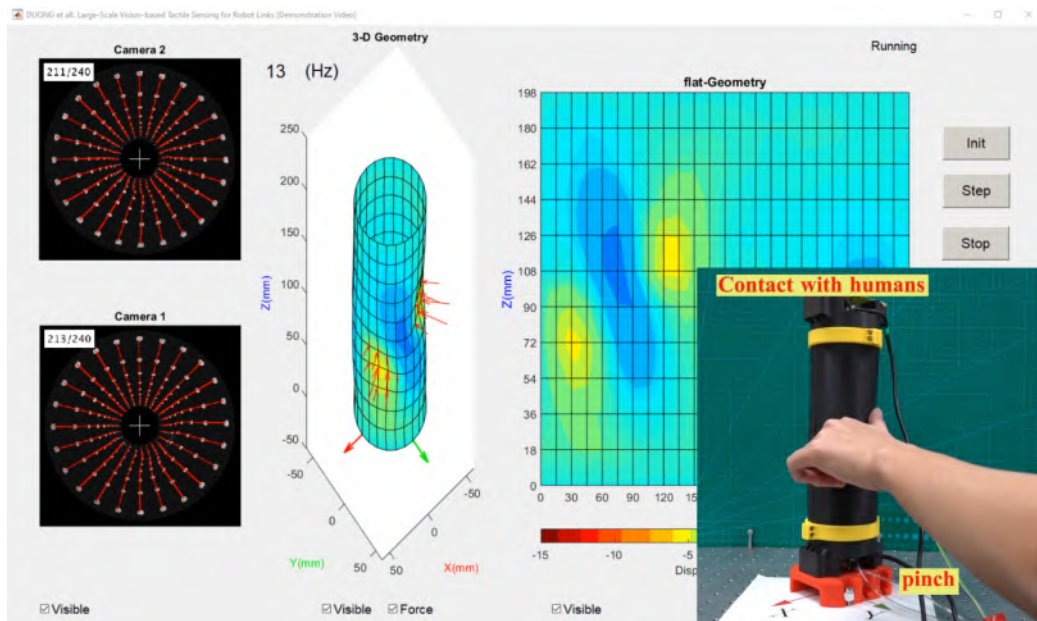


Figure 6.12: Pinching TacLINK by fingers.

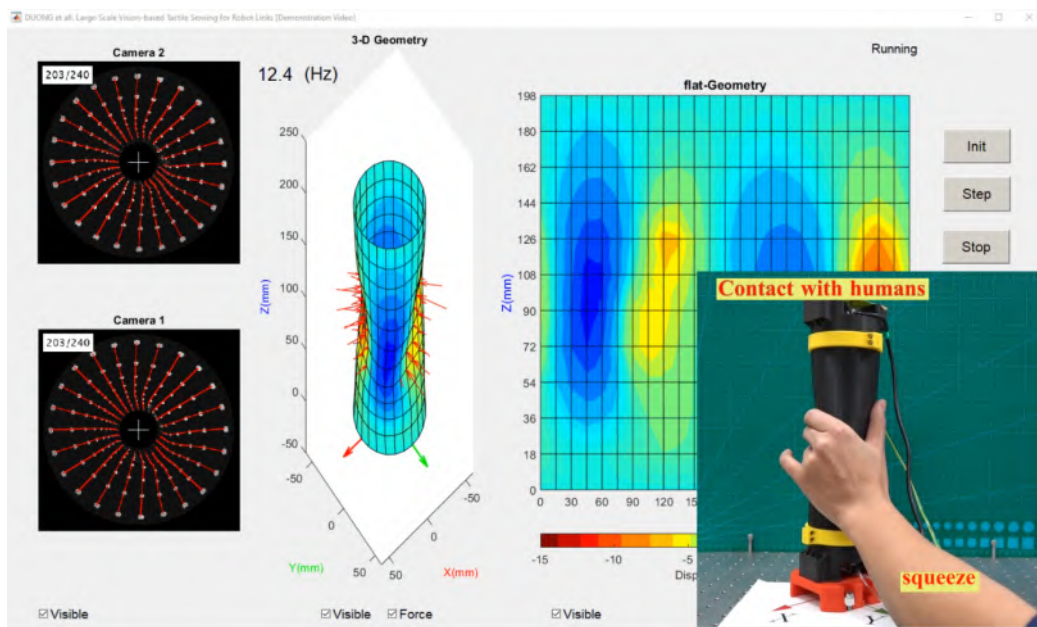


Figure 6.13: Squeezing TacLINK by fingers.

6.4 Summary

In this chapter, we assumed, analyzed, and quantitatively evaluated the FEM approach to calculate the tactile force, which represents the external force exerting on the artificial skin body. The proposed method of force computation using a global stiffness matrix with measured nodal displacements supplied by the vision system, so the computed force result at each node includes spatial errors that are occurred around its neighbors. Note that a shell element carries forces in all directions, undergoes bending, and in-plane deformation i.e., including bending and in-plane stiffness. With the cylindrical shape of the skin surface and spatial error of the stereo camera, we investigated that tactile force computation Eq. (6.1) can cause errors seriously in the tangential, and axial directions with much higher stiffness. Therefore, only the radial force component of TacLINK is considered. Tactile forces are conveyed by the distribution of tactile forces, with various contact scenarios were tested. The experimental results indicate that TacLINK is able to perceive and reconstruct robustly both contact geometry and contact force throughout on the skin surface contacting various real-world objects and humans. Because tactile forces are constructed on a large area and large numbers of measured points/nodes, its intensity could not be expected to convey accurately, but information of tactile force distribution was well reconstructed, which is very important for a large-scale tactile sensing system.

Chapter 7

Conclusion

Touch sensing is a crucial means for humans to perceive and interact with the environment. Meanwhile, the implementation of touch sensation on robots, especially a large-scale, remains challenging. Although in recent decades, tactile sensor technology has shown great advances in design, the main challenge relates to mimicking the inherent complexity of natural skin structure that has a particularly high density of various types of sensory receptors. The previous approach focused mostly on developing a skin-like structure with a matrix of sensing elements without considering the complexity of wiring, bulk of electronics, and risk of damage, etc. for the deployment of large-scale tactile sensing in practice. The thesis presents the developed TacLINK for robotic links with large-scale soft tactile skin. The feasibility of design and robustness in tactile reconstruction were verified. The system is low cost, affording a simple scalable structure, and real-time performance. Notably, TacLINK is not only equipped with sensing ability but can actively react to change its form and stiffness during interaction with the surrounding environment. Deployment of TacLINK with highly deformable skin and tactile force feedback will enable robots to interact safely and intelligently.

7.1 Summary and Contribution

The originality of the research is the development of a novel vision-based tactile force sensing principle. The research succeeded in developing a system with a curved cylinder skin shape that is a great challenge in the current literature on the tactile sensor. The scientific and technical contributions of the research can be summarized as

1) A novel design of a large-scale tactile sensing system at low-cost for robot links: The research proposed TacLINK, which is an efficient tactile sensing system for robot links with a large sensing area $\sim 500 \text{ cm}^2$. As described in Chapter 3, the artificial skin is fabricated by casting method using soft silicone rubber (Ecoflex-0050). The skin is continuous, highly durable, comfortable to touch, and even inflatable to change its form and stiffness. TacLINK is scalable and low in cost (about 150 \$US) but high performance in both contact geometry and contact force sensing upon interactions between the robot and surroundings.

2) A robust vision-based tactile sensing system: As presented in Chapter 4, the stereo vision, which comprises two facing cameras, tracks efficiently all the markers locating on the inner wall of the elongated skin surface thanks to the camera model and proposed algorithms (stereo registration, 3-D reconstruction). The entire 3-D deformation of the skin is derived without the need to embed any sensing elements or electronic components inside the skin, therefore minimizing the challenges in wiring, the bulk of electronics for developing large-scale tactile sensing that is great challenges in the current literature in the tactile technology. The vision-based system could output accurately the 3-D position of the markers/nodes with absolute error less than 0.7 mm ($\sim 5\% \text{ FS}$). Moreover, the automatic technique for self-calibration of the camera parameters was also developed and described, thus, the parameters of the vision system can be easily obtained.

3) The finite element method for tactile force sensing: Previous research on vision-based tactile sensing faced difficulty in finding the relationship be-

tween force and deformation. As presented in Chapter 5, we utilized the finite element method for shell structure to derive the structural stiffness of the skin, the contact force, therefore, could be calculated straightforwardly based on the 3-D deformation provided from the vision system. Thanks to the finite element approach, we could also characterize the artificial skin to verify and evaluate the design to choose suitable materials and sizes for the specific application..

As presented in Chapter 6, we investigated that tactile force computation can cause errors seriously in the tangential, and axial directions that are much higher stiffness. Thus, to ensure reliability, only the radial tactile force component of TacLINK is considered. Various contact scenarios with real-world objects and humans were tested, the results indicate that TacLINK reconstructs robustly both contact geometry and contact force throughout the skin surface, conveying meaningful tactile sensing information.

4) A highly scalable structure and generalized sensing principle for the development of the vision-based tactile sensing devices: The proposed skin with markers is simple and easily fabricated by the casting method. The shape and size could be customized for the specified applications. Vision technology is also highly scalable, i.e., a set of cameras can be installed to track the displacements of the artificial skin. The finite element method (FEM) is generalized that the structural stiffness of the skin could be derived by using the analytical FEM. The research expects to contribute significantly to the tactile sensing field with a generalized method for designing vision-based tactile force sensing devices.

7.2 Discussion

7.2.1 Vision-Based Tactile Force Sensing

In this system, utilizing only two facing cameras on a simple structure, the proposed system using the finite element method can efficiently track the 3-D

displacement of the markers/nodes (nodes of the FE model) to reconstruct the distribution of force acting on the continuous skin surface that is a great challenge in the current literature on the tactile sensor. However, during tracking the skin deformation, challenges of the vision system relate to the presence of reflected bright regions on the black skin surface (background), this effect significantly impedes image processing to track the white markers. Thus, improvement of the skin fabrication method is needed to reduce the reflexed light on the inner wall of the skin surface, such as change the roughness of the skin to trap the reflexed light.

The proposed vision-based tactile force sensing could be utilized to develop various tactile sensing devices. However, the proposed FEM to compute the stiffness of the skin is only suitable for a thin-shell structure. To apply more general shapes, such as cone, sphere, or complex surface, the more complex formulations of FEM (e.g., 3-D solid elements) are needed to model these structures. Note that the markers are the feature nodes of the FE mesh of the skin, resulting in a trade-off between the accuracy of the FE model and the detection of the vision system, i.e., increasing the accuracy of the FEM (with complex element model, dense markers/nodes) yields to reduce the detectability of the camera, and vice versa. Besides, designing the vision system is the issue, in which, utilizing the RGB-D cameras is also a convenient method to detect deformation. Thus, further researches in design are needed to deploy the proposed sensing principle for more devices.

7.2.2 FE Model and Material Nonlinearity

The finite element method is originally formulated based on the principle of virtual work in elasticity as in Eq. (5.25), therefore, the tactile force computation depends largely on the element model (strains $\hat{\epsilon}$ and stresses $\hat{\sigma}$ models) and divided mesh size ($2a, 2b$). These parameters are very important for representing the strain energy of actual skin deformation. In this system, the prototype model could not be ideal like the theoretical model, the size

of FE mesh ($2a = 9.5$ mm, $2b = 18$ mm) was not dense enough, etc., thus, the intensity of tactile force reconstruction might not be well reconstructed, especially over large contact areas with inner air pressure applied.

Besides, the linear finite element model requires linear elastic material and small displacements (based on infinitesimal strain theory), while a non-linear analysis, on the other hand, can describe elastoplastic materials and large displacements. In this research, to ensure the real-time performance of a sensing system, the artificial skin was assumed to be linearly elastic, i.e., the stiffness matrix is constant. However, the stiffness matrix remains constant on a linear region, but this phenomenon may not accurately describe the non-linear region. Thus, future researches on the nonlinearities of the skin material, including hyperelastic materials (e.g., silicone, rubber, etc.), are needed to analyze and describe accurately the response of the skin.

7.3 Future Work and Outlook

In humans, sensory skin not only helps us avoid any damage to the body from potentially harmful interaction but also a means of communication with the surroundings. Thus, we desire to create a generation of robots with similar sensing capabilities.

The technical contribution of the research is the generalized technique to design a vision-based tactile force sensing system. Future works will continue to use this technique for other parts of a robot, such as the head, hands, fingers, chest, legs, etc., and various sensory devices in the industry, medical, and healthcare. The deployment of the tactile devices on the control tasks, such as safe reaction, interactive action, is also an essential research direction for future work. Further investigations and researches to overcome the aforementioned limitations and issues are also very needed.

Although the presented work is rather complete, a scalable vision-based tactile sensing system, it is only a starting point, the outlook for future

research and development is

1) New generations of the robot with whole-body tactile sensing: The intelligent robot, such as humanoid robot, service robot, therapist robot, frequently interacts with the human at close distance, as well as these robots are expected to have ability to manipulate objects dexterously. Thus, equipping and deploying the robot with the sense of touch enables safe and intelligent interaction and better manipulation.

2) Human-like prosthetics with tactile sensation: The generation of prosthetics with artificial sensing and nerve is very promising in practice. Smart prosthetics can help the handicapped person perceiving pain, sense real-world objects, etc. as the sensory function of a normal person. This approach is very practical and expected to realize in near future.

List of Publications

Journal Papers:

- 1 . **L. Van Duong**, V. A. Ho, “Large-Scale Vision-Based Tactile Sensing for Robot Links: Design, Modeling, and Evaluation,” in *IEEE Transactions on Robotics (T-RO)*¹, vol. 37, no. 2, pp. 390-403, April 2021, doi: 10.1109/TRO.2020.3031251

International Conference Papers:

1. **L. Van Duong**, R. Asahina, J. Wang and V. A. Ho, “Development of a Vision-Based Soft Tactile Muscularis,” 2019 2nd IEEE International Conference on Soft Robotics (RoboSoft), Seoul, Korea (South), 2019, pp. 343-348, doi: 10.1109/ROBOSOFT.2019.8722814.

¹Citation statistics from Clarivate analytics, released June 2020:
• Eigenfactor: 0.01428 (#1 in robotics),
• Total citations: 14,259 (#1 in robotics),
• Impact factor: 6.123 (#2 in robotics).

Reference

- [1] R. S. Dahiya and M. Valle, “Robotic tactile sensing: Technologies and system,” *Springer*, 2014.
- [2] Park, Minhoon *et al.*, “Recent Advances in Tactile Sensing Technology.” *Micromachines*, vol. 9(7):321, 2018, doi:10.3390/mi9070321.
- [3] P. S. Girão, P. M. P. Ramos *et al.*, “Tactile sensors for robotic applications,” *Meas. J. Int. Meas. Confed.*, vol. 46, no. 3, pp. 1257–1271, 2013.
- [4] R. S. Dahiya, G. Metta *et al.*, “Tactile sensing-from humans to humanoids,” *IEEE Trans. Robot.*, vol. 26, no. 1, pp. 1-20, 2010.
- [5] Z. Kappassov, J. A. Corrales *et al.*, “Tactile sensing in dexterous robot hands - Review,” *Rob. Auton. Syst.*, vol. 74, pp. 195–220, 2015.
- [6] Kim J., Lee M., Shim H. *et al.*, “Stretchable silicon nanoribbon electronics for skin prosthesis,” *Nature Communications*, 2014, Art. no. 5747.
- [7] Sun Q, Seung W, Kim BJ *et al.*, “Active Matrix Electronic Skin Strain Sensor Based on Piezopotential-Powered Graphene Transistors,” *Adv Mater.*, 2015, Art. no 27(22):3411-7.
- [8] Wang S., Xu J., Wang W. *et al.*, “Skin electronics from scalable fabrication of an intrinsically stretchable transistor array,” *Nature*, 2018, Art. no. 555, 83–88.

- [9] Y. Al-Handarish et al., “A Survey of Tactile-Sensing Systems and Their Applications in Biomedical Engineering,” *Adv. Mater. Sci. Eng.*, vol. 2020, 2020, doi: 10.1155/2020/4047937.
- [10] A. Schmitz, P. Maiolino, M. Maggiali, L. Natale, *et al.*, “Methods and technologies for the implementation of large-scale robot tactile sensors,” *IEEE Trans. Robot.*, vol. 27, no. 3, pp. 389-400, 2011.
- [11] Y. S. Lee and K. D. Wise, “A batch-fabricated silicon capacitive pressure transducer with low temperature sensitivity,” *IEEE Transactions on Electron Devices*, vol. 29, no. 1, pp. 42-48, 1982.
- [12] L. Harmon, “Automated tactile sensing,” *The International Journal of Robotics Research*, vol. 1, no. 2, pp. 3-32, 1982.
- [13] Hollander L.E., Vick G.L., Diesel T, “The piezoresistive effect and its applications,” *Rev. Sci. Instrum.*, vol. 31, pp. 323–327, 1960.
- [14] Zou L., Ge C., Wang Z.J. Cretu, E. Li, X. “Novel Tactile Sensor Technology and Smart Tactile Sensing Systems: A Review,” *Sensors*, vol. 17, no. 2653, 2017.
- [15] T. V. Papakostas, J. Lima and M. Lowe, “A large area force sensor for smart skin applications,” *Sensors, 2002 IEEE*, Orlando, FL, USA, 2002, vol. 2, pp. 1620-1624.
- [16] D. Goger, N. Gorges and H. Worn, “Tactile sensing for an anthropomorphic robotic hand: Hardware and signal processing,” in *Proc. 2009 IEEE Int. Conf. Intell. Robots Autom.*, Kobe, 2009, pp. 895-901.
- [17] M. W. Strohmayer, H. Wörn and G. Hirzinger, “The DLR artificial skin step I: Uniting sensitivity and collision tolerance,” in *Proc. 2013 IEEE Int. Conf. Intell. Robots Autom.*, Karlsruhe, 2013, pp. 1012-1018.

- [18] Uriel Martinez-Hernandez, “Tactile Sensors,” *Scholarpedia*, 10(4):32398, 2015.
- [19] Siciliano, B and Khatib, “Springer Handbook of Robotics,” *Springer*, 2008.
- [20] D. Damjanovic, “Ferroelectric, dielectric and piezoelectric properties of ferroelectric thin films and ceramics,” *Reports on Progress in Physics*, vol. 61, no. 9, pp. 1267–1324, 1998.
- [21] G. M. Krishna and K. Rajanna, “Tactile sensor based on piezoelectric resonance,” *IEEE Sensors Journal*, vol. 4, no. 5, pp. 691-697, Oct. 2004.
- [22] Windecker R., Tiziani H.J., “Optical roughness measurements using extended white-light interferometry,” *Opt. Eng.*, vol. 38, pp. 1081–1087, 1999.
- [23] Ohka M., Mitsuya Y., Higashioka I., Kabeshita, H. “An experimental optical three-axis tactile sensor for micro-robots,” *Robotica*, vol. 23, pp. 457–465, 2005.
- [24] G. Palli, L. Moriello, U. Scarcia, *et al.*, “Development of an optoelectronic 6-axis force/torque sensor for robotic applications,” *Sens. Actuators A: Phys.*, vol. 220, pp. 333-346, 2014.
- [25] Z. Kappassov, D. Baimukashev, Z. Kuanyshuly, Y. Massalin, A. Urazbayev and H. A. Varol, “Color-Coded Fiber-Optic Tactile Sensor for an Elastomeric Robot Skin,” *2019 International Conference on Robotics and Automation*, Montreal, QC, Canada, 2019, pp. 2146-2152.
- [26] M. Soni, R. Dahiya, “Soft eSkin: distributed touch sensing with harmonized energy and computing,” *Phil. Trans. R. Soc. A*, vol. 378, no. 2164, p. 20190156, 2019.

- [27] B. Shih, D. Shah *et al.*, “Electronic skins and machine learning for intelligent soft robots,” *Sci. Robot.*, vol. 5, no. 41, 2020, Art. no. eaaz9239.
- [28] Zang Y., Zhang F., Di C.A., Zhu D., “Advances of flexible pressure sensors toward artificial intelligence and health care applications,” *Mater. Horizons*, vol. 2, no. 2, pp. 140-156, 2015.
- [29] D. Kwon, T. Lee *et al.*, “Highly sensitive, flexible, and wearable pressure sensor based on a giant piezocapacitive effect of three-dimensional microporous elastomeric dielectric layer,” *ACS Appl. Mater. Interfaces*, vol. 8, no. 26, pp. 16922-16931, 2016.
- [30] Y. Kim, A. Chortos *et al.*, “A bioinspired flexible organic artificial afferent nerve,” *Science*, vol. 360, no. 6392, pp. 998-1003, 2018.
- [31] W. W. Lee, Y. J. Tan *et al.*, “A neuro-inspired artificial peripheral nervous system for scalable electronic skins,” *Sci Robot.*, vol. 4, no. 32, 2019, Art. no. eaax2198.
- [32] Sundaram, S., Kellnhofer *et al.*, “Learning the signatures of the human grasp using a scalable tactile glove,” *Nature*, vol. 569, pp. 698-702, 2019.
- [33] M. Amjadi, A. Pichitpongkit, S. Lee, S. Ryu, and I. Park, “Highly stretchable and sensitive strain sensor based on silver nanowireelastomer nanocomposite,” *ACS Nano*, vol. 8, no. 5, pp. 5154-5163, 2014.
- [34] Ravinder S. Dahiya, Giorgio Metta *et al.*, “Tactile sensing-from humans to humanoids,” *IEEE Trans. Robot.*, vol. 26, no. 1, pp. 1-20, 2010.
- [35] S. Youssefi, S. Denei, F. Mastrogiovanni and G. Cannata, “A real-time data acquisition and processing framework for large-scale robot skin,” *Robot Auton. Syst.*, vol. 68, pp. 86-103, Jun. 2015.

- [36] T. Mukai, M. Onishi, T. Odashima, S. Hirano and Z. Luo, “Development of the Tactile Sensor System of a Human-Interactive Robot RI-MAN,” *IEEE Transactions on Robotics*, vol. 24, no. 2, pp. 505-512, 2008.
- [37] P. Maiolino, M. Maggiali, G. Cannata, G. Metta, and L. Natale, “A flexible and robust large scale capacitive tactile system for robots,” *IEEE Sens. J.*, vol. 13, no. 10, pp. 3910–3917, 2013.
- [38] G. Cheng, E. Dean-Leon, F. Bergner *et al.*, “A comprehensive realization of robot skin: Sensors, sensing, control, and applications,” *Proc. IEEE*, vol. 107, no. 10, pp. 2034-2051, 2019.
- [39] Shimonomura K., “Tactile Image Sensors Employing Camera: A Review,” *Sensors*, vol. 19, no. 18, 2019, Art. no. 3933.
- [40] A. C. Abad and A. Ranasinghe, “Visuotactile Sensors With Emphasis on GelSight Sensor: A Review,” *IEEE Sensors Journal*, vol. 20, no. 14, pp. 7628-7638, 15, 2020.
- [41] K. Kamiyama, K. Vlack, T. Mizota, H. Kajimoto *et all.*, “Vision-based sensor for real-time measuring of surface traction fields,” *IEEE Computer Graphics and Applications*, vol. 25, no. 1, pp. 68-75, 2005.
- [42] W. Yuan, S. Dong, and E. H. Adelson, “GelSight: High-resolution robot tactile sensors for estimating geometry and force,” *Sensors*, vol. 17, no. 12, pp. 2762, 2017.
- [43] Sato K., Kamiyama K., Kawakami N., Tachi S. “Finger-shaped GelForce: Sensor for measuring surface traction fields for robotic hand,” *IEEE Trans. Haptics*, vol. 3, pp. 37-47, 2010.
- [44] B. Ward-Cherrier et al., “The TacTip family: soft optical tactile sensors with 3D-printed biomimetic morphologies,” *Soft Robotics*, vol. 5, no. 2, 2018.

- [45] Y. Ito, Y. Kim, G. Obinata, "Multi-axis force measurement based on vision-based fluid-type hemispherical tactile sensor," in *Proc. IEEE/RSJ Int. Conf. Intell. Robots Syst.*, 2013, pp. 4729-4734.
- [46] M. Greminger, B. Nelson, "Vision-based force measurement," *IEEE Trans. Pattern Anal. Mach. Intell.*, vol. 15, no. 4, pp. 290-298, 2004.
- [47] A. N. Reddy *et al.*, "Miniature compliant grippers with vision-based force-sensing," *IEEE Trans. Robot.*, vol. 26, no. 5, pp. 867-877, 2010.
- [48] A. I. Aviles, S. M. Alsaleh, J. K. Hahn, A. Casals, "Towards retrieving force feedback in robotic-assisted surgery: A supervised neuro-recurrent-vision approach," *IEEE Trans. Haptics*, vol. 10, no. 3, pp. 431-443, 2017.
- [49] Z. Dequidt, J. Dequidt, C. Duriez, "Vision-based sensing of external forces acting on soft robots using finite element method," *IEEE Robot. Autom. Lett.*, vol. 3, no. 3, pp. 1529-1536, 2018.
- [50] Lim H. O., Tanie K., "Human Safety Mechanisms of Human-Friendly Robots: Passive Viscoelastic Trunk and Passively Movable Base," *The International Journal of Robotics Research*, vol. 19, no. 4, pp. 307-335.
- [51] G. A. Pratt and M. M. Williamson, "Series elastic actuators," in *Proc. IEEE Int. Conf. Intell. Robots Syst.*, Pittsburgh, PA, USA, 1995, pp. 399-406.
- [52] K. Kong, J. Bae and M. Tomizuka, "Control of Rotary Series Elastic Actuator for Ideal Force-Mode Actuation in Human–Robot Interaction Applications," *IEEE/ASME Transactions on Mechatronics*, vol. 14, no. 1, pp. 105-118, Feb. 2009.
- [53] N. M. Belyaev, "Strength of materials," *MIR Publishers*, Moscow, pp. 404-406, 1979.

- [54] R. Hartley and A. Zisserman, “Multiple View Geometry in Computer Vision,” *Cambridge, U.K.:Cambridge Univ. Press*, 2003.
- [55] S. Das, N. Ahuja, “Performance analysis of stereo vergence and focus as depth cues for active vision,” *IEEE Trans. Pattern Anal. Mach. Intell.*, vol. 17, no. 12, pp. 1213-1219, Dec. 1995.
- [56] Tatsuya Sakuma *et al.*, “A universal gripper using optical sensing to acquire tactile information and membrane deformation,” in *Proc. IEEE Int. Conf. Intell. Robots Syst.*, 2018, pp. 6431-6436.
- [57] A. Myronenko, X. Song, “Point set registration: coherent point drift,” *IEEE Trans. Pattern Anal. Mach. Intell.*, vol. 32, no. 12, pp. 2262-2275, 2010.
- [58] A. Vandini, C. Bergeles, B. Glocker, P. Giataganas, G.-Z. Yang, “Unified tracking and shape estimation for concentric tube robots,” *IEEE Trans. Robot.*, vol. 33, no. 4, pp. 901-915, 2017.
- [59] Z. Zhang, “A flexible new technique for camera calibration,” *IEEE Trans. Pattern Anal. Mach. Intell.*, vol. 22, no. 11, pp. 1330-1334, 2000.
- [60] R. Y. Tsai, “A versatile camera calibration technique for high-accuracy 3-D machine vision based metrology using off-the-shelf TV cameras and lenses,” *IEEE J. Robot. Automat.*, vol. 3, no. 4, pp. 323-344, 1987.
- [61] A. W. Fitzgibbon, “Simultaneous linear estimation of multiple view geometry and lens distortion,” *Comput. Vis. Pattern Recognit.*, vol. 1, pp. 125-132, 2001.
- [62] Abaqus, Inc. (2017), “Abaqus/CAE User’s Manual,” [Online]. Available: <https://abaqus-docs.mit.edu/2017/English/SIMACAEELMRefMap/simaelm-c-general.htm>

- [63] Abaqus, Inc. (2001), “Fundamental FEA Concepts and Applications,” [Online]. Available: https://www.cae.tntech.edu/~chriswilson/FEA/ANSYS/ANSYSGuide_fea-concepts.pdf
- [64] Abaqus, Inc. (2017), “Abaqus/CAE User’s Manual,” [Online]. Available: <http://130.149.89.49:2080/v6.11/books/usi/default.htm?startat=pt04ch25s01.html>
- [65] E. Oñate, “Structural analysis with the finite element method linear statics, in: Beams, Plates and Shells of Lecture Notes on Numerical Methods in Engineering and Sciences,” vol. 2, *Springer*, Berlin, 2013.
- [66] E. Oñate, “Structural analysis with the finite element method linear statics, in: Basis and Solids of Lecture Notes on Numerical Methods in Engineering and Sciences,” vol. 1, *Springer*, Berlin, 2009.
- [67] Liu GR, Quek SS, “The finite element method: a practical course. Butterworth Heinemann,” *Oxford*, 2003.
- [68] Young W. Kwon , Hyochoong Bang, “The Finite Element Method Using MATLAB,” *CRC Press, Inc.*, Boca Raton, FL, 2000.
- [69] Ahmad S., Irons B. M., Zienkiewicz O. C., “Analysis of thick and thin shell structures by curved finite elements,” *IJNME*, vol 2, pp. 419–451, 1970.
- [70] Dragan Marinković, Heinz Köppe, Ulrich Gabbert, “Numerically Efficient Finite Element Formulation for Modeling Active Composite Laminates,” *Mechanics of Advanced Materials and Structures*, vol. 13, no. 5, pp. 379-392, 2006.